UNIVERSITY OF OKLAHOMA

GRADUATE COLLEGE

SHAPE DESIGN SENSITIVITY ANALYSIS AND OPTIMIZATION FOR 2-D STRUCTURAL COMPONENTS UNDER MIXED-MODE FRACTURE USING EXTENDED FINITE ELEMENT METHOD AND LEVEL SET METHOD

A DISSERTATION

SUBMITTED TO THE GRADUATE FACULTY

in partial fulfillment of the requirements for the

Degree of

DOCTOR OF PHILOSOPHY

By

MANGESH SHRIKANT EDKE
Norman, Oklahoma
2009

SHAPE DESIGN SENSITIVITY ANALYSIS AND OPTIMIZATION FOR 2-D STRUCTURAL COMPONENTS UNDER MIXED-MODE FRACTURE USING EXTENDED FINITE ELEMENT METHOD AND LEVEL SET METHOD

A DISSERTATION APPROVED FOR THE
SCHOOL OF AEROSPACE AND MECHANICAL ENGINEERING

BY

Dr. Kuang-Hua Chang, Chair

Dr. Kurt Gramoll

Dr. Shivakumar Raman

Dr. Zahed Siddique

Dr. Alfred Striz

Dedicated to my loving parents, Sharmila and Shrikant Edke

ACKNOWLEDGMENTS

This research has come to fruition with the help of many individuals that I directly or indirectly interacted with during the last four years at the University of Oklahoma and they all deserve a special mention here.

It is indeed difficult to describe my deep appreciation for my advisor, Professor Kuang-Hua Chang, in a few lines. I cannot thank him enough for his valuable guidance and excellent suggestions, for his support and encouragement through the most difficult times, for believing in me, and for always being available. His enthusiasm for research was contagious and kept me motivated even when unexpected problems surfaced. In every problem that I took to him, he showed me an opportunity to gain further knowledge, enhance quality of this research, and make contribution to the scholarly community. He taught me how to keep the goal in sight and never let me stray from it.

I would like to thank my committee members, Professor Kurt Gramoll, Professor Shivakumar Raman, Professor Zahed Siddique, and Professor Alfred Striz for their valuable comments and suggestions that helped enhance quality of this work. They all have been very approachable and easily available. The courses that I took with Professor Striz have been the backbone for my master's and doctoral research.

I owe special thanks to Professor Stephane Bordas at Glasgow University, UK for making available the XFEM code developed by his research group. His doctoral thesis was immensely helpful in understanding of XFEM-LSM and availability of the code

greatly expedited further developments tasks. He also granted me access to the Computational Mechanics discussion group which was a great resource by itself and I found answers to many questions there.

Although I did not get an opportunity to interact with Professor Baldwin until my research was in final stages, his fracture mechanics course helped me in understanding finer aspects of fracture mechanics. He possesses a wealth of knowledge in fracture and fatigue and patiently answered all my questions. He graciously made available plenty of learning resources and I am grateful for the same. I have enjoyed working as his teaching assistant for the past two years. I am thankful to Professor Harold Stalford for offering me an opportunity to work with Advanced Capstone Project teams. He is energetic, inquisitive, and ever-helpful and it was a pleasure to work with him.

I have been blessed to have great mentors during both internships. Stefano Bernero at Alstom Power, Switzerland was very approachable and friendly and gave me a chance to work on some interesting projects. Dr. Tim Griffin at OMRF is very passionate about his work, is ever ready to help, and is a wonderful person to work with. The summer I spent at OMRF was very exciting and productive and I had a great time working with Tim. Both internships have opened new avenues for me and I wish I could have worked on many more interesting projects.

My colleagues, Sung-Hwan Joo, David Gibson, Trey Wheeler, Tyler Bunting, and most recently, ChienChih Chen have been very supportive. ChienChih's close scrutiny of my dissertation report has helped correct many typographical errors. Since he is going to continue with this research, I am sure he will take this work to new heights.

My stay in Norman was made thoroughly enjoyable and memorable by all my friends. I would like to thank Shailesh Mirasdar, Gautam Sanghavi, Parag Gujar, Mayur Gala, and Manik Naik for their help. I spent several memorable weekends in Duncan with Gauri and Parag Gujar and in Tulsa with Indrani and Arindam Basu. Our exclusive cooking group, Aashish Wadke, Shweta Deshpande, Suyog Lokhande, and I had a great time in Spring ’07. Ameya and Girija Marathe have been special friends through this time and the weekends spent with them and our IFN group were the best ones. My close friends, Aashish Wadke, Lalit Deshpande, Anup Hunnur, Shweta Deshpande, Ha Tran, Srikanth Sathyanarayana, Vishal Kulkarni, Rohan Dubal, Shekhar and Sayali Kamat, Gopinath Venkatesan, and Prasanna Parthasarathy have been simply great in supporting me through this time. Srikanth, Vishal, and Rohan awarded me doctorate during my first year of Ph.D. and I am happy to have earned it today.

My weekly badminton sessions with our club members were a great respite and kept me fresh and energized for research. I would like to thank Shawn Lam, Santhosh Parmeswaran, Prof. David Tan, Sushama Shivakumar, Kedar Sapkal, Trung Tran, and Sitthisa Surapass for all the great moments we shared on and off the courts.

Rishi Patil, Mayank Kapoor, Pratik Mehta, Harguneet Brar, Luvy Singh, Anurag and Sonika Jhalani, Roy Alexander, Akila Rajendran, Baiju John, and Ketan and Bhavana Parikh were like my family when I was in Switzerland and I am thankful to them for the amazing times we had.

Chintamani Tol, Amod Gokhale, and Dhawal and Utpal Bacholkar have been close friends since school. I would like to thank them for their support and encouragement and for being such great friends. Alok Tongaonkar, Suyog Lokhande, and

Shirish Kendre have been greatest sources of inspiration throughout this time. It's hard to imagine being at this stage without Alok and Suyog's support. I would like to thank them for being themselves.

Most importantly, I would like to thank my parents and extended family. This research would have been impossible without their unconditional support and love.

TABLE OF CONTENTS

LIST OF TABLES

LIST OF FIGURES

ABSTRACT

Weight and service life are often the two most important considerations in the design of structural components. This research incorporates a novel crack propagation analysis technique into shape optimization framework to support design of 2-D structural components under mixed-mode fracture for: (i) maximum service life subject to an upper limit on weight, and (ii) minimum weight subject to specified minimum service life. In both cases, structural performance measures are selected as constraints and CAD dimensions are employed as shape design variables. Fracture parameters, such as crack growth rate and crack growth direction are computed using extended finite element method (XFEM) and level set method (LSM).

XFEM is a computational technique in which special enrichment functions are used to incorporate the discontinuity of structural responses caused by crack surfaces and crack tip fields into finite element approximation. The LSM employs level set functions to track the crack during the crack propagation analysis. As a result, this method does not require highly refined mesh around the crack tip nor re-mesh to conform to the geometric shape of the crack when it propagates, which makes the method extremely attractive for crack propagation analysis.

However, shape sensitivity analysis for crack propagation involves calculating derivatives of enrichment functions employed in XFEM that are discontinuous or unsmooth. The proposed sensitivity analysis method in this study overcomes these issues

and calculates accurate derivatives of both crack growth rate and direction with respect to design variables. The proposed method employs (i) semi-analytical method for the derivatives of stresses and displacements, and (ii) material derivatives for the SIFs obtained from the domain form of the interaction integral, and therefore, the crack growth rate and direction. The method enables computation of sensitivity coefficients of fracture parameters for a growing crack and is up to 40% faster than the commonly used finite-difference method.

Two different optimization approaches—a batch-mode, gradient-based, nonlinear optimization and an interactive what-if analysis—are used for optimization. An engine connecting rod example is used to demonstrate the feasibility and accuracy of the proposed method. The design optimization process can successfully handle arbitrary 2-D geometries and can solve general design problems that are most commonly encountered, such as design for maximum life and design for minimum weight.

Chapter 1

INTRODUCTION

1.1 Background and motivation

Failure of components due to fatigue and fracture is a major issue that spans across several engineering disciplines and costs hundreds of billions of dollars (NBS, 1983). Structural components commonly observed in aerospace and mechanical industries are obvious examples where crack growth could lead to downtime or failure and may even result in substantial damage and loss of life. The Liberty ships (Bannerman & Young, 1946), Comet Aircraft incident (Wells, 1955), Aloha Airlines accident (NTSB, 1989), and the Sioux City DC-10 crash (NTSB, 1990) are some of the well-known incident of catastrophic failure due to fracture.

The mere presence of crack does not condemn a structure to be unsafe. In fact, the damage tolerant design and analysis approach takes into account the presence of flaws and predicts useful remaining service life (residual life) of components. It is a common practice to subject critical structural components to periodic inspections to identify presence of cracks and then monitor crack growth at certain intervals. Knowing the geometric shape of structure, flaw shape and size, material, and loading, in many cases it is possible to predict the period of sub-critical crack growth using crack propagation

analysis techniques. An example where cracks observed during periodic inspection in the nose landing gear strut resulted in grounding of an aircraft is shown in Figure 1.1.

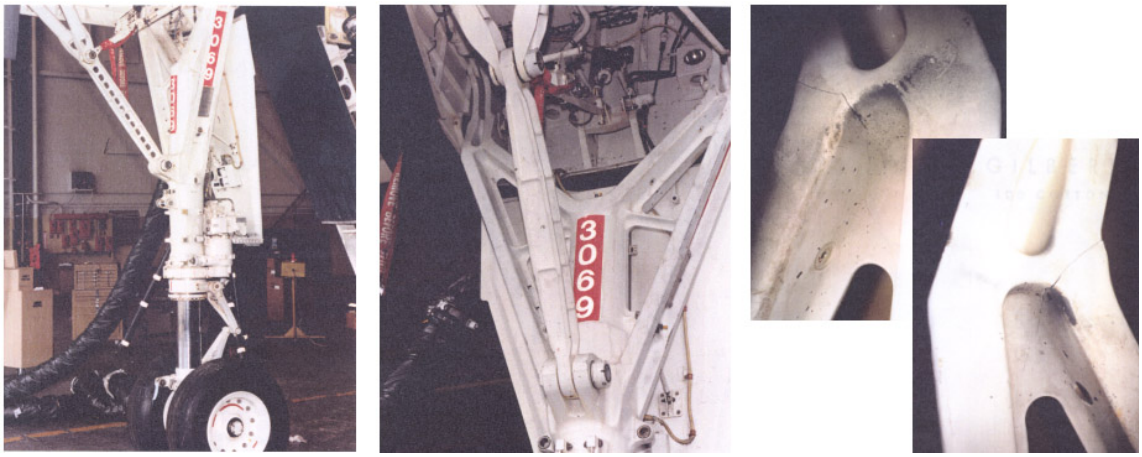

Figure 1.1 Cracks found in an airplane landing gear strut

A vast pool of empirical data and commercial software tools, such as AFGROW (Harter, 2008), MSC.Fatigue (MSC.Software, 2005), and NASGRO (SwRI, 2005), are available for crack propagation analysis for many commonly used geometric shapes, such as plates, pipes, and shafts. However, when it comes to crack propagation simulation for arbitrary 2-D geometries, currently available commercial software tools require significant manual efforts for mesh rearrangement and are computationally expensive. For crack propagation analysis of complex 3-D parts, such as the landing gear strut shown above, currently available commercial software tools are simply not adequate. The reasons behind this deficiency are elaborated in Section 1.4. An accurate and efficient software tool for crack propagation analysis is therefore necessary.

As mentioned earlier, geometric shape of the component, flaw size and shape, material, and loading (including environmental effects) are the four factors that influence

residual life of the components. Out of these, flaw shape and size are beyond designer's control and loading is determined by application for the most part. Hence geometry and material are the two parameters that designer can control to increase residual life. Material selection is usually dictated by cost, application, environment, availability and manufacturing processes. Hence, in addition to developing reliable and efficient crack propagation analysis capability, effect of geometric shape on crack propagation must be studied during the design stage in order to optimize shape of structural components for maximum service life. Such study will be useful in two ways: (i) for parts with pre-existing flaws, shape of the part can be optimized subject to given loads and initial flaw size, and material could be removed from or added to the part, if feasible, and (ii) by conducting crack initiation analysis during the design phase, most likely location and type of flaw can be estimated, and this information can be used for optimizing residual service life of the component.

One can argue that changing shape of a component will change stress pattern, and hence for the optimum design, the crack may not initiate at the same location as the initial design. While this may be true in many cases, there is an important class of structural components, such as connecting rod, turbine blades, gear teeth, aircraft wing panels, etc., for which the overall geometric shape is dictated primarily by functional requirements and interfacing components. For such components, there is only limited flexibility for changing shape of some local geometric features, and hence even with changes in shape of local features, the overall stress pattern remains similar to original design. This research will be instrumental in design of such components. For other cases, it will be helpful in identifying effect of shape changes on crack propagation.

This research aims at incorporating an accurate and efficient crack propagation simulation technique into structural shape optimization framework to facilitate design of structural components for maximum service life. This chapter presents an overview of the current state of the art related to these topics and briefly describes the proposed design process that effectively addresses aforementioned issues.

1.2 Shape optimization of cracked structures

The problem of crack propagation analysis in structural components has enjoyed great deal of popularity in the mechanics community; however, the issue of designing components for maximum service life has not received much attention. Some noteworthy attempts to include service life into shape optimization problem were made earlier. This section summarizes some such attempts made previously and distinguishes between those and the current work.

Han and Lim (2002) used the growth-strain method to optimize shape of components for prolonged service life. The growth-strain method is independent of boundary parameterization or sensitivity analysis. It optimizes shape of a structure by volume deformation occurring in the process of making a parametric variable (such as von Mises stress) uniform. The process was demonstrated using a compact tension (CT) specimen and a cantilever beam. The use of growth-strain method limited its application to simple geometries. Jones *et al.* (2002) presented a simple shape optimization algorithm with residual (fracture) strength as constraint; however, the objective was not to maximize service life. They indicated that in several cases, fracture based design optimization may yield a lighter structure than stress-based optimization, and emphasized

the need for a detailed study of this subject. Banichuk *et al.* (2005) presented a technique for solving the problem of axisymmetric shell optimization under fracture mechanics and geometric constraints. The objective was to minimize weight of brittle and quasi-brittle bodies subject to constraints on the cyclic loading for fatigue cracks using genetic algorithms. Miegroet *et al.* (2005) developed a generalized shape optimization method based on level set method and XFEM. Although their work dealt with shape optimization, it focused on shape and topology optimization of structures with voids—shape optimization for structures with cracks was not addressed. This method was found very promising for topology optimization where voids with simple geometric shape (circle, ellipse, rectangle, etc.) in the structure were represented using level sets. The main limitations were (i) use of finite difference method for sensitivity calculation, and (ii) its applicability to only the basic geometric shapes.

1.3 Shape sensitivity analysis of cracked structures

Design sensitivity analysis can be used by itself to reveal relationship between shape design variables and fracture parameters or it can be used to provide sensitivity coefficients to optimization algorithm for determining direction towards optimum design. In either case, it is a powerful technique to analyze effect of changes in shape design variables on fracture parameters. Several attempts to compute sensitivity of fracture parameters with respect to either shape design variables or crack geometry parameters were made. Some of the salient works are briefly discussed next.

Chang *et al.* (1997) solved a shape optimization problem in which the crack-initiation life was imposed as design constraint. Continuum-based material derivative

technique was used for computing sensitivity coefficients of structural parameters; whereas finite difference method was used to compute gradients of fatigue life. The method was demonstrated using a 3-D structural part. Saurin (2000) presented an adjoint variable method for computing sensitivity coefficients of fracture parameters. They computed fracture parameters using domain form of the well-known J-integral. Design sensitivity coefficients for plates under in-plane loading were computed for several different boundary variations. Taroco (2000) developed a continuum-based material derivative approach for shape sensitivity analysis of 2-D cracked bodies. He simulated crack propagation as a shape change of the cracked body and computed sensitivity coefficients of potential energy release rate with respect to unit crack advance.

Along similar lines, Chen *et al.* (2001) successfully demonstrated a continuum-based material derivative approach for calculating sensitivity coefficients of fracture parameters. This approach is useful in first and second order reliability methods (FORM and SORM) that are commonly used in probabilistic fracture mechanics. However, in their research only sensitivity analysis of SIFs for a given crack configuration was performed; crack growth rate and propagation direction were not considered. Thus, sensitivity computation for an evolving crack could not be performed. Also, the sensitivity coefficients of SIF's were computed with respect to crack length and no shape design variables were considered.

It was observed that although all of these techniques included fracture parameters in the shape optimization problem, none of them dealt with maximizing service life of structural components. The scope of their research was restricted to simple and standard shaped geometries. On the other hand, although some successful attempts for shape

sensitivity analysis of cracked structures were made, these were based on finite element method and suffer from the limitations described in section 1.4. Further, a majority of these computed sensitivity coefficients with respect to crack size, and not shape design variables. The principal problem behind this is suspected to be the tedious and computationally expensive re-meshing procedure required by then-existing numerical crack propagation analysis techniques. Hence the work for present research commenced with a review of computational fracture mechanics in order to find a suitable method that would overcome aforementioned limitations.

1.4 A brief review of computational fracture mechanics

Numerical methods are indispensible for analyzing mechanics of fracture as it is possible to derive closed-form solutions for fracture problems only for some simple geometric shapes. Over the span of past five decades, the field of computational fracture mechanics has steadily evolved. A comprehensive overview of the state of the art in crack propagation analysis can be found in (Mohammadi, 2008; Timbrel, Chandwani, & Cook, 2004). There are only a handful of methods, such as boundary integral method, boundary element method (Aliabadi, 1997), finite element method, and meshless methods, available for crack propagation study. Among them, the finite element method (FEM) is the most versatile and widely accepted. Numerous finite-element based techniques for solving crack propagation analysis problems exist, and an excellent review of those was presented by Bordas (2003) and Mohammadi (2008). Here, only a few finite element–based techniques are briefly mentioned to give the reader an idea about current capabilities.

1.4.1 Discrete inter-element crack

This approach models discontinuity by simply defining crack along element edges (Ngo & Scordelis, 1967; Nilson, 1968). However, the crack-tip singularity cannot be accounted for unless special singular finite elements are included in the model.

1.4.2 Discrete cracked element

This technique overcomes some limitations of the discrete inter-element crack method by allowing crack to be defined inside an element (Grootenboer, 1979; Saouma & Ingraffea, 1981). New mesh is created by splitting the cracked element and dividing adjacent elements to satisfy compatibility. State variables of the new elements are computed using state variables of the parent element.

1.4.3 Smeared crack model

In this technique, the crack is modeled implicitly by simulating the mechanical effects of crack in terms of strength or stiffness reduction of the model (Rots, Nauta, Kursters, & Blaauwendraad, 1985). The model is essentially treated as a continuum. Initially crack propagation path is determined, and appropriate changes in the model's compliance are made. Hence, it does not require re-meshing and is much more efficient than methods described earlier. However, its major drawbacks are that it cannot model crack surfaces. Also, representation of the cracked model as a continuum induces locked-in stresses in the elements close to the localization zone and hence there could be an artificial increase in the structural stiffness (Rots J. G., 1988).

1.4.4 Singular elements

Singular elements model the crack-tip singularity by collapsing the nearby midside node to the quarter points (Barosum, 1974; Benzley, 1974; Henshell & Shaw, 1975; Barosum, 1977). This is a very powerful technique and has been widely used since its inception for modeling crack-tip singularity using finite element method.

All of these methods have their advantages and disadvantages and no single method is capable of solving all types of problems. However, all of them are based on FEM, and FEM in its classic form, suffers from following disadvantages that make it cumbersome and unattractive to model crack-growth behavior.

- The mesh must conform to the discontinuity. This implies that every time the crack grows, the structure must be re-meshed.
- Highly refined mesh near crack-tip is required to accurately capture the high stress and displacement gradients observed in that region.
- Since the structure is being re-meshed during each crack-growth cycle, it becomes difficult to track local structural performance measures, such as displacements, during shape design optimization.
- It is nearly impossible or impractical to model crack growth for geometrically complex 3-D components due to the limitation of mesh-generators.
- The need for highly refined mesh and re-meshing greatly increases computational burden.

Development of a new class of methods called as generalized or enriched finite elements (Melenk, 1995) has proved to be a major breakthrough in solving problems involving discontinuity in the structure. These methods exploit the partition of unity

(Melenk & Babuska, 1996; Babuska & Melenk, 1997) property of the finite elements to enrich the approximation space so that the feature of interest (crack, bi-material interface, singularity, etc.) is naturally reproduced. It was shown by Melenk and Babuska (1996) that the use of such enrichment functions significantly improves convergence rate and accuracy of the solution. In the short period since their inception, these methods have gained a wide following in the computational mechanics community.

1.5 The eXtended Finite Element Method

In this research, one of the methods based on the partition of unity principle, the XFEM (Belytschko & Black, 1999), is employed for crack propagation analysis. In the XFEM, nodes surrounding the crack-tip region are enriched using four functions that span the near-tip asymptotic fields derived from linear elastic fracture mechanics (LEFM) theory. This facilitates representation of the crack independent of the finite element mesh and helps capture crack-tip fields accurately with minimal mesh refinement. Heaviside function is used to enrich the nodes whose support is cut by the crack. This helps incorporate the discontinuity across the crack surface.

The XFEM has been used to solve a variety of problems including crack growth analysis. Belytschko and Black (1999) first demonstrated application of the XFEM for modeling static fracture mechanics problems. Since then, the XFEM has been successfully used to model quasi-static crack propagation (Huang, Sukumar, & Prevost, 2003), dynamic crack propagation (Belytschko & Chen, 2004), cracks in Mindlin-Reissner plates (Dolbow, Moes, & Belytschko, 2000), cohesive crack growth (Moes & Belytschko, 2002), arbitrary branched and intersecting cracks (Daux, Moes, Dolbow,

Sukumar, & Belytschko, 2000), non-planar 3-D crack growth (Moes, Gravouil, & Belytschko, 2002; Gravouil, Moes, & Belytschko, 2002), and several other crack propagation problems. A more in-depth review of various developments and applications of XFEM can be found in (Dolbow, 1999; Chessa, 2002; Bordas, 2003). It was shown that combination of the XFEM with the level set method (LSM) provides an elegant scheme for modeling crack propagation (Stolarska, Chopp, Moes, & Belytschko, 2001).

1.6 Level set method

The LSM was introduced by Osher and Sethian (1988) to model moving interfaces. In this method, an interface of interest is represented as a zero-level set of a function that is of one higher dimension than the interface itself. The interface is modeled using implicit level-set functions and updating the position of the interface simply requires updating values of these functions. When implemented within the finite element framework, the level-set functions are stored at nodes, and are updated as the interface evolves. This computation takes place over a fixed mesh, meaning that the need to re-mesh the structure is completely obviated. Originally, the LSM was introduced for modeling closed interfaces (voids or inclusions in the structure, bi-material interfaces, etc.) and as such, were not suitable for modeling cracks, which can be described as open curves. Stolarska *et al.* (2001) modified the LSM to overcome this limitation. They employed one level set function to represent the crack surface and another to represent the crack front. The intersection of zero level sets of these two functions was used to represent the crack-tip.

To summarize, the XFEM necessitates minimal mesh refinement and the LSM eliminates the need for re-meshing. Thus, the combination of these two methods effectively addresses all of the FEM limitations discussed earlier, and is the method of choice for this research.

1.7 Design problem definition

With the sound analysis method in place, it is desirable to further extend the method to support design of structural components by optimizing geometric shape for maximum service life. It is assumed that initial crack size, shape, and location are specified and constant amplitude cyclic loading is applied. Two types of design problems are considered in this research. In the first design problem, the goal is to maximize service life of components subject to constraints on volume (which is analogous to weight) and structural performance measures. The design problem is defined as:

$$\begin{aligned} &\text{Maximize: } N(\mathbf{b}) \\ &\text{Subject to: } \mathbb{V}(\mathbf{b}) < \mathbb{V}^{max}, \psi_i(\mathbf{b}) \leq \psi_i^u \\ &b_j^\ell \leq b_j \leq b_j^u \end{aligned} \tag{1.1}$$

where N is the service life in number of load cycles; b_j are the shape design variables with lower and upper limits b_j^l and b_j^u, respectively; $\mathbb{V}$ is the volume with the upper limit of $\mathbb{V}^{max}$; and ψ_i are the constraints on structural performance measures, such as stresses.

The second design problem, which focuses on minimizing material subject to constraints on service life and structural performance measures, is defined as:

$$\text{Minimize: } \mathbb{V}(\mathbf{b})$$

$$\text{Subject to: } N(\mathbf{b}) > N^{min},\ \psi_i(\mathbf{b}) \leq \psi_i^u \qquad (1.2)$$

$$b_j^\ell \leq b_j \leq b_j^u$$

where N^{min} is the minimum required service life.

An overview of the design process is shown in Figure 1.2. For both design problems, the geometry of the structure is represented in CAD environment. The design variables employed for shape DSA are essentially the dimension parameters defined in CAD. A combination of XFEM and LSM is used for computing fracture parameters and for crack propagation analysis. A semi-analytical shape design sensitivity analysis (DSA) method developed in this research is used to calculate gradients of crack propagation rate and propagation direction with respect to geometric parameters that govern the shape of the structural components. The gradients are then supplied to an optimization algorithm that determines shape changes. Depending on problem type, the objective could be either maximum service life or minimum weight. The design is then updated and the process is repeated until optimum design is found. Since the geometry is defined in CAD environment, downstream processes, such as rapid prototyping, dimension verification, virtual manufacturing, and finally, physical prototyping using CNC can be readily carried out.

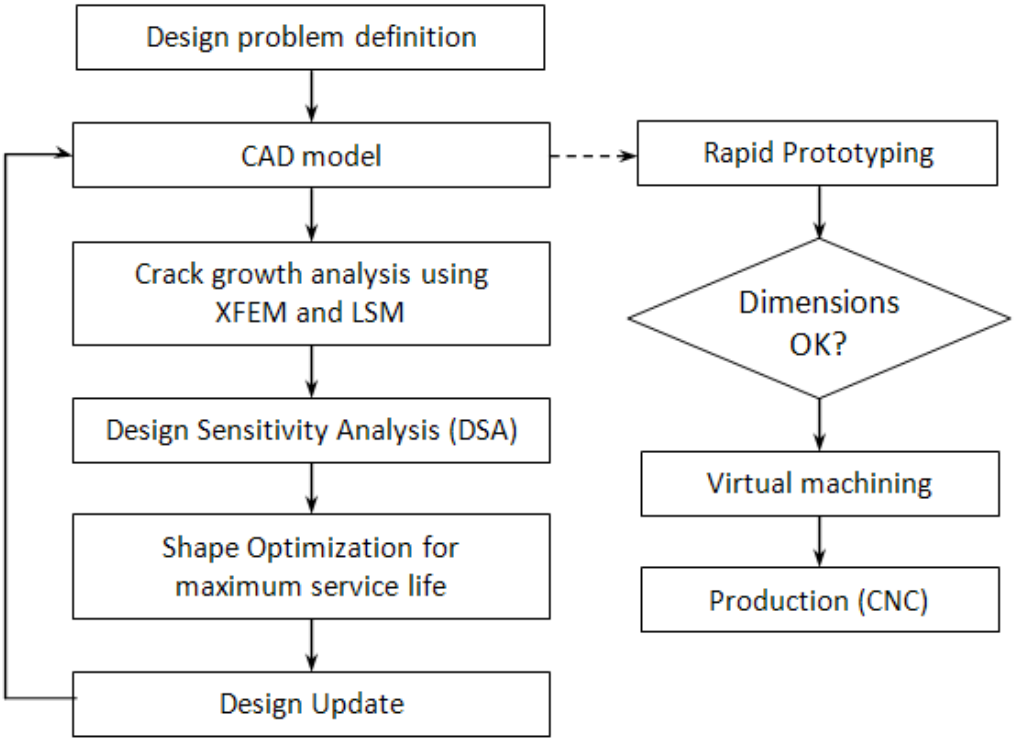

Figure 1.2 Proposed shape optimization process for maximizing service life of structural components

The remainder of the dissertation is organized as follows. Chapter 2 briefly discusses the fracture mechanics concepts used in this study. The fracture mechanics theory used for this research is discussed and the crack growth laws are reviewed. Computation of SIFs that determine the crack growth parameters using interaction energy integral technique is also presented.

XFEM and LSM theories are discussed in more detail in Chapter 3. Incorporation of these methods into the finite element framework is described. The enrichment functions used are explained briefly. Special considerations required for the implementation of these methods for crack propagation analysis is explained in detail.

The computational code available for XFEM-LSM methods was only capable of performing static analysis. This code was extended to model crack propagation. The accuracy of this code is demonstrated using an example and the comparison of results against reference solution is also shown. A detailed study was conducted to determine correct level of mesh refinement and crack growth increment size. Results for this study are presented at the end of this chapter.

Chapter 4 is devoted to the discussion on design sensitivity analysis. First, design velocity field, which is used for updating finite element mesh during design optimization process, is briefly explained. Different methods considered for evaluation of sensitivity coefficients of fracture parameters are presented. The semi-analytical method developed in this research for DSA is explained in detail. DSA results for two numerical examples are shown to demonstrate accuracy and efficiency of the semi-analytical method.

Chapter 5 explains the optimization process in detail. The feasibility and scope of the proposed design process is demonstrated using an engine connecting-rod example. Results for the two design problems discussed earlier using two different optimization methods—batch-mode optimization and interactive what-if study—are presented.

Finally, Chapter 6 concludes this research and identifies enhancements and scope for further extension of this design process for 3-D problems.

Chapter 2

LINEAR ELASTIC FRACTURE MECHANICS

The problem of modeling crack propagation has been of considerable interest to the mechanics community. In earlier stages of fracture mechanics, the techniques developed for estimating fracture parameters heavily relied on empirical knowledge. Since it is not possible to extensively test each and every component, certain standard specimens were tested and the data required for computation of fracture parameters was made available. However, since then, structural components have become increasingly complex in terms of geometry—partly due to advances in manufacturing processes, and partly due to advanced modeling tools and simulation-based design techniques. Although the empirical knowledge based techniques were (and still are) applicable for many commonly used components, the increasing geometric complexity and the need to reduce cost call for more advanced crack propagation analysis techniques. It also reiterates the need to understand of effect of geometric shape on crack propagation.

2.1 Scope of linear elastic fracture mechanics

A detailed and authoritative discussion on LEFM theory can be found in (Anderson, 1985). Limitations of LEFM are discussed here to define scope of this research. LEFM is a branch of fracture mechanics that deals with problems in which the size of the plastic

zone around the crack tip is very small in comparison to the domain size. LEFM holds well for the brittle mode of fracture, which governs the fracture until the SIFs are less than the material fracture toughness. Fracture in metals after this point is usually accompanied by significant plastic yielding and since LEFM is unable to analyze crack growth in such cases, it yields conservative estimate of life. However, for a majority of common structural applications, fracture toughness is still considered as the failure criteria. Due to this fact, and due to its simplicity, LEFM is widely used and is also adopted in this study.

2.2 Crack-tip opening modes

The three independent movements of the upper and lower crack surfaces with respect to each other (corresponding to three independent cases of loading) define the three crack opening modes as shown in Figure 2.1.

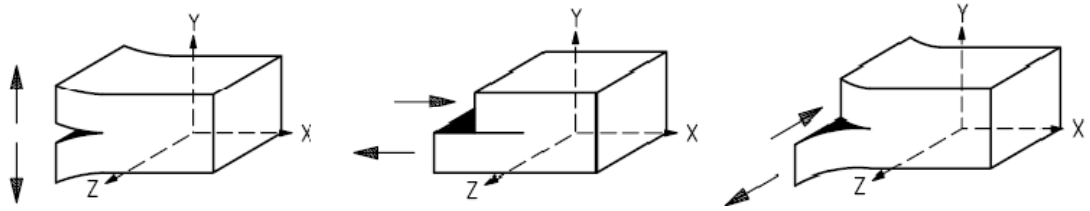

a) Mode I: Crack opening b) Mode II: Crack Shearing c) Mode III: Crack Tearing

Figure 2.1 Modes of crack tip opening

The strength of stress singularity near the crack-tip region in each mode is characterized by the stress intensity factor (SIF) for that mode. The SIFs for the three modes are denoted by $K_{\mathrm{I}}, K_{\mathrm{II}},$ and K_{III}. In a general case, more than one mode of loading may be present, and the crack tip fields can be modeled by an appropriate linear

combination of those corresponding to these three modes. Such problems are called mixed-mode problems. In this research, only planar components are considered and hence further discussion would be limited to the first two modes.

2.3 Mixed-mode crack-tip fields

According to LEFM theory, the crack-tip fields are given by Eq. (2.2) through Eq. (2.5) (Anderson, 1985). In these expressions, (r, θ) are used to define location of a point in local crack-tip coordinate system (shown in Figure 2.2), μ is the shear modulus, ν is Poisson's ratio, and κ is the Kolosov coefficient, whose value is given by

$$\kappa = 3 - 4\nu \text{ for plane strain;} \qquad \text{and} \qquad \kappa = \frac{3-\nu}{1+\nu} \text{ for plane stress} \tag{2.1}$$

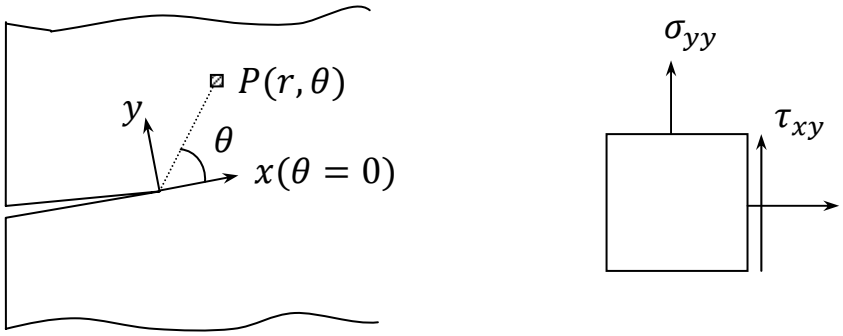

Figure 2.2 Crack-tip coordinate system

Stress fields for a crack under pure mode I loading are given by

$$\begin{Bmatrix} \sigma_{xx} \\ \sigma_{yy} \\ \tau_{xy} \end{Bmatrix} = \frac{K_I}{\sqrt{2\pi r}} \cos\frac{\theta}{2} \begin{Bmatrix} 1 - \sin\frac{\theta}{2}\sin\frac{3\theta}{2} \\ 1 + \sin\frac{\theta}{2}\sin\frac{3\theta}{2} \\ \sin\frac{\theta}{2}\cos\frac{\theta}{2}\cos\frac{3\theta}{2} \end{Bmatrix} \tag{2.2}$$

And the associated compatible displacement fields are as follows:

$$\begin{Bmatrix} u_x \\ u_y \end{Bmatrix} = \frac{K_I}{2\mu}\sqrt{\frac{r}{2\pi}} \begin{Bmatrix} cos\frac{\theta}{2}\left[\kappa - 1 + 2sin^2\frac{\theta}{2}\right] \\ sin\frac{\theta}{2}\left[\kappa + 1 - 2cos^2\frac{\theta}{2}\right] \end{Bmatrix} \tag{2.3}$$

Stress fields for a crack under pure mode II loading are given by

$$\begin{Bmatrix} \sigma_{xx} \\ \sigma_{yy} \\ \tau_{xy} \end{Bmatrix} = \frac{K_{II}}{\sqrt{2\pi r}} \begin{Bmatrix} -sin\frac{\theta}{2}\left[2 + cos\frac{\theta}{2}cos\frac{3\theta}{2}\right] \\ sin\frac{\theta}{2}cos\frac{\theta}{2}cos\frac{3\theta}{2} \\ cos\frac{\theta}{2}\left[1 - sin\frac{\theta}{2}sin\frac{3\theta}{2}\right] \end{Bmatrix} \tag{2.4}$$

And the associated compatible displacement fields are as follows:

$$\begin{Bmatrix} u_x \\ u_y \end{Bmatrix} = \frac{K_{II}}{2\mu}\sqrt{\frac{r}{2\pi}} \begin{Bmatrix} sin\frac{\theta}{2}\left[\kappa + 1 + 2cos^2\frac{\theta}{2}\right] \\ cos\frac{\theta}{2}\left[\kappa - 1 - 2sin^2\frac{\theta}{2}\right] \end{Bmatrix} \tag{2.5}$$

It can be observed from these equations that the near-tip stresses and displacements are completely determined by the stress intensity factors. Numerical computation of SIFs is discussed in section 2.5.

2.4 Quasi-static fatigue crack growth

2.4.1 Crack growth rate regions

Fatigue crack growth here refers to the crack growth under constant-amplitude cyclic loading conditions. A plot of crack growth rate per cycle da/dN against stress intensity factor range ΔK is shown in Figure 2.3. The curve can be divided into three regions (Zahavi & Torbilo, 1996).

- Crack initiation region: In the first region, crack initiation occurs when the ΔK exceeds threshold value, ΔK_{th}. At this point, the slope of the curve becomes constant.
- Linear Crack Propagation: This region exhibits linear relationship between ΔK and $\log(da/dN)$, and the crack growth takes place according to the Paris law (Paris, Gomez, & Anderson, 1961). This region corresponds to the useful service life for most structural components, and is the focus of this research. The Paris law remains valid until $\Delta K < \Delta K_c$, where ΔK_c is the fracture toughness of the material.
- Overload Failure: In the last region, accelerated crack growth rate is observed, and even a small increment in ΔK may result in a rapid crack growth, and eventually, failure. The plastic zone ahead of the crack tip is significant in size, and must be taken into account while predicting crack growth in this region.

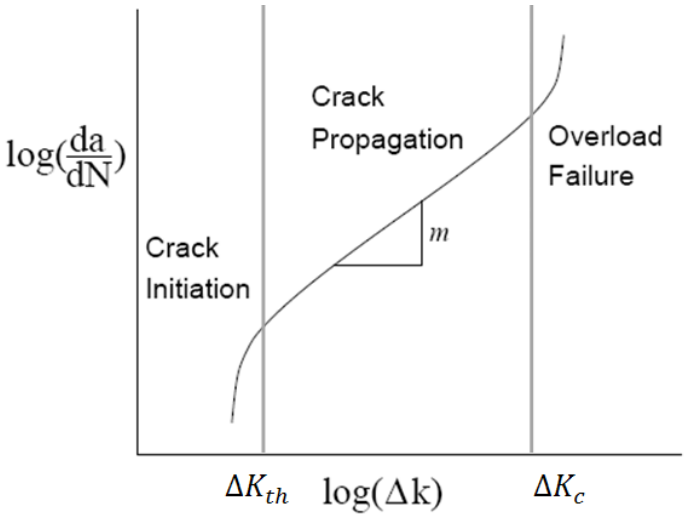

Figure 2.3 Three regions of crack growth rate

2.4.2 Paris law for fatigue crack growth

Paris *et al.* (1961) presented an empirical law that relates fatigue crack growth to LEFM. For a given fatigue loading, assume that $\Delta K = K_{max} - K_{min}$ is the SIF range. Suppose that the crack grows by amount Δa in ΔN cycles. Crack growth rate is related to ΔK as follows:

$$\frac{\Delta a}{\Delta N} \approx \frac{da}{dN} = C(\Delta K)^m \tag{2.6}$$

where C and m are material constants. For general mixed-mode loading, ΔK is replaced by an equivalent SIF range, ΔK_{eq}, given by

$$\Delta K_{eq} = \sqrt{\Delta K_{\mathrm{I}}^2 + \Delta K_{\mathrm{II}}^2} \tag{2.7}$$

Usually, the crack growth per cycle Δa is very small—almost of the order of 10^{-8} in (Anderson, 1985). Hence, instead of computing crack growth in each cycle, it is a common practice to predetermine the value of Δa. As a thumb rule, $\Delta a = a/10$, where a is the initial crack length. It is assumed that other fracture parameters would remain constant while crack propagates through this increment. If the crack has small curvature, smaller values of Δa can be selected. Once Δa is fixed, the only unknown is the corresponding number of cycles, which is computed using the following equation.

$$\Delta N = \frac{\Delta a}{C(\Delta K_{eq})^m} \tag{2.8}$$

Note that in some cases, an initial analysis may be required to determine the crack trajectory and an adjustment in Δa value may be required.

2.4.3 Crack growth direction

Along with crack growth rate, crack propagation angle (θ_c) is the other necessary parameter in modeling crack propagation. Some of the commonly used criteria for determining crack growth angle are:

- The maximum energy release rate criterion (Nuismer, 1975);
- The maximum circumferential (hoop) stress criterion or the maximum principal stress criterion (Erdogen & Sih, 1963); and
- The minimum strain energy density criterion (Sih, 1973).

The maximum hoop stress criterion, which states that the crack will propagate in a direction where the hoop stress ($\sigma_{\theta\theta}$) is maximum, is used in this study. The expression for θ_c, obtained by setting the shear stress from Eq. (2.2) and Eq. (2.4) to zero, is given as:

$$\theta_c = 2\ arctan\ \left(\frac{1}{4}(K_I/K_{II} \pm \sqrt{(K_I/K_{II})^2 + 8}\right) \tag{2.9}$$

It can be seen from Eq. (2.8) and Eq. (2.9) that ΔN and θ_c are functions of K_{I} and K_{II}, whose calculation is discussed next.

2.5 Calculation of stress intensity factors

The stress intensity factors depend on component geometry, loading, and the initial crack geometry. For commonly observed simple geometries (plates, shafts, pipes, etc.) SIFs can be determined using the vast pool of empirical data. However, accuracy of these empirical relations fades away as geometric complexity of the components increases and for the components such as the landing gear shown in Figure 1.1, different techniques

must be devised. The advancements in numerical techniques, such as the FEM, the boundary element method, and meshless methods, have been a great boon for developing such techniques. A slew of numerical techniques have been developed to estimate SIFs. Some of the commonly employed techniques are: Virtual crack extension (VCE) (deLorenzi, 1982; 1985); Virtual crack closure integral (VCCI) (Buchholz, Grebner, Dreyer, & Krome, 1988; Chow & Atluri, 1995); Quarter point element stress (QPES) (Buchholz, Chergui, & Dhondt, 1999); and J-integral (Rice, 1968) converted into domain form (Stern, Becker, & Dunham, 1976; Shih, Moran, & Nakamura, 1986; Moran & Shih, 1987; Moran & Shih, 1987; Shih & Asaro, 1988; Nishikov & Atluri, 1987).

J-integral method is especially popular for evaluation of mixed-mode SIFs and is adopted in this study for the following reasons:

- It involves evaluation of a path-independent contour integral, and thus, it yields good results for widely different meshes (Dhondt, 2001).
- The required data for evaluation of the integral is readily available from numerical solution of the boundary value problem, and thus can be easily incorporated into any finite element code. In fact, this method was recently incorporated into the commercial finite element code, ABAQUS (Courtin, Gardin, Bezine, & Ben Hadj Hamouda, 2005).
- Unlike VCE, VCCI, and QPES, this method does not require any adjustment or rearrangement of the mesh near crack-tip.

2.5.1 J-integral

J-integral is basically a path independent contour integral around the crack tip. Its use as a fracture parameter was put forth by Rice (1968). J-integral is given by

$$J = \int_{\Gamma} \left[W\delta_{1j} - \sigma_{ij} \frac{\partial z_i}{\partial x_1} \right] n_j d\Gamma \tag{2.10}$$

where W is the strain energy density; σ_{ij} is the Cauchy stress tensor; and n_j is the outward normal to an arbitrary contour Γ around the crack tip as shown in Figure 2.4.

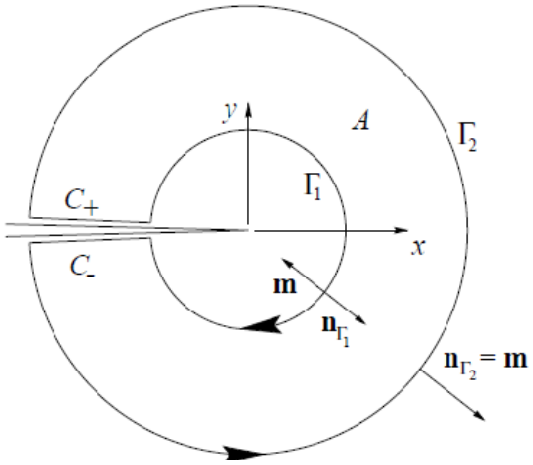

Figure 2.4 Path independent closed contour around the crack tip

Physically, J-integral may be interpreted as the energy flowing through the contour Γ per unit crack advance. Under elastic conditions, the J-integral is equivalent to Griffith's energy release rate (Anderson, 1985), and its relation to the stress intensity factors for 2-D cases is given by

$$G = J = \int_{\Gamma} \left[W\delta_{1j} - \sigma_{ij} \frac{\partial z_i}{\partial x_1} \right] n_j d\Gamma = \frac{1}{E^*}(K_I^2 + K_{II}^2) \tag{2.11}$$

As seen above, J-integral evaluation directly yields energy release rate and cannot distinguish between contributions due to crack opening and crack shearing modes. To overcome this difficulty, a conservation integral for two kinematically admissible states (actual and auxiliary), is computed (Yau, Wang, & Corten, 1980). Further, it is more

convenient to perform integration over an area than a contour from finite element standpoint. Hence, J-integral is converted to a domain form by applying divergence theorem.

2.5.2 Domain form of J-integral

Consider Eq. (2.10) written on a closed contour with a weight function q introducd in the integrand

$$J' = \int_{\Gamma} \left[W\delta_{1j} - \sigma_{ij}\frac{\partial z_i}{\partial x_1}\right] m_j q d\Gamma \tag{2.12}$$

where m_j is the outward normal to the closed contour Γ. The weight function q is defined as

$$q = \begin{cases} 1 & \text{on } \Gamma_1 \\ 0 & \text{on } \Gamma_2 \\ \text{arbitrary} & \text{otherwise} \end{cases} \tag{2.13}$$

Since $q = 0$ on Γ_2 and the integrand vanishes on C_+ and C_-, the closed contour integral in Eq. (2.12) reduces to a contour integral on Γ_1. Applying divergence theorem to Eq. (2.12) yields the following domain (area) integral.

$$J' = \int_A \left\{\frac{\partial}{\partial x_j}\left[W\delta_{1j} - \sigma_{ij}\frac{\partial z_i}{\partial x_1}\right] q + \left[W\delta_{1j} - \sigma_{ij}\frac{\partial z_i}{\partial x_1}\right]\frac{\partial q}{\partial x_j}\right\} dA \tag{2.14}$$

The first term vanishes for linear elastostatics. Comparing Eq. (2.12) and Eq. (2.14) and reversing normal m_j in Eq. (2.12) to be the outward normal $n_{\Gamma 1}$ leads to

$$\int_{\Gamma} \left[W\delta_{1j} - \sigma_{ij}\frac{\partial z_i}{\partial x_1}\right] m_j q d\Gamma = \int_A \left[\sigma_{ij}\frac{\partial z_i}{\partial x_1} - W\delta_{1j}\right]\frac{\partial q}{\partial x_j} dA \tag{2.15}$$

Thus, the domain form of J-integral is

$$J = \int_A \left[\sigma_{ij}\frac{\partial z_i}{\partial x_1} - W\delta_{1j}\right]\frac{\partial q}{\partial x_j}dA \tag{2.16}$$

2.5.3 Interaction energy integral

As pointed out earlier, the evaluation of J-integral does not give separate values of mode I and mode II SIFs. Yau *et al.* (1980) proposed an interaction integral technique, in which two kinematically admissible states of a body are superimposed to extract the mixed-mode SIFs.

Consider two independent equilibrium states of a cracked body. State 1 is defined as the actual state for the given boundary conditions, while state 2 is an auxiliary state which will be explained later. The J-integral for the two superposed states is

$$J^{(1+2)} = \int_\Gamma \left[W^{(1+2)}\delta_{1j} - \left(\sigma_{ij}^{(1)} + \sigma_{ij}^{(2)}\right)\frac{\partial\left(z_i^{(1)}+z_i^{(2)}\right)}{\partial x_1}\right]n_j d\Gamma \tag{2.17}$$

where the total strain energy is

$$W^{(1+2)} = \frac{1}{2}\left(\sigma_{ij}^{(1)} + \sigma_{ij}^{(2)}\right)\left(\varepsilon_{ij}^{(1)} + \varepsilon_{ij}^{(2)}\right) \tag{2.18}$$

Eq. (2.17) can be expanded and rearranged as

$$\begin{aligned} J^{(1+2)} = {} & \int_\Gamma \left[W^{(1)}\delta_{1j} - \sigma_{ij}^{(1)}\frac{\partial z_i^{(1)}}{\partial x_1}\right]n_j d\Gamma + \int_\Gamma \left[W^{(2)}\delta_{1j} - \sigma_{ij}^{(2)}\frac{\partial z_i^{(2)}}{\partial x_1}\right]n_j d\Gamma + \\ & \int_\Gamma \left[W^{(1,2)}\delta_{1j} - \sigma_{ij}^{(1)}\frac{\partial z_i^{(2)}}{\partial x_1} - \sigma_{ij}^{(2)}\frac{\partial z_i^{(1)}}{\partial x_1}\right]n_j d\Gamma \\ & \therefore J^{(1+2)} = J^{(1)} + J^{(2)} + M^{(1,2)} \end{aligned} \tag{2.19}$$

Here $J^{(1)}$and $J^{(2)}$ are the J-integrals for actual state and auxiliary state, respectively, and $M^{(1,2)}$ is the interaction integral for the two equilibrium states.

$$M^{(1,2)} = \int_{\Gamma} \left[W^{(1,2)} \delta_{1j} - \sigma_{ij}^{(1)} \frac{\partial z_i^{(2)}}{\partial x_1} - \sigma_{ij}^{(2)} \frac{\partial z_i^{(1)}}{\partial x_1} \right] n_j d\Gamma \tag{2.20}$$

$W^{(1,2)}$ is the interaction strain energy

$$W^{(1,2)} = \frac{1}{2}\left(\sigma_{ij}^{(1)} \varepsilon_{ij}^{(2)} + \sigma_{ij}^{(2)} \varepsilon_{ij}^{(1)} \right) = \sigma_{ij}^{(1)} \varepsilon_{ij}^{(2)} = \sigma_{ij}^{(2)} \varepsilon_{ij}^{(1)} \tag{2.21}$$

Just like J-integral, the interaction integral is converted into domain form.

$$M^{(1,2)} = \int_{A} \left[\sigma_{ij}^{(1)} \frac{\partial z_i^{(2)}}{\partial x_1} + \sigma_{ij}^{(2)} \frac{\partial z_i^{(1)}}{\partial x_1} - W^{(1,2)} \delta_{1j} \right] \frac{\partial q}{\partial x_j} dA \tag{2.22}$$

Expanding individual terms yields:

$$\begin{aligned} M^{(1,2)} = & \int_{A} \left[\sigma_{11}^{(1)} \frac{\partial z_1^{(2)}}{\partial x_1} \frac{\partial q}{\partial x_1} + \sigma_{12}^{(1)} \frac{\partial z_1^{(2)}}{\partial x_1} \frac{\partial q}{\partial x_2} + \sigma_{21}^{(1)} \frac{\partial z_2^{(2)}}{\partial x_1} \frac{\partial q}{\partial x_1} + \sigma_{22}^{(1)} \frac{\partial z_2^{(2)}}{\partial x_1} \frac{\partial q}{\partial x_2} \right] dA \\ & + \int_{A} \left[\sigma_{12}^{(2)} \frac{\partial z_1^{(1)}}{\partial x_1} \frac{\partial q}{\partial x_2} + \sigma_{22}^{(2)} \frac{\partial z_2^{(1)}}{\partial x_1} \frac{\partial q}{\partial x_2} - \sigma_{12}^{(2)} \frac{\partial z_1^{(1)}}{\partial x_2} \frac{\partial q}{\partial x_1} - \sigma_{22}^{(2)} \frac{\partial z_2^{(1)}}{\partial x_2} \frac{\partial q}{\partial x_1} \right] dA \end{aligned} \tag{2.23}$$

Rewriting Eq. (2.23) as follows,

$$M^{(1,2)} = \int_{A} h dA \tag{2.24}$$

where $h = h_1 + h_2 + h_3 + h_4 + h_5 + h_6 - h_7 - h_8$ and $h_i,\ i = 1$ to 8 are given as:

$$\begin{aligned} h_1 &= E_1 \left[\nu_1 \frac{\partial z_1^{(1)}}{\partial x_1} + \nu_2 \frac{\partial z_2^{(1)}}{\partial x_2} \right] \frac{\partial z_1^{(2)}}{\partial x_1} \frac{\partial q}{\partial x_1} & h_2 &= E_2 \left[\frac{\partial z_1^{(1)}}{\partial x_2} + \frac{\partial z_2^{(1)}}{\partial x_1} \right] \frac{\partial z_1^{(2)}}{\partial x_1} \frac{\partial q}{\partial x_2} \\ h_3 &= E_2 \left[\frac{\partial z_1^{(1)}}{\partial x_2} + \frac{\partial z_2^{(1)}}{\partial x_1} \right] \frac{\partial z_2^{(2)}}{\partial x_1} \frac{\partial q}{\partial x_1} & h_4 &= E_1 \left[\nu_2 \frac{\partial z_1^{(1)}}{\partial x_1} + \nu_1 \frac{\partial z_2^{(1)}}{\partial x_2} \right] \frac{\partial z_2^{(2)}}{\partial x_1} \frac{\partial q}{\partial x_2} \\ h_5 &= \sigma_{12}^{(2)} \frac{\partial z_1^{(1)}}{\partial x_1} \frac{\partial q}{\partial x_2} & h_6 &= \sigma_{22}^{(2)} \frac{\partial z_2^{(1)}}{\partial x_1} \frac{\partial q}{\partial x_2} \\ h_7 &= \sigma_{12}^{(2)} \frac{\partial z_1^{(1)}}{\partial x_2} \frac{\partial q}{\partial x_1} & h_8 &= \sigma_{22}^{(2)} \frac{\partial z_2^{(1)}}{\partial x_2} \frac{\partial q}{\partial x_1} \end{aligned} \tag{2.25}$$

Factors E_1, E_2, ν_1, and ν_2 depend on stress state. For plane stress, $E_1 = E/(1-\nu^2)$, $E_2 = E/2(1+\nu)$, $\nu_1 = 1$, and $\nu_2 = \nu$. For plane strain, $E_1 = E/(1+\nu)(1-2\nu)$, $E_2 = E/2(1+\nu)$, $\nu_1 = (1-\nu)$, and $\nu_2 = \nu$.

Eq. (2.11) for the superposed state can be written as

$$J^{(1+2)} = \frac{2}{E^*}\left(\left(K_I^{(1)}\right)^2 + \left(K_{II}^{(1)}\right)^2\right) + \left(\left(K_I^{(2)}\right)^2 + \left(K_{II}^{(2)}\right)^2\right) + \left(K_I^{(1)}K_I^{(2)} + K_{II}^{(1)}K_{II}^{(2)}\right) \tag{2.26}$$

$$\therefore J^{(1+2)} = J^{(1)} + J^{(2)} + \frac{2}{E^*}\left(K_I^{(1)}K_I^{(2)} + K_{II}^{(1)}K_{II}^{(2)}\right)$$

Comparing Eq. (2.19) to Eq. (2.26), following relationship is obtained

$$\therefore M^{(1,2)} = \frac{2}{E^*}\left(K_I^{(1)}K_I^{(2)} + K_{II}^{(1)}K_{II}^{(2)}\right) \tag{2.27}$$

where $M^{(1,2)}$ is computed using Eq.(2.22).

2.5.4 Stress intensity factors computation

Now that we have a relation between interaction integral and SIFs, obtaining individual SIFs involves making appropriate choice of the auxiliary state. To obtain mode I SIF, the auxiliary state is chosen to be the pure mode I asymptotic condition from Eq. (2.2) with $K_{\mathrm{I}}^{(2)} = 1$ and $K_{\mathrm{II}}^{(2)} = 0$. Substituting this in Eq. (2.27) gives

$$M^{(1,2)} = \frac{2}{E^*}K_I^{(1)} \tag{2.28}$$

$M^{(1,2)}$ can be calculated from Eq. (2.22). Hence mode I SIF is given by

$$K_I^{(1)} = \frac{E^*}{2}M^{(1,Mode\ I)} \tag{2.29}$$

Similarly, mode II stress intensity factors is obtained by selecting the auxiliary state to be the mode II asymptotic solution from Eq. (2.4) with $K_{\mathrm{I}}^{(2)} = 1$ and $K_{\mathrm{II}}^{(2)} = 0$.

$$K_{II}^{(1)} = \frac{E^*}{2} M^{(1,Mode\ II)} \tag{2.30}$$

Note that the asymptotic fields used for the auxiliary state are valid for LEFM only, and hence the interaction integral method presented here is also applicable only for LEFM.

Chapter 3

XFEM AND LSM FOR CRACK PROPAGATION

3.1 The Level Sets Method

3.1.1 Introduction to the LSM

Excellent description for LSM can be found in (Stolarska, Chopp, Moes, & Belytschko, 2001; Osher & Sethian, 1988). The discussion here closely follows these sources, but pertains to the scope of this research. Consider a closed, non-intersecting, moving interface Γ modeled as a zero level set of a function $\psi(\boldsymbol{x}(t), t)$.

$$\Gamma(x) = \{\boldsymbol{x} \in \mathbb{R}^2 : \psi(\boldsymbol{x}, t) = 0\} \tag{3.1}$$

Notice that the level set function $\psi(\boldsymbol{x}, t)$ is one higher dimension than the interface itself. The evolution equation of Γ can then be expressed as the evolution equation of ψ by taking time derivative of $\psi(\boldsymbol{x}(t), t) = 0$. The resulting equation of motion of the interface is

$$\psi_t + \boldsymbol{F}\|\nabla\psi\| = 0 \qquad (\text{Assuming } \psi(\boldsymbol{x}, t = 0) \text{ is given}) \tag{3.2}$$

Here $\boldsymbol{F}$ is the speed of the front at $\boldsymbol{x} \in \Gamma(t)$ in the direction normal to the interface, and $\|\nabla\psi\| \equiv 1$ by construction. A signed distance function defined below is used as a level set function in this research.

$$\psi(\boldsymbol{x},t) = d(\boldsymbol{x}) = \pm\, min\, \|\boldsymbol{x} - \boldsymbol{x}_\Gamma\|\,,\ \boldsymbol{x}_\Gamma \in \Gamma(t) \tag{3.3}$$

The sign of the distance function depends on which side of the interface point $\boldsymbol{x}$ is located. Since the LSM is implemented here within the finite element framework, signed distance functions for the crack are calculated with respect to finite element nodes.

3.1.2 Representation of crack using LSM

For this research, the crack Γ_c is considered as a one dimensional curve evolving in a two-dimensional domain Ω as shown in Figure 3.1. Since the crack is an open curve, two orthogonal level-set functions are required to represent it. The first level set function, $\psi(\boldsymbol{x},t)$, is normal to the crack and zero level set of this function represents the crack surface. The other level set function, $\phi(\boldsymbol{x},t)$, is tangent to the crack at the crack tip. Although the crack tip lies inside the domain, the level set function that represents crack front must initially be constructed up to the structure boundary. Hence, for calculating the level set, the crack is tangentially extended up to the boundary. The crack is represented by a set of points

$$\Gamma_c = \{\boldsymbol{x} \in \mathbb{R}^2 \mid \psi(\boldsymbol{x},t) = 0 \qquad and \qquad \phi(\boldsymbol{x},t) \leq 0\} \tag{3.4}$$

For a crack that lies completely inside a structure, two tangential level-sets, $\phi_1(\boldsymbol{x},t)$ and $\phi_2(\boldsymbol{x},t)$, are used. The crack tip(s) is (are) located at the intersection of zero level sets of these two orthogonal signed distance functions. The values of the level-sets are stored at nodes and are interpolated using the regular FEM displacement shape functions, N_j.

$$\psi(\boldsymbol{x},t) = \sum_{j\epsilon J} \psi_j(\boldsymbol{x},t) N_j(\boldsymbol{x})\,; \qquad \phi_i(\boldsymbol{x},t) = \sum_{j\epsilon J} \phi_{ij}(\boldsymbol{x},t) N_j(\boldsymbol{x}) \tag{3.5}$$

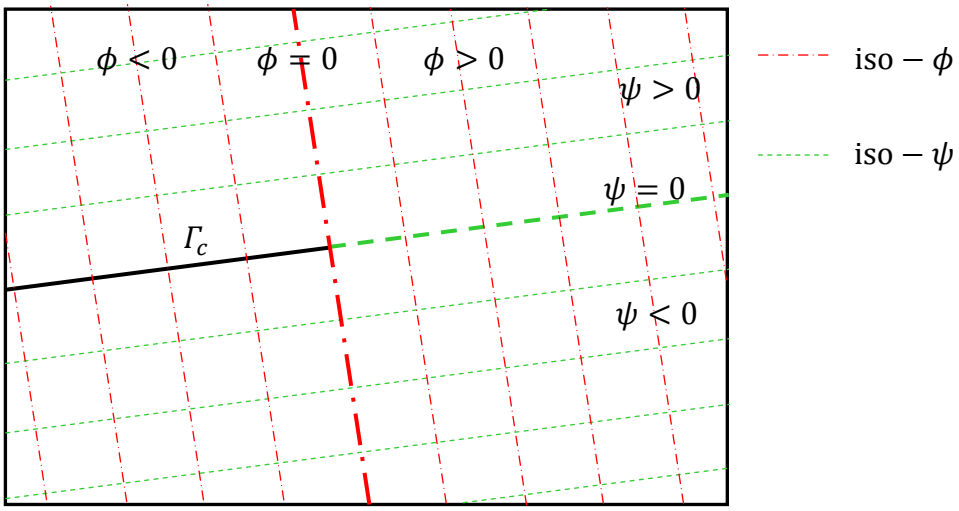

Figure 3.1 Level sets illustration

3.1.3 Level sets update

It is assumed that once a part of crack forms, it will not change its position or geometry. Since we are only concerned with crack propagation, it is sufficient to update level set values in a narrow region surrounding the crack. The narrow region for level sets update is built by surrounding the crack by a predetermined layer of elements. It must be ensured that the layer of elements is larger than the predefined crack increment (Δa) to ensure that all elements affected by crack are included in level set computation.

The two parameters that characterize crack growth are the direction θ_c and the crack tip displacement given by a vector $\boldsymbol{F} = (F_x, F_y)$, where by construction, $\|\boldsymbol{F}\| \equiv \Delta a$. Assume that the current location of the crack tip is $\boldsymbol{x}_i = (x_i, y_i)$. Let the current values of the level sets be $\phi^n = \phi(\boldsymbol{x}_i, t = n)$ and $\psi^n = \psi(\boldsymbol{x}_i, t = n)$. The following procedure is performed to update the level sets:

Recall that in Eq. (3.2), $\boldsymbol{F}$ is always normal to the crack front. However, the new crack tip increment $\boldsymbol{F}$ may not be normal to the zero level set of ϕ^n. Hence, ϕ^n must be first rotated so that it becomes orthogonal to $\boldsymbol{F}$. The rotated level set is given by

$$\hat{\phi}^n = (x - x_i)\frac{F_x}{\|\boldsymbol{F}\|} + (y - y_i)\frac{F_y}{\|\boldsymbol{F}\|} \tag{3.6}$$

The crack is extended by computing new values of ψ^{n+1} in the region where $\hat{\phi}^n > 0$, which is the Ω^{update} region. The region where $\hat{\phi}^n < 0$ is $\Omega^{\text{no update}}$ region (see Figure 3.2).

$$\begin{aligned} \psi^{n+1} &= \psi^{n+1} \quad in\ \ \Omega^{no\ update} \\ \psi^{n+1} &= \pm\left|(x - x_i)\frac{F_y}{\|\boldsymbol{F}\|} + (y - y_i)\frac{F_x}{\|\boldsymbol{F}\|}\right| \quad \text{in } \Omega^{\text{update}} \end{aligned} \tag{3.7}$$

ϕ^{n+1} is then computed using Eq. (3.2) so that it correctly represents the updated crack tip location. The location the new crack tip can be determined by taking intersection of the updated level sets ϕ^{n+1} and ψ^{n+1}.

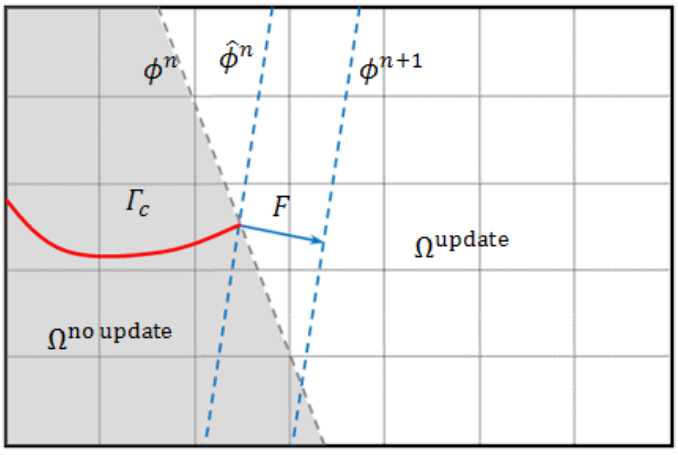

Figure 3.2 Updating level set functions

3.2 The extended finite element method

XFEM is a partition of unity finite element method (PUFEM). For more details on the PUFEM, the reader is referred to Melenk and Babuska (Melenk & Babuska, 1996; Babuska & Melenk, 1997). Detailed discussion about the XFEM theory can be found in (Bordas, 2003; Belytschko & Black, 1999; Moes, Gravouil, & Belytschko, 2002; Gravouil, Moes, & Belytschko, 2002; Dolbow, 1999). Here only the basic theory and implementation of XFEM as applied to LEFM-based crack growth analysis is presented.

3.2.1 Introduction to XFEM

Analyzing crack propagation involves computation of the $1/\sqrt{r}$ stress singularity observed in the crack-tip region. Due to this singularity, very high stress and displacement gradients are observed near the crack tip. Standard FEM requires a very refined mesh to adequately capture these gradients. The XFEM on the other hand, takes advantage of PUFEM, incorporates these singularities in the local approximation, and thus naturally reproduces effect of these singularities in the solution. Crack propagation analysis also involves treating the jump in displacement fields caused by the discontinuity across the crack surface. Again, this is observed in the local region surrounding the crack surface. While FEM requires the mesh to be aligned to the crack surfaces, XFEM enriches the nodes whose support is cut by the crack using Heaviside function and thus, accurately models the discontinuity. Since the discontinuity is modeled implicitly in the XFEM using Heaviside function, the mesh need not conform to the discontinuity.

3.2.2 XFEM displacement formulation

The X-FEM displacement approximation for a vector valued function $u(x)$: $\mathbb{R}^2 \rightarrow \mathbb{R}^2$ is given as

$$u^h(\boldsymbol{x},t) = \sum_{i\in I} u_i(t)\, N_i(\boldsymbol{x}) + \sum_{j\in J} b_j(t)\, N_j(\boldsymbol{x}) H\big(\psi(\boldsymbol{x},t)\big) + \sum_{k\in K} N_j(\boldsymbol{x}) \Big(\sum_{\ell=1}^{4} a_k^l(t) B_\ell(r,\theta)\Big) \tag{3.8}$$

where $N_i(\boldsymbol{x})$ is the shape function associated with the node i and t is a monotonically increasing time parameter. J is the set of all nodes whose support is bisected by the crack (shown by circled nodes in Figure 3.3). The set K contains all nodes of the elements containing the crack tip (shown by squared nodes in Figure 3.3). In Eq. (3.8), the first term is the regular finite element approximation; the second term represents the Heaviside step function (H) employed to model the discontinuity due to crack; and the last term incorporates the near-tip asymptotic displacement fields using the so called Branch functions.

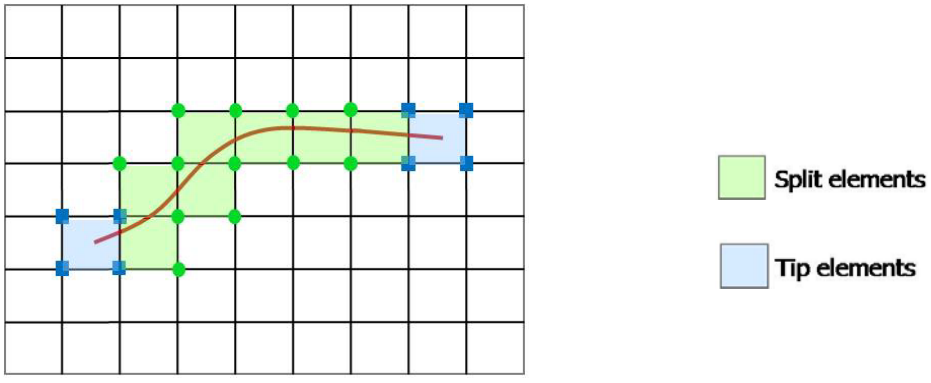

Figure 3.3 Enrichment in XFEM

3.2.3 Enrichment functions

The Heaviside function is defined as follows:

$$H(y) = \begin{cases} 1, & \text{for } y > 0 \\ -1, & \text{for } y < 0 \end{cases} \tag{3.9}$$

The branch functions are defined as:

$$B_l(r,\theta) = \left\{\sqrt{r}\,sin\frac{\theta}{2}, \sqrt{r}\,cos\frac{\theta}{2}, \sqrt{r}\,sin\frac{\theta}{2}\,sin\theta, \sqrt{r}\,cos\frac{\theta}{2}sin\theta\right\} \tag{3.10}$$

where (r, θ) are defined in a polar coordinate system at the crack tip and θ = 0 is tangent to the crack. Plots of branch functions are shown in Figure 3.4.

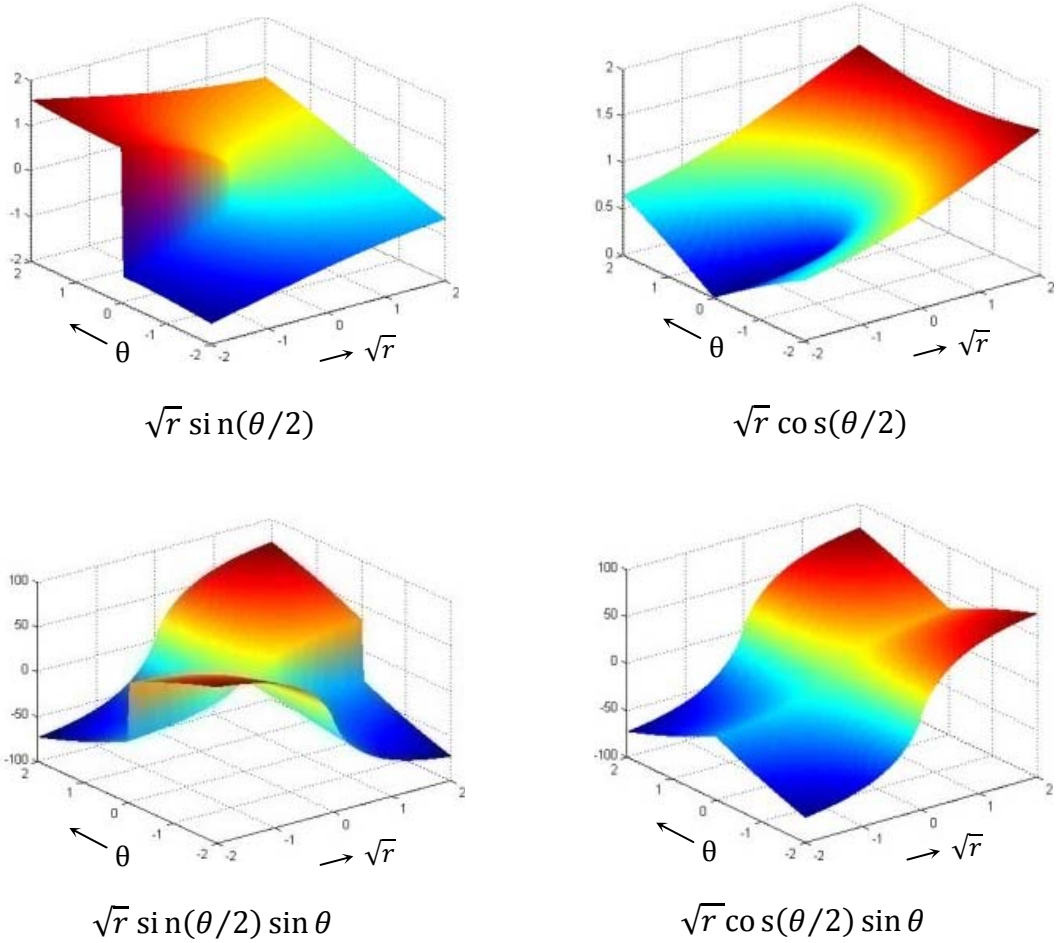

$\sqrt{r}\,\sin(\theta/2)$ $\sqrt{r}\,\cos(\theta/2)$

$\sqrt{r}\,\sin(\theta/2)\sin\theta$ $\sqrt{r}\,\cos(\theta/2)\sin\theta$

Figure 3.4 Branch functions

These functions span the near-tip asymptotic fields from Eq. (2.2) to Eq. (2.5), and the first branch function accounts for the discontinuity due to the crack (Belytschko, Moes, Usui, & Parimi, 2001). For each node enriched with Heaviside function, one fictitious node is added and for each node enriched with branch functions, four fictitious nodes are added. Thus, the total degrees of freedom for the enriched formulation are

$$ndof_{total} = (n_r + n_h + 4n_b) * 2 \tag{3.11}$$

where n_r is the number of regular nodes; n_s is the number of nodes with Heaviside function; and n_b is the number of nodes enriched with branch functions.

3.2.4 XFEM stiffness matrix construction

This section briefly discusses formulation of XFEM stiffness matrix. The XFEM formulation is very similar to the regular FEM formulation, except for the local enrichment. First, the shape function vectors are expanded to account for the enrichment functions.

$$\boldsymbol{N} = [\boldsymbol{N}_{FEM}, \quad \boldsymbol{N}_{ENRICHED}] \implies \boldsymbol{N} = [[N_1 \quad \dots \quad N_4], \quad [\psi_1 N_1 \quad \dots \quad \psi_4 N_4]] \tag{3.12}$$

where ψ_{i} are enrichment functions (either Heaviside or Branch functions). The 'B' matrix, which consists of shape function derivatives, is constructed as follows:

$$\boldsymbol{B} = [\boldsymbol{B}_{FEM}, \quad \boldsymbol{B}_{ENRICHED}]$$

$$\boldsymbol{B} = \begin{bmatrix} & (\psi_1 N_1)_{,x} & 0 & \dots & 0 \\ \boldsymbol{B}_{FEM} & 0 & (\psi_1 N_1)_{,y} & \dots & (\psi_4 N_4)_{,y} \\ & (\psi_1 N_1)_{,y} & (\psi_1 N_1)_{,x} & \dots & (\psi_4 N_4)_{,x} \end{bmatrix} \tag{3.13}$$

Derivatives of the Heaviside function is the well-known Dirac-Delta function (δ). However, if the crack surfaces are assumed to be traction free, then derivatives of

Heaviside function can be omitted (Rabczuk & Wall, 2006-2007). Therefore the derivative of the Heaviside function is:

$$\frac{\partial(HN_i)}{\partial x} = \frac{\partial N_i}{\partial x} \cdot H \tag{3.14}$$

Since the branch functions are expressed in crack-tip coordinate system, their derivatives are calculated using chain rule as follows:

$$\frac{\partial Br_i}{\partial x} = \frac{\partial Br_i}{\partial r} \cdot \frac{\partial r}{\partial x} + \frac{\partial Br_i}{\partial \theta} \cdot \frac{\partial \theta}{\partial x}; \quad \text{and} \quad \frac{\partial Br_i}{\partial y} = \frac{\partial Br_i}{\partial r} \cdot \frac{\partial r}{\partial y} + \frac{\partial Br_i}{\partial \theta} \cdot \frac{\partial \theta}{\partial y} \tag{3.15}$$

The enriched global stiffness matrix is constructed using the following relation

$$\boldsymbol{K} = \int_{\Omega} \boldsymbol{B}^T \boldsymbol{C} \boldsymbol{B} \; d\Omega \tag{3.16}$$

where $\boldsymbol{C}$ is the constitutive matrix. The integration is carried out using Gauss Quadrature method, more details on which follow. The equilibrium equation in discretized form is,

$$\begin{bmatrix} \boldsymbol{K_{uu}} & \boldsymbol{K_{ua}} & \boldsymbol{K_{ub}} \\ \boldsymbol{K_{ua}} & \boldsymbol{K_{aa}} & \boldsymbol{K_{ab}} \\ \boldsymbol{K_{ub}} & \boldsymbol{K_{ab}} & \boldsymbol{K_{bb}} \end{bmatrix} \begin{Bmatrix} \boldsymbol{u} \\ \boldsymbol{a} \\ \boldsymbol{b} \end{Bmatrix} = \begin{Bmatrix} \boldsymbol{f_u} \\ \boldsymbol{f_a} \\ \boldsymbol{f_b} \end{Bmatrix} \tag{3.17}$$

where $\boldsymbol{K_{uu}}$, $\boldsymbol{K_{aa}}$, and $\boldsymbol{K_{bb}}$ are contributions from regular nodes, nodes enriched with Heaviside functions, and nodes enriched with branch functions, respectively; $\boldsymbol{u}$, $\boldsymbol{a}$, and $\boldsymbol{b}$ are nodal displacements corresponding to the regular and extra degrees of freedom, respectively; and $\boldsymbol{f}$ is the external force vector.

3.2.5 Discontinuous Gauss Quadrature

Regular Gauss integration does not permit discontinuity in displacement and stress fields that are observed across the crack faces. To circumvent this problem, the discontinuous elements are divided into sub-triangles such that the triangle edges are

coincident with the crack geometry. This allows the fields to be continuous over each sub-region and the integration can be carried out. To capture the high gradients in the near-tip elements, higher order gauss integration is used. Figure 3.5 shows the subdivision of discontinuous elements into triangles. It must be emphasized that this is not re-meshing; merely a way to handle integration in discontinuous elements. A thorough discussion on this was presented by Sukumar & Prevost (2003).

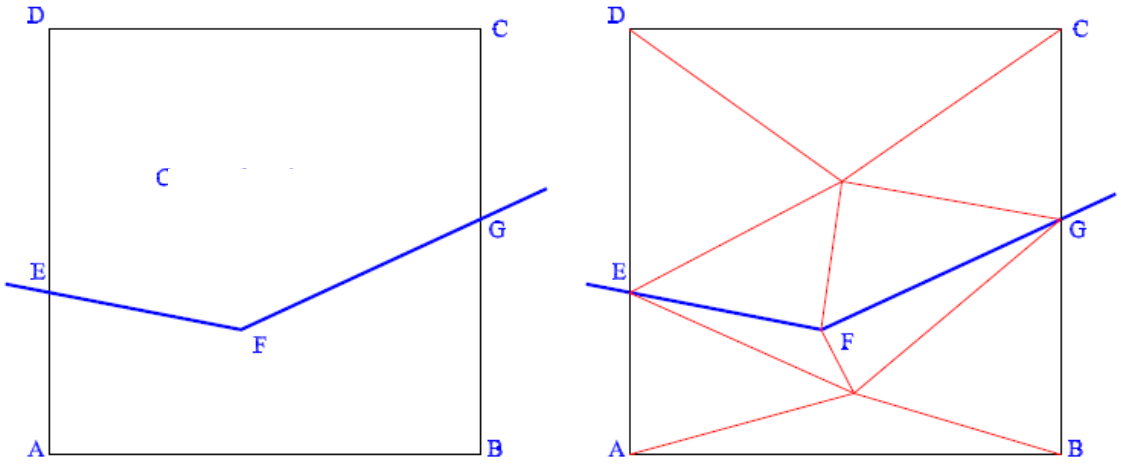

Figure 3.5 Division of elements into sub-triangles for Gauss integration

Note that there are three types of elements: crack-tip elements, elements completely cut by crack, and regular elements. Different quadrature order is used for each kind of element (see Figure 3.6). Gauss integration order of 7 was used for each sub-triangle of the crack-tip element, an order of 3 was used for the elements cut by crack, and for regular elements, an order of 2 was used. A report published by David Noel (2007-2008) presents a lucid explanation of the effect of selecting a particular order of

integration for particular type of element, and the reader is referred to the same for more details.

3.2.6 Interaction energy integral evaluation

Remember that the domain form of the interaction integral approach lends itself particularly well for implementation using finite element methods. Elements surrounding the crack tip form the domain for interaction integral evaluation. Even though the interaction integral is theoretically path independent, for numerical evaluation, the domain must be carefully selected. If the radius is too small, the crack-tip element would contribute towards evaluation of field variables, and the computational accuracy will suffer. On the other hand, if the radius is too large, the effect of crack-tip singularities may not be captured. Nguyen (2005) performed a study of effect of domain radius on accuracy of stress intensity factors. As suggested by Nguyen, all elements intersected by a circle of radius equal to 3 to 5 times the area of the crack-tip element should be selected for evaluation of interaction energy integral.

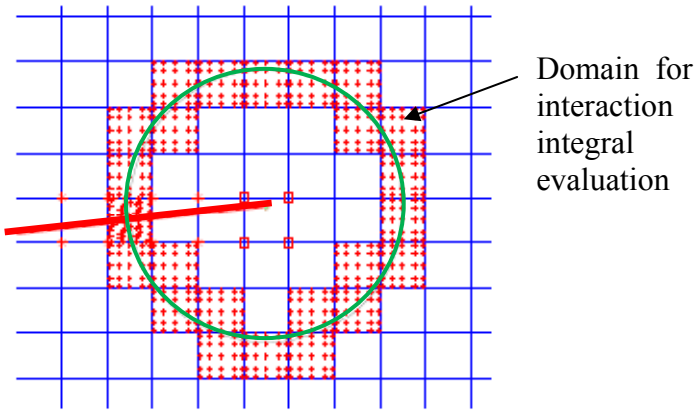

Figure 3.6 Domain for interaction integral evaluation and Gauss integration points in the corresponding elements

3.3 Combination of XFEM and LSM

XFEM and LSM work together naturally for crack growth modeling. Level sets contain all the necessary information for modeling crack, and allow crack propagation over a fixed mesh. Further, they facilitate selection of nodes for enrichment. To determine whether a node lies above or below the crack, one simply needs to retrieve sign of ψ at that point. If the crack cuts through an element, then $\phi \leq 0$ and $\psi_{min}\psi_{max} \leq 0$, where ψ_{min} and ψ_{max} are the minimum and maximum values of ψ at the nodes of this element. Nodes of this element are enriched with Heaviside function. If crack tip lies inside an element, then $\phi_{min}\phi_{max} \leq 0$ and $\psi_{min}\psi_{max} \leq 0$, and nodes of that element are enriched with branch functions shown in Eq. (3.10).

Also note that the level sets ϕ and ψ are orthogonal to each other form a natural coordinate system whose origin lies at the crack tip. The direction of the local X-axis can be obtained by computing $\nabla\phi$. Local Y-axis is determined by computing $\hat{e}_z \times \nabla\phi$, where $\hat{e}_z = (0,0,1)$. Parameters required for computing the branch functions are defined in local crack-tip coordinate system, and can be directly computed using level set functions as follows:

$$r = \sqrt{\psi^2(\boldsymbol{x},t) + \phi^2(\boldsymbol{x},t)}\,; \quad \text{and} \quad \theta = tan^{-1}\left(\frac{\psi(\boldsymbol{x},t)}{\phi(\boldsymbol{x},t)}\right) \tag{3.18}$$

XFEM computes the required information for crack growth $(\theta_c, \Delta a)$, which is then used to update level sets, and hence, crack-tip position.

The algorithm shown in Figure 3.7 delineates the procedure for crack propagation analysis using XFEM and LSM. First, level sets are computed for the initial crack and the nodes to be enriched are determined. The equilibrium equation with extra degrees of

freedom is solved according to Eq. (3.17) and nodal displacements are obtained. From this information, SIFs and θ_c are obtained using Eq. (2.29), (2.30) and Eq. (2.9), respectively. The level sets are updated using this information and new crack segment is added. The process is repeated until specified termination criterion is reached.

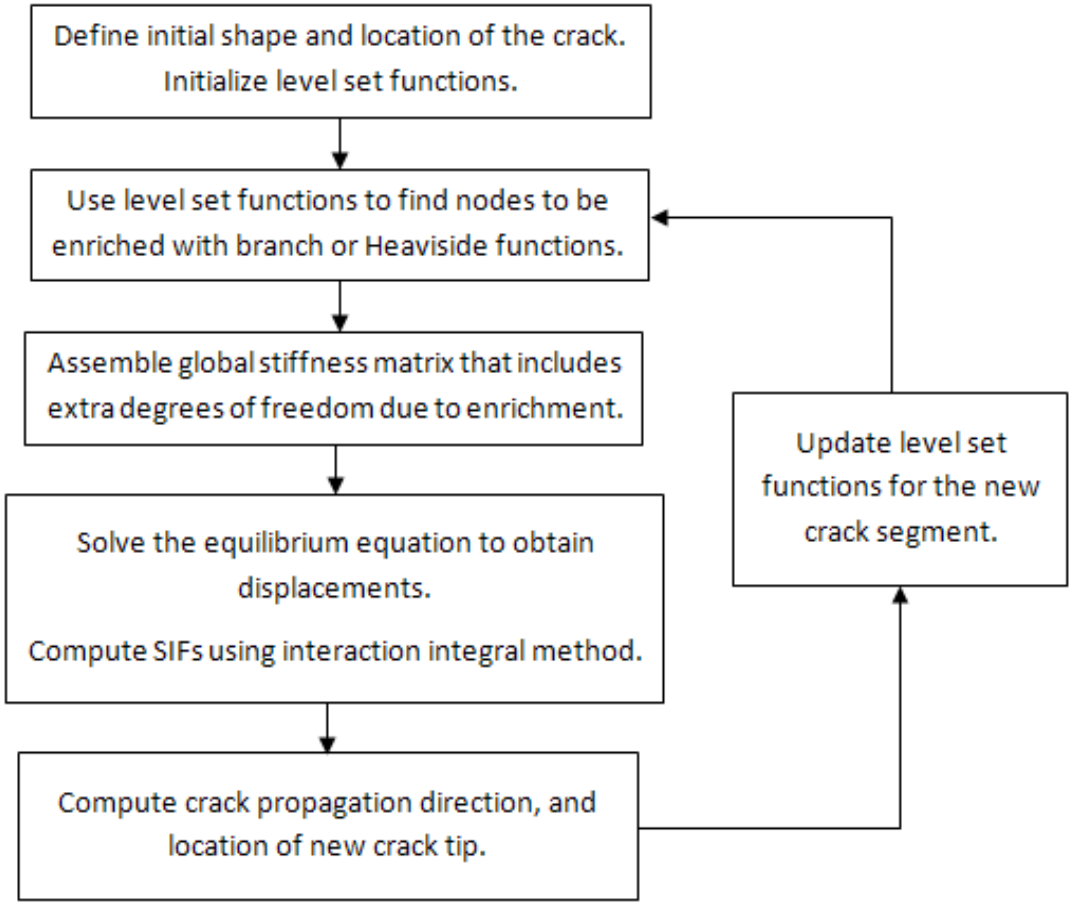

Figure 3.7 Algorithm for crack propagation using XFEM and LSM

3.4 Example 1: Rectangular plate under shear load

Consider a rectangular plate of width $w = 7\,in$ and height of $h = 16\,in$ and an edge crack of $a = 3.5\,in$ as shown in Figure 3.8. The bottom face of the plate is fixed and a shear load of $\tau^{\infty} = 1\,psi$ acts on the top. The Young's modulus is $E = 30 \times 10^6\,psi$ and Poisson's ratio is $\nu = 0.25$. Fracture toughness for this material is 45.80 $ksi\sqrt{in}$. A 27×55 mesh is used that constitutes about 3700 degrees of freedom, including the extra degrees of freedom incurred due to enriched nodes. Crack growth simulation is performed for this problem using the XFEM-LSM code, in which an initial crack and a pre-determined crack growth increment (Δa) are prescribed. Fracture toughness is specified as termination criterion. The guidelines for selecting a value for Δa are discussed by Fleming (1997).

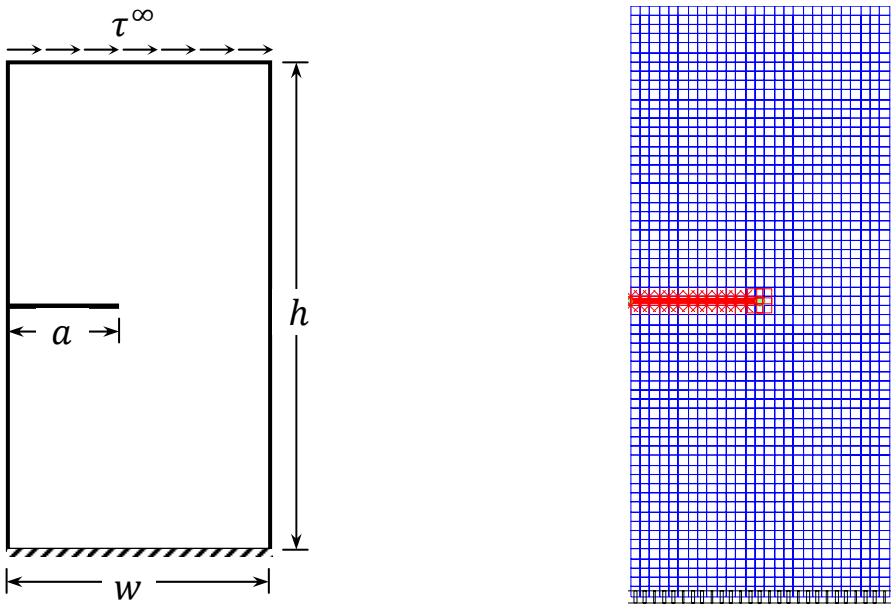

(a) A rectangular plate under shear load (b) XFEM mesh with enriched nodes

Figure 3.8 Crack propagation analysis example: A rectangular plate under shear

Figure 3.9 shows Y-stress plot for the plate after three crack propagation cycles. The high-stress region near crack tip can be observed. A closer view of crack propagation path is shown in Figure 3.10 and the crack growth analysis results are summarized in Table 3.1. The first row in Table 3.1 corresponds to the initial crack. The correlation between crack inclination angle and the SIFs is evident from the results. The crack starts growing at an inclined angle since both mode I and mode II SIFs are significant. When mode II SIF decreases rapidly, the crack keeps growing in a straight direction (relative to the previous crack segment). It is observed that mode I SIF increases steadily, but mode II SIF remains close to zero. The analysis stopped after 3 crack growth cycles when the equivalent SIF exceeded fracture toughness of the material.

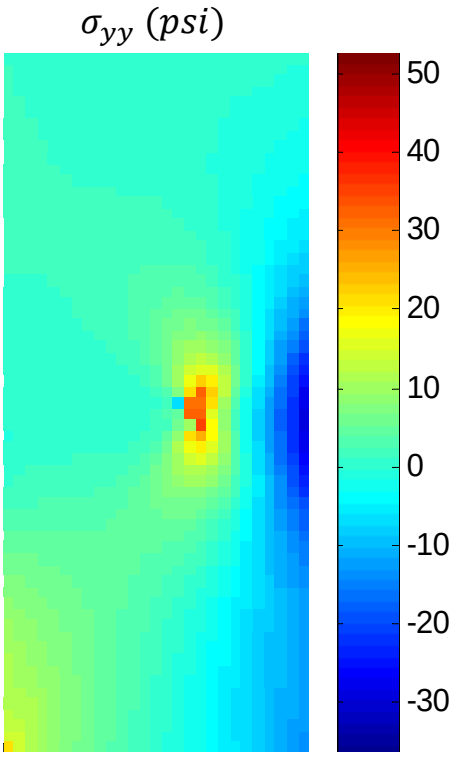

Figure 3.9 Y-stress plot at failure

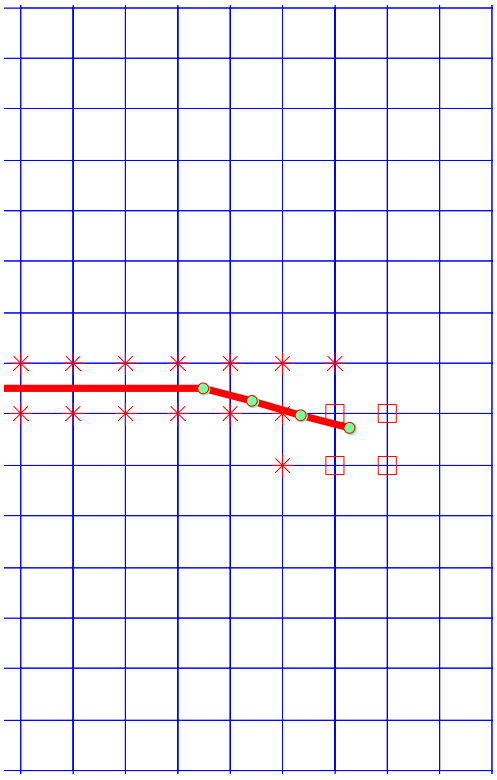

Figure 3.10 Crack propagation path

Table 3.1 Crack propagation analysis results for the rectangular plate under shear load

Cycles	K_I $(ksi\sqrt{in})$	K_{II} $(ksi\sqrt{in})$	θ_c (Deg)	Crack Tip Coordinates
0	33.293	4.506	-14.89	(3.50,8.00)
1	37.994	-0.003	0.01	(3.74,7.94)
2	43.608	0.009	-0.25	(3.98,7.87)
3	49.338	-0.037	0.09	(4.22,7.81)

The SIF results for the initial crack configuration are compared to the results obtained by Chen *et al.* (2001). Note that even though the mesh near crack-tip region is not very refined, the SIF values for initial design compare very well with those obtained by Chen *et al.* as shown in Table 3.2. Hence, it can be deduced that the XFEM-LSM code is capable of handling 2-D crack propagation analysis.

Table 3.2 Comparison of SIF results against test cases

	Reference	Proposed method	% Difference
K_I $(psi\sqrt{in})$	34.13	33.29	2.46
K_I $(psi\sqrt{in})$	4.54	4.51	0.66

3.5 Example 2: Engine connecting rod

Consider an engine connecting rod (Hwang, Choi, & Chang, 1997) shown in Figure 3.11. Material properties for the rod are as follows: Young's modulus $E = 210\ GPa$ and Poisson's ratio is $\nu = 0.30$. The Paris constants are: $C = 5.6 \times 10^{-12}\ mm/cycle$ and $m = 3.5$, and fracture toughness is $K_c = 100\ MPa\sqrt{mm}$.

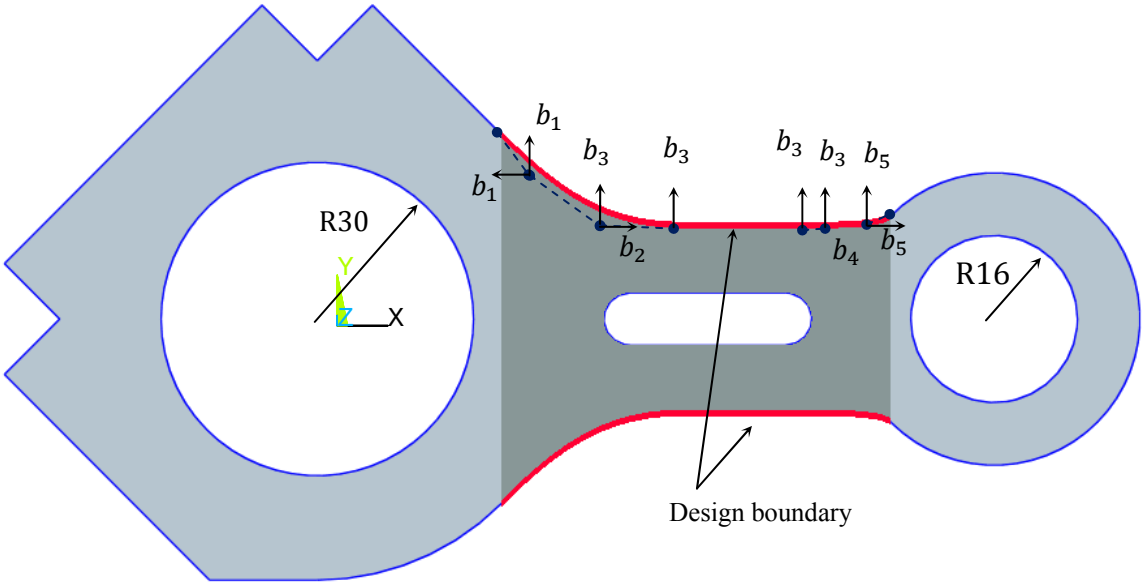

Figure 3.11 Engine Connecting Rod

The design boundary, shown by thick red lines, consists of two cubic Bezier curves at each end and a horizontal line in the middle. Upper and lower design boundaries are symmetric with respect to the centerline. Vertices of the control polygons of these Bezier curves are selected as design variables. Parametric equations of the design boundary are developed. There are total five design variables. Note that the control points corresponding to b_1 and b_5 are constrained to move at an angle of 45° to maintain tangency with the adjacent segments. Design variable b_3 controls movement of four control points as shown in order to keep the edge straight and horizontal. The shaded area represents the domain affected by design variables. The initial design variable values and their upper and lower bounds are summarized in Table 3.3.

Table 3.3 Design variables for the engine connecting rod

Variable	Lower bound	Initial value	Upper bound
b_1 (mm)	15.00	25.00	30.00
b_2 (mm)	40.00	55.00	65.00
b_3 (mm)	7.00	18.00	21.00
b_4 (mm)	90.00	100.00	115.00
b_5 (mm)	12.00	18.50	19.50

The load acting on the connecting rod in terms of the rotation angle θ is given by

$$T_F = \begin{cases} 43.794\theta^2 + 30.19 \quad \text{at left inner circle} \ \left(\frac{-40}{180}\pi \le \theta \le \frac{40}{180}\pi\right) \\ 9.54\theta^2 - 42.97 \quad \text{at right inner circle} \ \left(\frac{140}{180}\pi \le \theta \le \frac{220}{180}\pi\right) \end{cases} \tag{3.19}$$

Initially, a mesh with about 6000 DOFs was created using ANSYS. Figure 3.12 shows the finite element model of the connecting rod. Average element length (ℓ_e) in the crack region for this mesh is 1.9 mm. This, of course, varies from element to element and is only given here to give a rough idea about mesh size as compared to the crack growth increment. Boundary conditions were applied as suggested by Hwang *et al.* (1997).

The maximum principal stress distribution in the connecting rod is shown in Figure 3.13. Although the maximum stress appears to be at the fixed node on the left side, it is merely an artificial stress concentration due to displacement constraints. The real maximum stress of $\sigma_{max} = 124$ MPa occurs on the left semicircular edge of the slot. An initial crack of $a = 7\ mm$ (an arbitrary choice) is introduced in this location and crack propagation analysis is conducted with $\Delta a = 1.5\ mm$. Figure 3.14 shows the crack propagation path until failure, i.e. until K_{eq} exceeds the fracture toughness of the material.

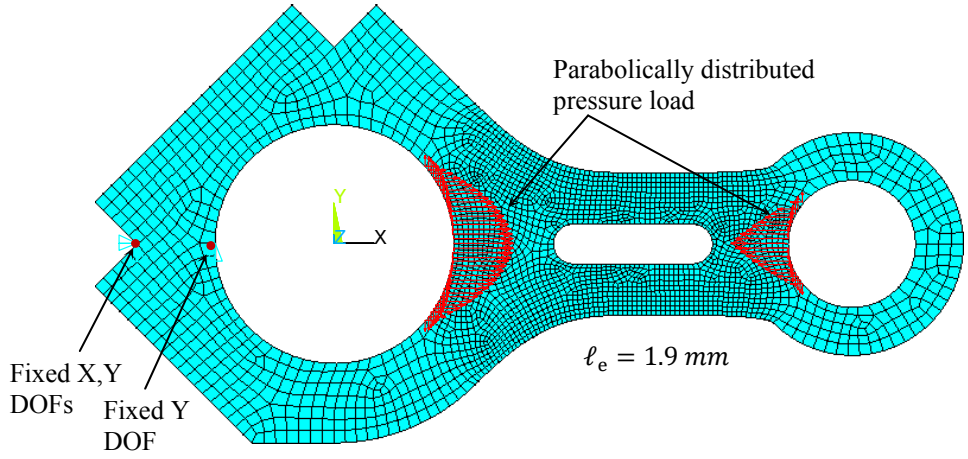

Figure 3.12 Finite element model of the connecting rod

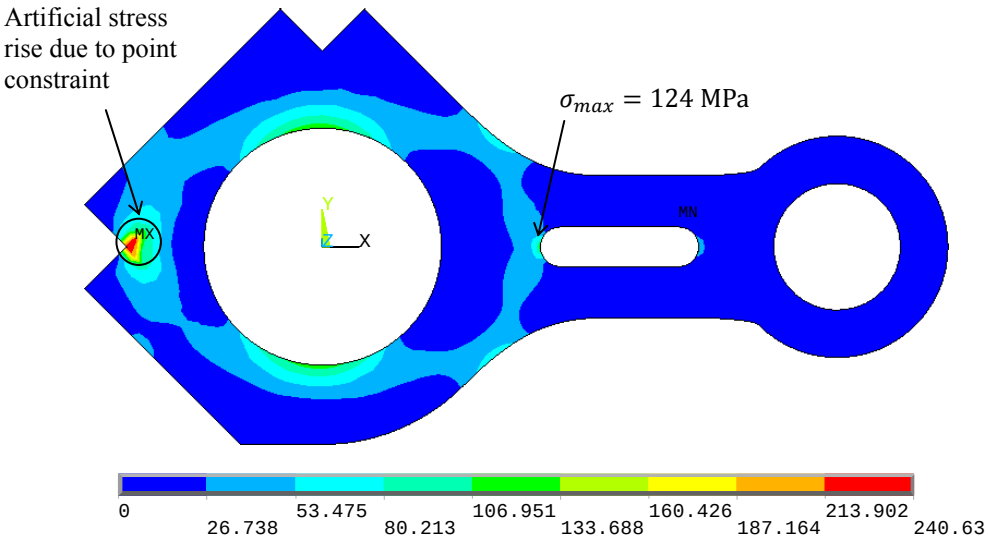

Figure 3.13 Maximum principal stress distribution for connecting rod

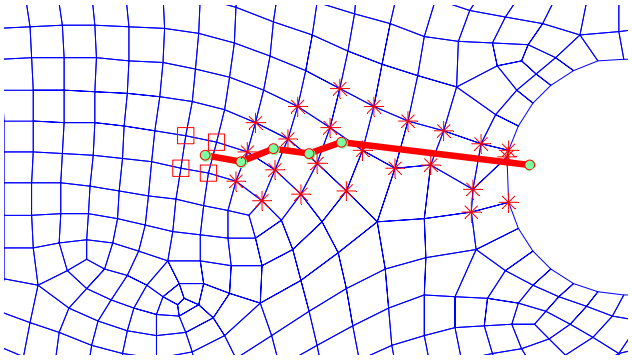

Figure 3.14 Crack propagation path

For mixed-mode cases, generally the crack propagation path is curvilinear. In this case however, the path appears to be zigzag due to alternating positive and negative sign of θ_c. Large crack growth increment Δa is suspected to be the main reason behind these oscillations. Based on initial crack size, the algorithm predicts certain crack growth direction, but due to fixed Δa, crack overshoots in that direction. The algorithm tries to compensate for this error by changing angle in the next cycle, but it again overshoots due to the fixed value of Δa. Thus, the crack growth increment must be reduced to minimize these oscillations.

From analysis standpoint, XFEM-LSM does allow crack to propagate within an element. However if Δa is quite small as compared to average element size, the same set of elements will be used for computation of interaction integral for multiple successive crack growth cycles, and computation of fracture parameters may not be reliable. Thus, Δa and mesh size are related and do have an impact on accuracy of analysis results. This relationship also plays an important role in downstream design studies. If large value of Δa is selected, it may not accurately predict crack path and service life, leading to erroneous optimum design. On the other hand, very small value of Δa will require very fine mesh, thereby greatly increasing computational burden. Hence a detailed study was undertaken to examine effect of mesh refinement and crack growth increments on SIFs and crack propagation path. Based on this study, appropriate level of mesh refinement and crack growth increment were determined for design sensitivity analysis and optimization studies.

3.6 Effect of mesh refinement and crack growth increment

The crack growth analysis for the initial mesh (henceforth called Mesh 1) revealed the crack propagation path. Taking advantage of this, only elements in this region were refined to create two additional finite element models. Mesh 2 (shown in Figure 3.15) is the intermediate mesh with 8,554 DOFs and Mesh 3 (see Figure 3.16) is the finest mesh with 25,186 DOFs. Average element length (ℓ_e) near crack region for Mesh 2 is 0.65 mm and that for Mesh 3 is 0.22 mm.

For each of these meshes, twelve different Δa values ranging from 0.1 mm to 1.2 mm were used and crack growth simulations were carried out. Note that the algorithm is set-up not to allow multiple crack growth increments within an element to avoid erroneous calculation of SIFs. Hence, for coarse mesh (Mesh 1), Δa values smaller than 0.9 mm could not be used. Similarly, for intermediate mesh (Mesh 2), values of Δa smaller than 0.3 mm could not be used. These values roughly correspond to $0.5(\ell_e)$.

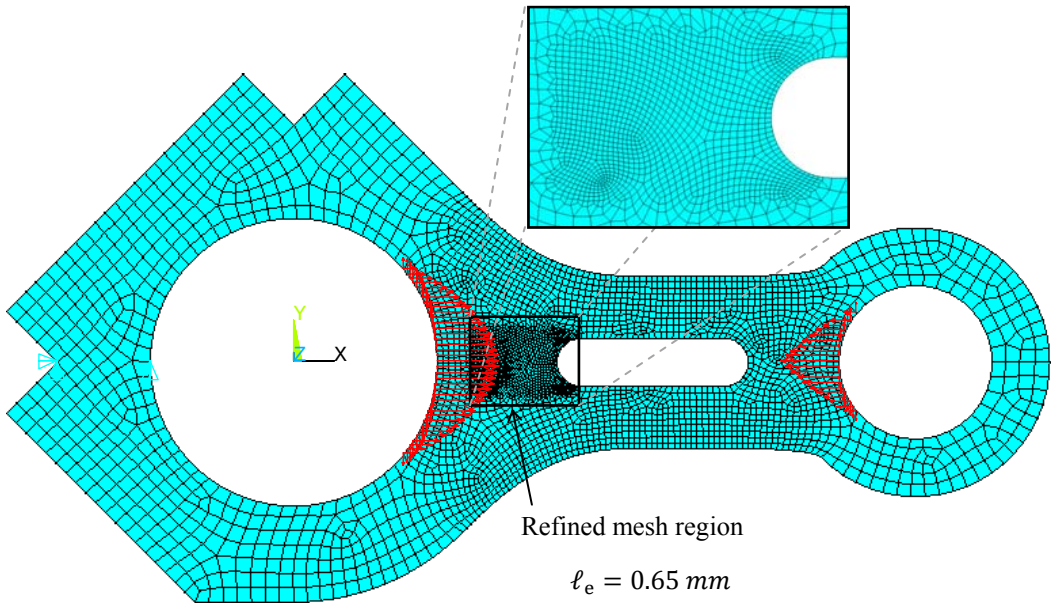

Figure 3.15 Finite element model of the connecting rod (Mesh 2: Intermediate mesh)

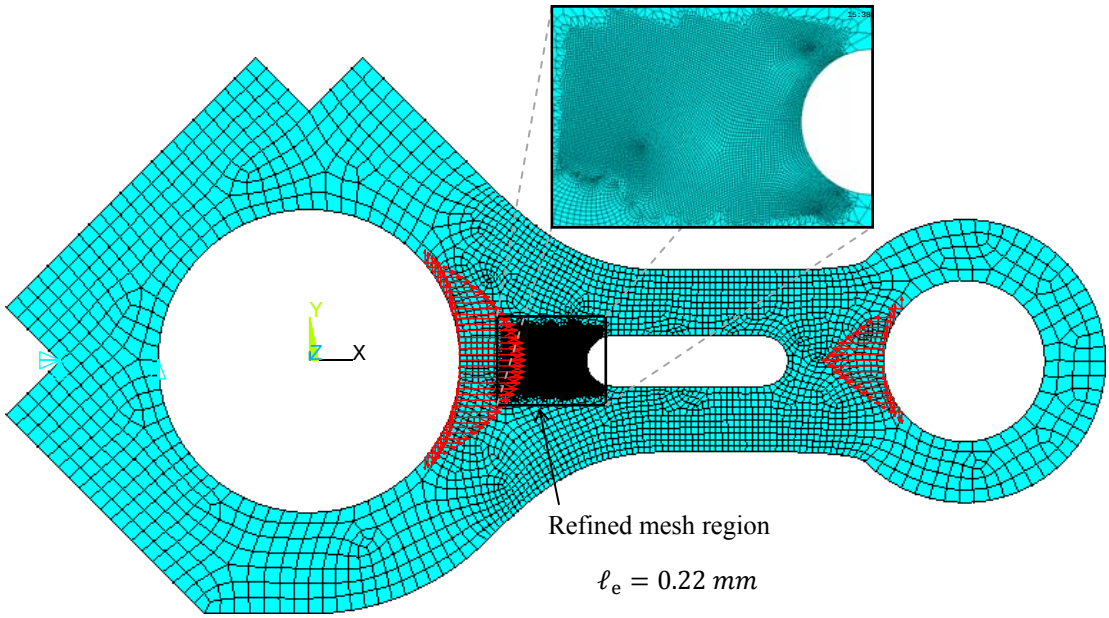

Figure 3.16 Finite element model of the connecting rod (Mesh 3: Fine mesh)

3.6.1 Δa study results for Mesh 1

Figure 3.17 shows crack propagation path for different values of Δa for the coarse mesh. The scale on both axes is selected to be different to illustrate the path more clearly. Table 3.4 shows equivalent stress intensity factor (K_{eq}), and Table 3.5 lists crack propagation angle (θ_c) and service life (N) results for this study. As seen from Figure 3.17, the crack path is zigzag for all values of Δa. Explanation for this can be found in Table 3.5, which shows that the sign for θ_c switches from cycle to cycle. Thus, for Mesh 1, reducing Δa from 1.5 mm to 0.9 mm does not markedly affect the zigzag nature of the path. From Table 3.4, it can be observed that for certain consecutive crack growth cycles (for example, cycle 2 and 3 for $\Delta a = 0.9\ mm$), the SIF value is quite close. This occurs when a crack segment lies completely within an element.

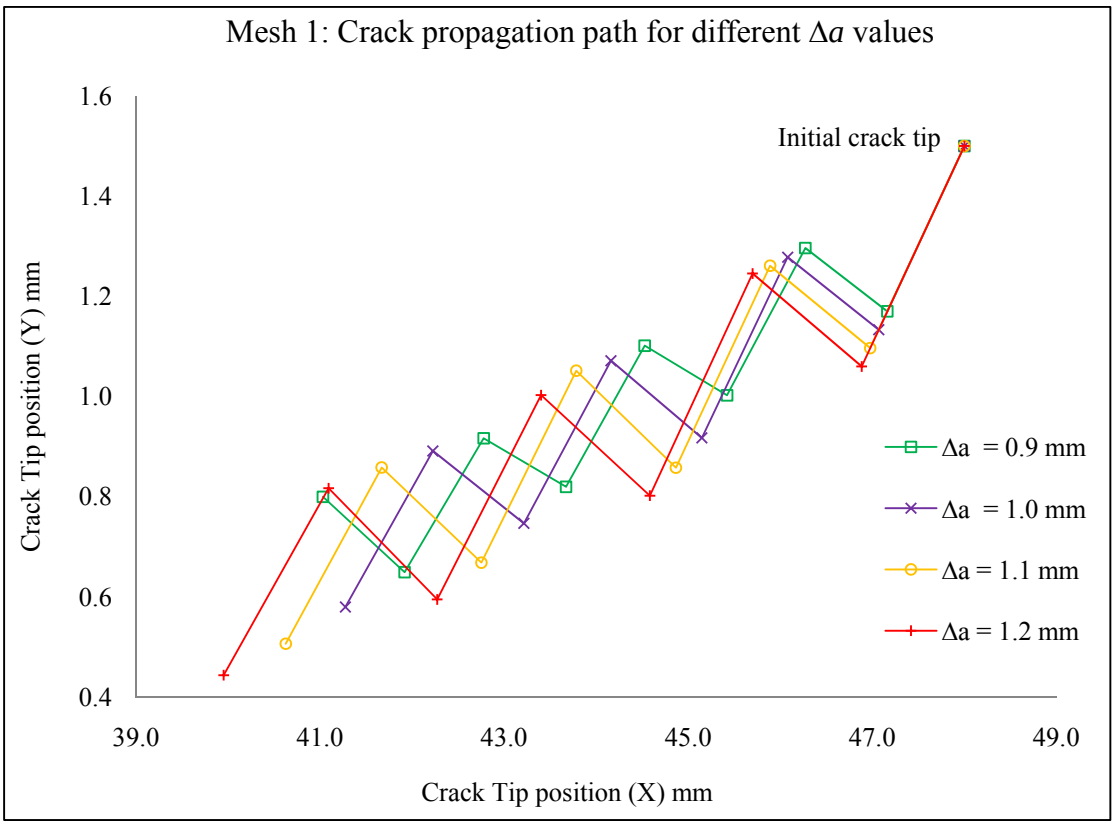

Figure 3.17 Crack propagation path for different values of Δa for Mesh 1

Table 3.4 Equivalent stress intensity factor results for Mesh 1

Cycle No.	Equivalent stress intensity factor K_{eq} $(MPa\sqrt{mm})$			
	$\Delta a = 0.9\ mm$	$\Delta a = 1.0\ mm$	$\Delta a = 1.1\ mm$	$\Delta a = 1.2\ mm$
1	81.10	81.10	81.10	81.10
2	83.37	83.57	83.77	83.99
3	83.03	87.41	87.63	88.00
4	89.81	89.64	89.94	90.39
5	90.68	90.65	96.06	96.94
6	96.44	97.15	95.94	99.24
7	97.13	100.42	99.39	103.25
8	100.71		103.28	

Table 3.5 Crack propagation angle and service life results for Mesh 1

Cycle	Crack propagation angle θ_c (Degrees)				Service Life N (cycles)			
	Δa				Δa			
No.	0.9 mm	1.0 mm	1.1 mm	1.2 mm	0.9 mm	1.0 mm	1.1 mm	1.2 mm
1	28.64	28.64	28.64	28.64	33460	37177	40895	44613
2	-29.59	-29.84	-30.11	-30.41	30377	33473	36506	39461
3	27.14	29.47	30.09	30.58	30807	28594	31182	33519
4	-25.38	-30.01	-31.63	-31.31	23414	26188	28474	30521
5	24.55	27.81	30.52	29.49	22633	25176	22614	23893
6	-24.41	-27.25	-30.32	-30.53	18248	19760	22712	22011
7	23.46	26.44	28.59	28.78	17798	17598	20065	
8	-26.89		-29.55		15678			
Total service life:					192415	187967	202448	194018

While the total service life for $\Delta a = 0.9\,mm$ and $1.0\,mm$ is quite close, that for other two cases is about 10% higher. This increase in life is due to the following factors: (i) the crack overshoots during the last cycle, and (ii) larger Δa naturally corresponds to increased service life.

3.6.2 Δa study results for Mesh 2

Figure 3.18 shows crack propagation path for different values of Δa for the intermediate mesh. Table 3.6, Table 3.7, and Table 3.8 show results for K_{eq}, θ_c, and N, respectively. It can be observed that with decreasing values of Δa, the oscillations decrease and for values of Δa smaller than $0.6\,mm$, the crack path is quite smooth for the last few cycles. It should also be noticed that crack paths corresponding to Δa values are spaced quite closely. For example, for a fixed value of X, the position of crack tip for different values of Δa differs only by about $0.1\,mm$.

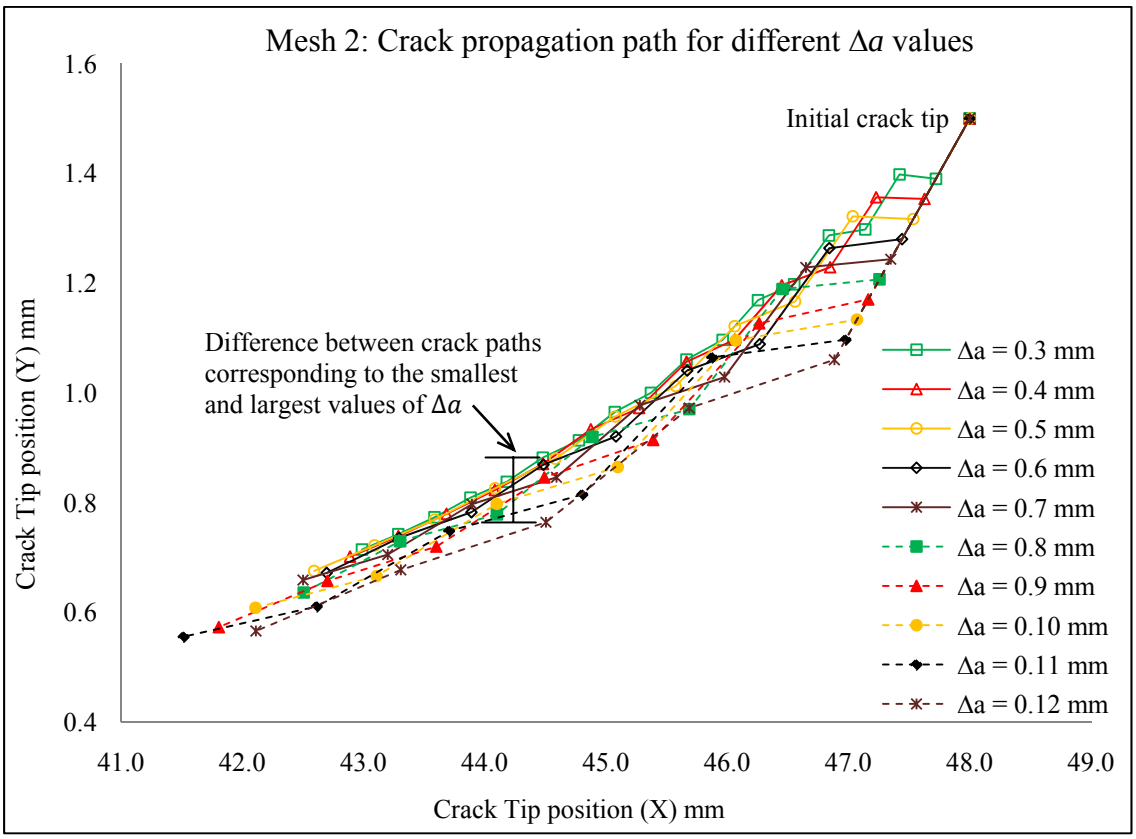

Figure 3.18 Crack propagation path for different values of Δa for Mesh 2

The service life results shown in Table 3.8 differ by about 8% depending upon Δa. As seen from Table 3.6, for $\Delta a = 0.3\,mm$, the difference between SIF values for some consecutive cycles (for example, cycles 3 and 4, 6 and 7, 8 and 9) is very small. In these cycles, the crack propagates within the same element. This corroborates earlier claim that from numerical implementation perspective, it is not desirable to choose Δa value that is much smaller than ℓ_e. Also, for same value of Δa, θ_c decreases in magnitude as crack length increases. This is to be expected since the compressive load in X-direction is analogous to applying tensile load in Y-direction (due to Poisson effect as well as due to Hoop stress effect). This, in effect, is similar to Mode I loading and hence, the crack eventually becomes straight.

Table 3.6 Equivalent stress intensity factor results for Mesh 2

Cycle	Equivalent stress intensity factor K_{eq} $\left(MPa\sqrt{mm}\right)$									
No.	$\Delta a = 0.3\ mm$	$0.4\ mm$	$0.5\ mm$	$0.6\ mm$	$0.7\ mm$	$0.8\ mm$	$0.9\ mm$	$1.0\ mm$	$1.1\ mm$	$1.2\ mm$
1	81.52	81.52	81.52	81.52	81.52	81.52	81.52	81.52	81.52	81.52
2	81.35	82.44	82.77	83.38	83.69	84.01	84.97	85.30	85.54	86.34
3	84.67	85.99	86.44	87.58	88.40	89.03	89.84	90.45	91.10	92.07
4	84.95	86.81	88.35	89.57	90.49	91.54	92.81	93.82	94.83	96.15
5	87.49	89.29	90.98	91.85	93.52	94.96	96.34	97.57	98.82	100.20
6	88.40	90.67	92.45	94.08	95.91	97.47	99.25	100.77	102.25	
7	88.91	90.94	94.29	96.22	98.34	100.15	102.06			
8	91.15	93.48	96.14	98.36	100.51					
9	91.35	95.15	97.77	100.24						
10	93.35	95.20	99.41							
11	93.40	97.77	100.99							
12	95.44	99.05								
13	95.42	100.31								
14	97.47									
15	98.41									
16	98.43									
17	100.33									

Table 3.7 Crack propagation angle results for Mesh 2

Cycle No.	Crack propagation angle θ_c (Degrees)									
	$\Delta a = 0.3\ mm$	$0.4\ mm$	$0.5\ mm$	$0.6\ mm$	$0.7\ mm$	$0.8\ mm$	$0.9\ mm$	$1.0\ mm$	$1.1\ mm$	$1.2\ mm$
1	28.62	28.62	28.62	28.62	28.62	28.62	28.62	28.62	28.62	28.62
2	-23.01	-21.92	-22.06	-19.92	-20.27	-20.23	-18.71	-19.33	-19.81	-17.29
3	21.03	19.00	18.65	15.39	15.36	14.62	10.86	11.19	11.45	5.79
4	-17.41	-13.86	-12.92	-12.37	-12.38	-12.25	-9.28	-9.50	-9.68	-5.84
5	15.15	9.59	7.45	6.98	6.60	6.53	3.68	3.70	3.74	1.18
6	-11.71	-8.51	-6.25	-6.64	-6.80	-6.65	-4.06	-4.24	-4.30	
7	8.42	6.39	2.48	3.37	3.54	3.20	1.39			
8	-7.10	-6.61	-2.65	-3.80	-3.75					
9	4.79	3.51	0.35	1.60						
10	-4.94	-2.26	-1.13							
11	3.18	-0.59	-0.07							
12	-3.87	-0.39								
13	2.40	-0.52								
14	-2.89									
15	1.29									
16	-0.90									
17	-0.59									

Table 3.8 Service life results for Mesh 2

Cycle	Service life N (Cycles)									
No.	$\Delta a = 0.3\ mm$	$0.4\ mm$	$0.5\ mm$	$0.6\ mm$	$0.7\ mm$	$0.8\ mm$	$0.9\ mm$	$1.0\ mm$	$1.1\ mm$	$1.2\ mm$
1	10951	14601	18252	21902	25553	29203	32853	36504	40154	43804
2	11035	14041	17306	20239	23313	26291	28417	31146	33937	35827
3	9593	12117	14869	17044	19245	21455	23383	25372	27218	28618
4	9483	11719	13774	15755	17732	19464	20869	22324	23657	24585
5	8553	10617	12430	14425	15806	17123	18309	19463		
6	8249	10065	11750	13267	14468	15626				
7	8083	9959	10970	12260	13257					
8	7411	9044	10246	11353						
9	7352	8500	9663							
10	6815	8485	9114							
11	6804	7729								
12	6309	7385								
13	6313									
14	5861									
15	5666									
16	5661									
Total:	124137	124262	128375	126245	129373	129161	123831	134809	124966	132834

3.6.3 study results for Mesh 3

Figure 3.19 shows crack propagation path for different values of for the fine mesh. Table 3.9, Table 3.10, and Table 3.11 show results for , , and , respectively. It can be observed that for all values of , sign for is consistent except for first few crack growth cycles. Therefore, the crack propagation path appears quite smooth. It should also be noticed that crack paths for different values are spaced quite closely—for a fixed value of X, the position of crack tip for different values of differs only by less than . The service life results shown in Table 3.11 differ by about by 8% depending upon .

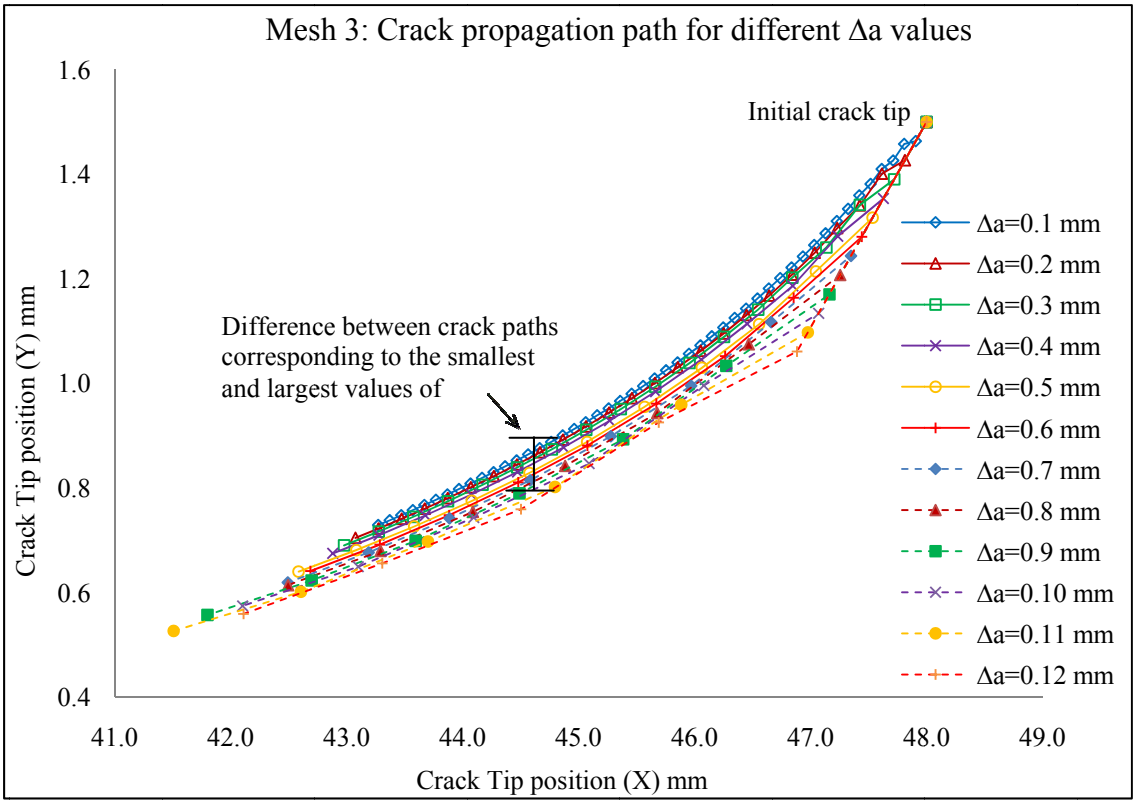

Figure 3.19 Crack propagation path for different values of for Mesh 3

Table 3.9 Equivalent stress intensity factor results for Mesh 3

Cycle No.	Equivalent stress intensity factor K_{eq} $\left(MPa\sqrt{mm}\right)$													
	$\Delta a = 0.1\ mm$			$0.2\ mm$	$0.3\ mm$	$0.4\ mm$	$0.5\ mm$	$0.6\ mm$	$0.7\ mm$	$0.8\ mm$	$0.9\ mm$	$1.0\ mm$	$1.1\ mm$	$1.2\ mm$
1	81.69	25	92.55	81.69	81.69	81.69	81.69	81.69	81.69	81.69	81.65	81.69	81.69	81.69
2	81.40	26	92.56	83.41	84.29	85.15	85.88	86.07	86.26	86.38	86.48	86.65	86.84	87.07
3	84.36	27	93.24	85.99	86.71	87.28	87.83	88.42	89.01	89.63	90.24	90.92	91.62	92.23
4	84.27	28	93.24	86.70	87.56	88.44	89.40	90.35	91.27	92.26	93.28	94.27	95.34	96.25
5	85.96	29	93.84	87.43	88.52	89.75	91.02	92.36	93.71	95.03	96.38	97.73	99.03	100.31
6	86.25	30	94.16	87.97	89.43	91.05	92.74	94.49	96.10	97.75	99.37	101.00	102.44	
7	86.89	31	94.51	88.54	90.42	92.42	94.44	96.51	98.46	100.38	102.18			
8	87.14	32	94.85	89.17	91.46	93.85	96.16	98.48	100.66					
9	87.47	33	95.22	89.80	92.46	95.12	97.86	100.41						
10	87.71	34	95.57	90.46	93.53	96.58	99.54							
11	88.01	35	95.93	91.12	94.47	97.89	100.97							
12	88.27	36	96.21	91.79	95.53	99.17								
13	88.59	37	96.59	92.53	96.60	100.50								
14	88.89	38	96.88	93.21	97.56									
15	89.21	39	97.25	93.84	98.53									
16	89.21	40	97.62	94.48	99.51									
17	89.84	41	97.95	95.18	100.52									
18	89.83	42	98.26	95.91										
19	90.52	43	98.56	96.57										
20	90.52	44	98.94	97.21										
21	91.19	45	99.21	97.96										
22	91.19	46	99.54	98.54										
23	91.87	47	99.54	99.20										
24	91.87	48	100.14	100.53										

Table 3.10 Crack propagation angle results for Mesh 3

Cycle No.	Crack propagation angle θ_c (Degrees)													
	$\Delta a = 0.1\ mm$			$0.2\ mm$	$0.3\ mm$	$0.4\ mm$	$0.5\ mm$	$0.6\ mm$	$0.7\ mm$	$0.8\ mm$	$0.9\ mm$	$1.0\ mm$	$1.1\ mm$	$1.2\ mm$
1	28.598	25	-0.748	28.60	28.60	28.60	28.60	28.60	28.60	28.60	28.63	28.60	28.60	28.60
2	-18.344	26	0.250	-14.03	-12.11	-11.08	-9.60	-10.25	-11.04	-11.94	-12.77	-13.53	-14.25	-14.98
3	15.359	27	-0.608	10.16	6.41	3.35	-0.21	-0.49	-0.42	-0.06	0.25	0.65	0.99	1.46
4	-9.106	28	0.218	-5.02	-4.69	-3.31	-2.07	-2.04	-2.08	-2.22	-2.38	-2.67	-2.77	-3.00
5	7.211	29	-0.557	1.07	0.67	-0.52	-0.99	-0.99	-1.02	-0.94	-0.80	-0.52	-0.44	-0.32
6	-4.001	30	0.008	-1.52	-1.74	-1.16	-0.90	-0.98	-0.94	-0.95	-0.97	-1.10	-1.11	
7	2.354	31	-0.195	-0.60	-0.45	-0.72	-0.87	-0.72	-0.63	-0.67	-0.62			
8	-1.409	32	-0.276	-0.81	-0.82	-0.69	-0.70	-0.61	-0.64					
9	0.055	33	0.049	-0.50	-0.60	-0.58	-0.50	-0.57						
10	-0.669	34	-0.393	-0.65	-0.52	-0.54	-0.45							
11	-0.305	35	0.083	-0.44	-0.49	-0.47	-0.46							
12	-0.459	36	-0.233	-0.43	-0.51	-0.34								
13	-0.392	37	-0.146	-0.37	-0.31	-0.40								
14	-0.371	38	-0.025	-0.36	-0.29									
15	-0.308	39	-0.267	-0.32	-0.34									
16	0.077	40	0.039	-0.37	-0.31									
17	-0.962	41	-0.203	-0.27	-0.32									
18	0.361	42	-0.081	-0.30										
19	-0.884	43	-0.066	-0.27										
20	0.367	44	-0.193	-0.27										
21	-0.859	45	-0.015	-0.19										
22	0.379	46	-0.156	-0.14										
23	-0.899	47	0.056	-0.28										
24	0.364	48	-0.335	-0.15										

Table 3.11 Service life results for Mesh 3

Cycle No.	Service life N (Cycles)													
	$\Delta a = 0.1\ mm$			$0.2\ mm$	$0.3\ mm$	$0.4\ mm$	$0.5\ mm$	$0.6\ mm$	$0.7\ mm$	$0.8\ mm$	$0.9\ mm$	$1.0\ mm$	$1.1\ mm$	$1.2\ mm$
1	3624	25	2341	7247	10871	14495	18118	21742	25366	28989	32671	36237	39860	43484
2	3670	26	2341	6739	9743	12537	15209	18111	20973	23846	26718	29481	32184	34793
3	3239	27	2282	6056	8824	11501	14062	16486	18791	20953	23025	24920	26684	28437
4	3251	28	2282	5885	8528	10979	13216	15285	17207	18942	20502	21954	23213	24492
5	3032	29	2231	5716	8208	10431	12412	14152	15691	17076	18284			
6	2997	30	2204	5594	7920	9919	11623	13067	14365	15471				
7	2920	31	2176	5469	7622	9411	10908	12133	13196					
8	2892	32	2149	5335	7321	8920	10241	11305						
9	2853	33	2119	5205	7048	8511	9630							
10	2826	34	2093	5072	6770	8069	9073							
11	2793	35	2065	4944	6538	7696								
12	2763	36	2044	4820	6288	7354								
13	2729	37	2017	4686	6046									
14	2697	38	1995	4568	5840									
15	2663	39	1969	4461	5642									
16	2663	40	1943	4356	5449									
17	2599	41	1920	4245										
18	2599	42	1899	4133										
19	2530	43	1879	4036										
20	2530	44	1854	3943										
21	2466	45	1836	3839										
22	2466	46	1815	3760										
23	2403	47	1815	3674										
24	2403	48	1777	3590										
Total service life:			116650	117372	118658	119822	124492	122280	125589	125277	121201	112591	121941	131206

3.6.4 Cross-mesh comparison of results

To clearly illustrate the effect of mesh refinement, plots of the crack path for same Δa value for different meshes are shown in Figure 3.20. Results for $\Delta a = 0.9 - 1.2\, mm$ are shown here as only those are available for all meshes. Oscillations reduce significantly with first level of refinement (Mesh 1 to Mesh 2). Crack paths for Mesh 2 and Mesh 3 are quite close. It should also be noted that crack path for Mesh 3 does not show any oscillations. Results for $\Delta a = 0.3 - 0.8\, mm$ for Mesh 2 and Mesh 3 exhibit similar trends.

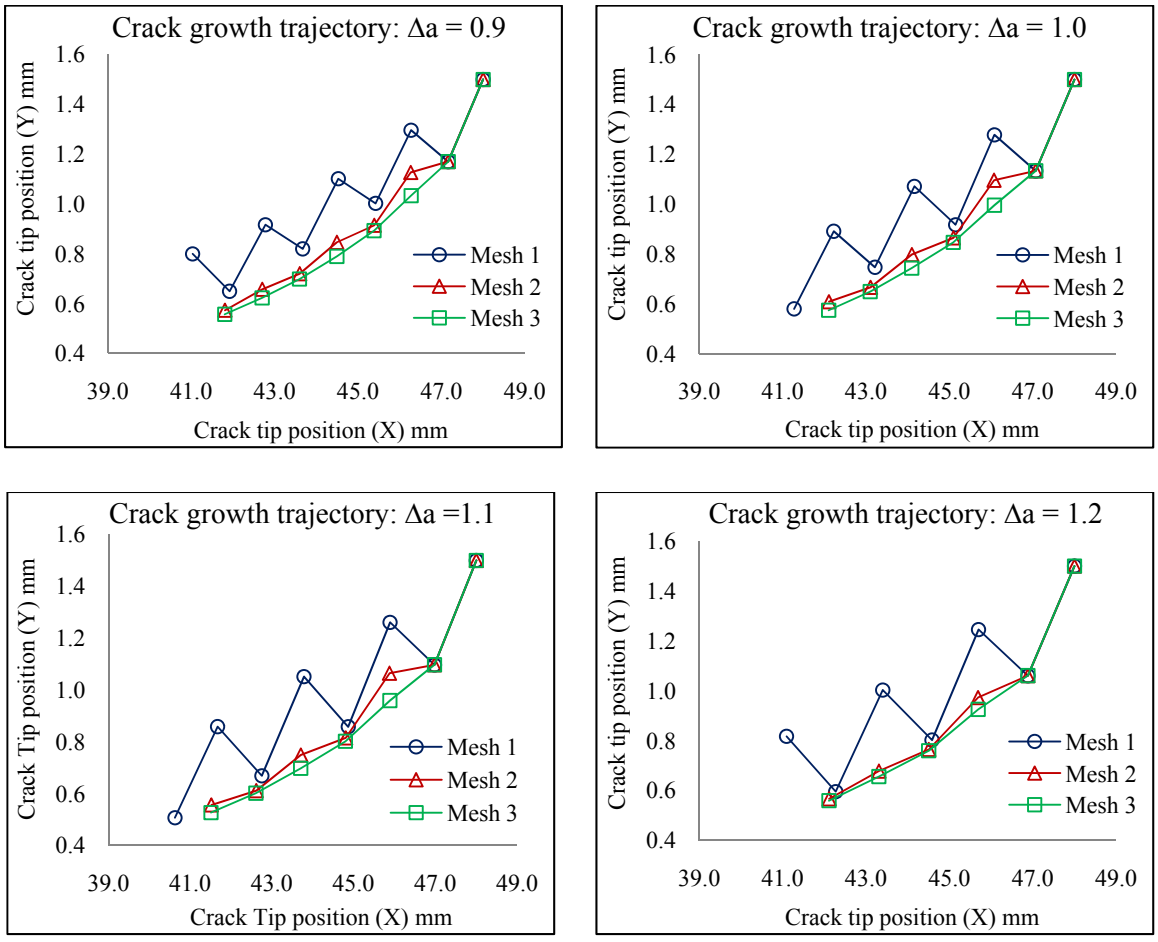

Figure 3.20 Cross-mesh comparison of crack propagation path

3.6.5 Determination of mesh size and Δa for design studies

The objective for this study was to determine appropriate level of mesh refinement and Δa value for further design studies. Notice from Table 3.4, Table 3.6, and Table 3.9 that even with different meshes, K_{eq} and N values are quite close. However, significant differences can be observed in case of θ_c, which impacts crack growth trajectory. This happens because for same Δa, mode I and mode II SIF values differ from mesh to mesh, however, the difference in equivalent SIF is not significant. Thus, even though the coarse mesh predicts fracture parameters with sufficient accuracy, it is deemed inadequate for accurate prediction of crack growth trajectory.

Since no analytical solution is available for this problem, the most refined case— $\Delta a = 0.1\ mm$ for Mesh 3— is taken as the basis for comparison. For this case, the crack terminates at (43.27, 0.73), which was deemed as the true point of failure. For all other Δa cases, crack segments exceeding this termination point were excluded. The crack trajectory was then approximated as a 2nd order curve and 2nd order polynomials were fitted through the crack-tip coordinates for different values of Δa for Mesh 2 and Mesh 3 as shown in Figure 3.21 and Figure 3.22, respectively. Since the correlation coefficient (R^2 value) for all curves is almost 1, 2nd order polynomial is a good approximation. It can be observed that although the polynomial coefficients corresponding to different Δa values are different, the curves themselves are quite close to each other. Out of all mesh and Δa combinations, the curve for Mesh 2 and $\Delta a = 0.8\ mm$ case matches most closely with the best case shown in Figure 3.23. It can be observed that these two are very close to each other. Although this combination does exhibit some oscillations, this combination was selected in the interest of saving computational burden.

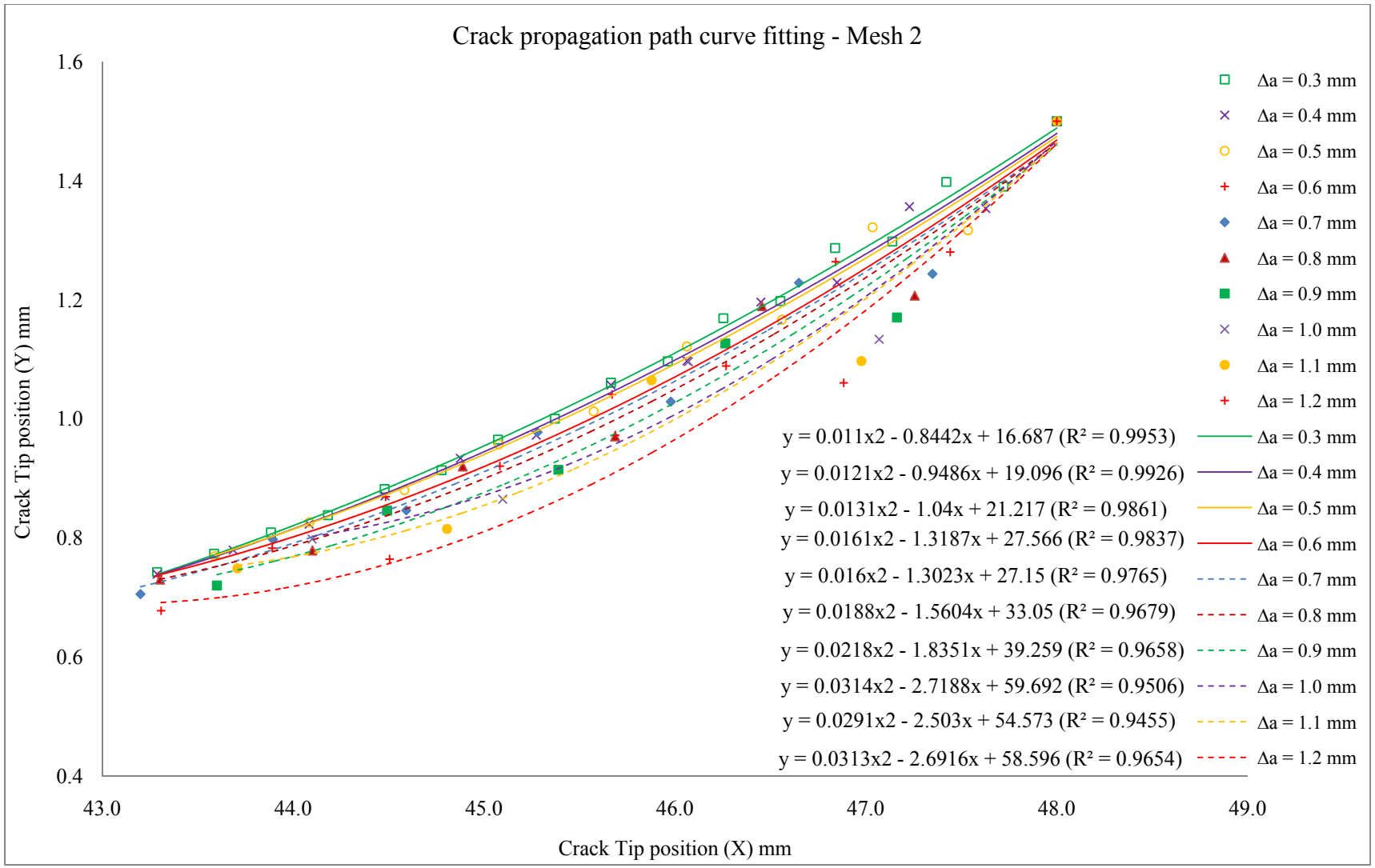

Figure 3.21 Crack propagation path curve fitting for Mesh 2

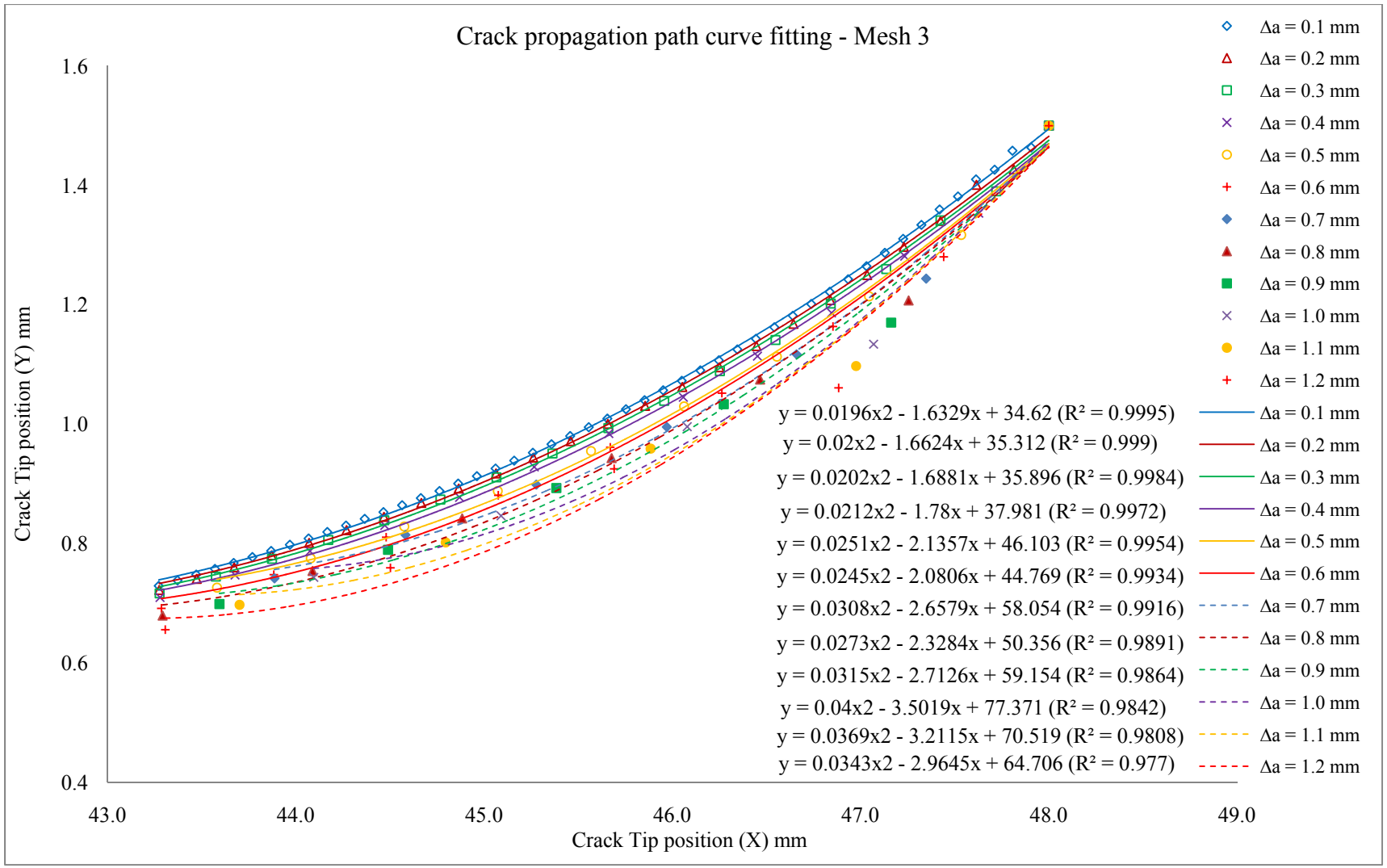

Figure 3.22 Crack propagation path curve fitting for Mesh 3

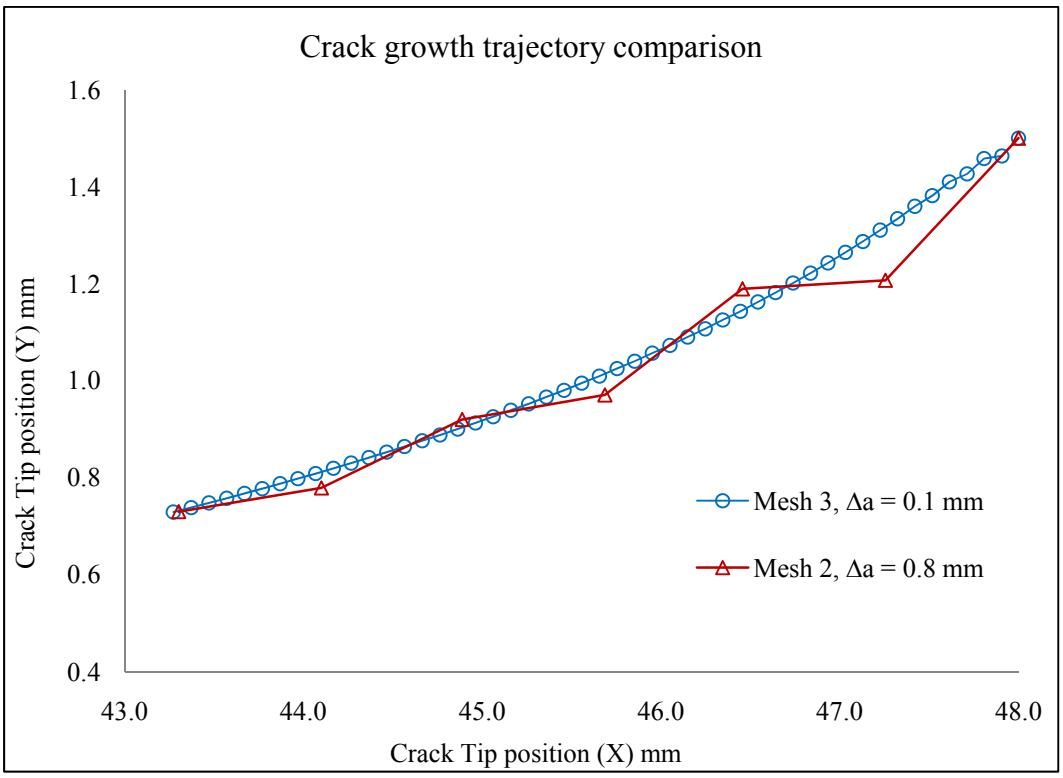

Figure 3.23 Comparison of crack propagation path for reference and selected cases

3.6.6 Crack propagation analysis results for selected mesh

For the selected mesh (mesh 2) and Δa size ($0.8\ mm$), crack propagation path and stress distribution at failure are shown in Figure 3.24 and Figure 3.25, respectively. The peculiar plastic zone shape for the plane strain condition can be observed near the crack tip region. The plastic zone size is quite small as compared to the overall size of the connecting rod and hence LEFM assumption is valid for this example.

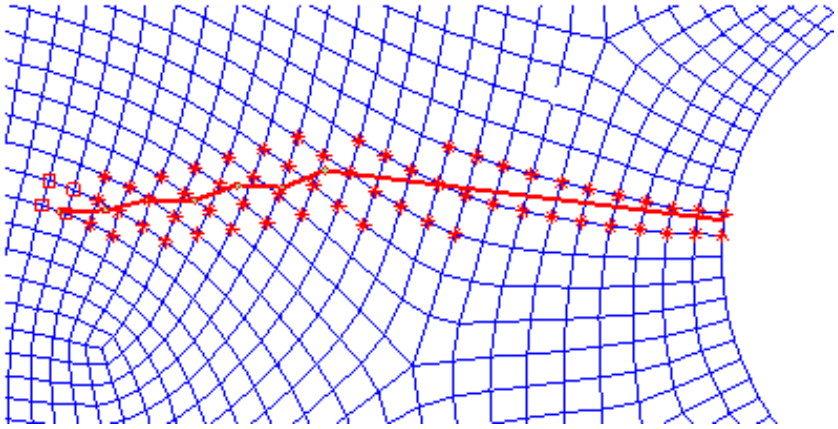

Figure 3.24 Crack propagation path for Mesh 2

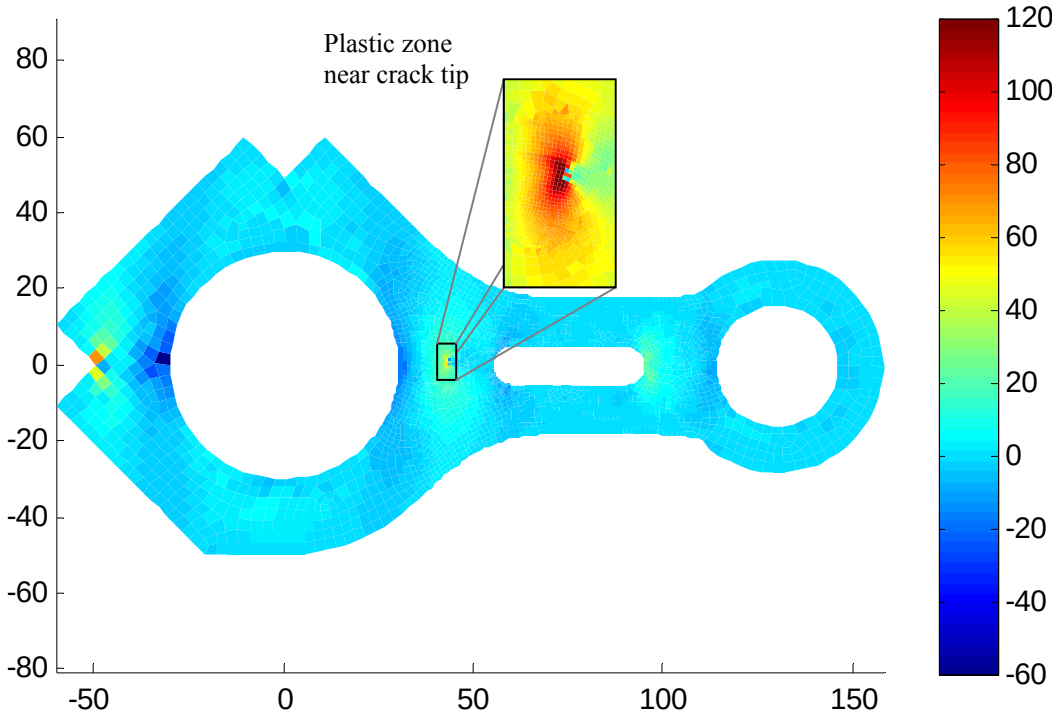

Figure 3.25 σ_{yy} (MPa) distribution for the connecting rod

Chapter 4

DESIGN SENSITIVITY ANALYSIS

During optimization process, it is necessary to compute sensitivity coefficients of the objective function and performance measures with respect to design variables. These coefficients help optimization algorithm in determining search direction towards optimum design. In shape DSA, the parameters that define shape are considered as design variables. In the context of CAD modeling, the dimensions of different features in the CAD model serve as design variables. In this chapter, different methods considered for computing design sensitivity coefficients are discussed. The concept of design velocity field, which facilitates finite element mesh update, is also introduced.

4.1 Design velocity field computation

Structural performance is measured at some specific points in the finite element model. As the design domain changes during the shape optimization process, it is necessary to update location of these points accordingly. The finite element model, being non-parametric, cannot be updated simply by updating the design variables. The design velocity field characterizes material point movements due to changes in the shape design variables and, hence, can be used to update the FEA mesh and the positions of the local structural performance measurement points.

Consider a general continuum structure undergoing the change from Ω to Ω_τ as shown in Figure 4.1. Let τ be a monotonically increasing parameter that plays the role of design time. Assume that there exists a homeomorphic mapping T, such that

$$T: x \to x_\tau(x), \quad x \in \Omega \tag{4.1}$$

with this mapping function, one can determine shape parameters at time τ as follows:

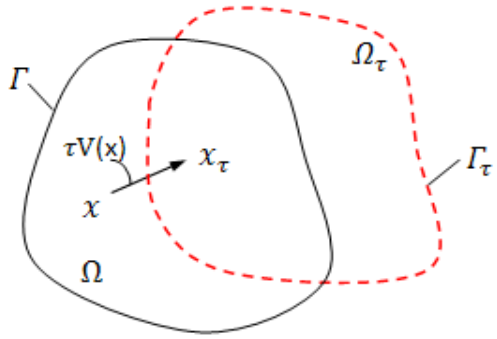

Figure 4.1 Deformation of a continuum structure

$$\begin{aligned} x_\tau &\equiv T(x,\tau), \\ \Omega_\tau &\equiv T(\Omega,\tau), \text{ and} \\ \Gamma_\tau &= T(\Gamma,\tau) \end{aligned} \tag{4.2}$$

Suppose that a material point $x \in \Omega$ in the initial domain at $\tau = 0$ moves to a new location $x_\tau \in \Omega_\tau$ in the perturbed domain. Then a design velocity field can be defined as

$$V(x_\tau,\tau) \equiv \frac{dx_\tau}{d\tau} = \frac{dT(x,\tau)}{d\tau} = \frac{\partial T(x,\tau)}{\partial \tau} \tag{4.3}$$

In the neighborhood of initial time $\tau = 0$, assuming a regularity hypothesis and ignoring higher-order terms, T can be approximated by

$$T(x,\tau) = T(x,0) + \frac{\partial T(x,0)}{\partial \tau} + O(\tau^2)$$
$$\approx x + \tau V(x,0) \tag{4.4}$$

where $x \equiv T(x,0)$ and $V(x) \equiv V(x,0)$.

For the current research, a hybrid design velocity computation method proposed by Choi & Chang (1994) is employed. In this method, design velocity is calculated in two steps. An isoparametric mapping method is first used to calculate the design velocity of the boundary points, called the boundary velocity field (BVF). Then, the boundary displacement method is used to determine the movement of interior points, called the domain velocity field. These two are then combined to obtain the overall design velocity field. A detailed account of design velocity field computation can be found in (Choi & Chang, 1994). The overall design velocity field is used to update the finite element mesh according to the following equation:

$$x(\boldsymbol{b} + \delta b_j) = x(\boldsymbol{b}) + \frac{\partial x}{\partial b_j}\delta b_j = x(\boldsymbol{b}) + V_j\,\delta b_j \tag{4.5}$$

Note that, in Equation (4.5), δb_j may assume different values depending upon the design iteration, but V_j , once calculated, can be used throughout the design optimization process.

4.2 Overall finite difference method

Overall finite difference (FD) method is simple to implement, and hence is used as an initial step in this research. In overall FD method, structural performance measures are first evaluated for the current design. Then a design variable is perturbed by a small amount. A perturbed finite element mesh is created using the design velocity field.

Analysis is carried out to evaluate the structural responses for the perturbed design. The differences between the current and perturbed responses are computed and divided by the amount of the design perturbation to obtain the first order design sensitivity coefficients for the particular design variable. An expression for the same is given by

$$\frac{\partial \psi_i(\boldsymbol{b})}{\partial b_j} \cong \frac{\Delta \psi_i(\boldsymbol{b})}{\Delta b_j} = \frac{\psi_i(\boldsymbol{b}+\Delta b_j)-\psi_i(\boldsymbol{b})}{\Delta b_j} \tag{4.6}$$

where ψ_i is a performance measure that depends on design variables vector $\boldsymbol{b}$ and Δb_j is the perturbation in j^{th} design variable. The performance measure in this case could be stresses, the stress intensity factors, crack propagation angle, or service life.

Although this method is attractive due to its simplicity, it imposes considerable computational burden as it requires evaluation of structural response for two different designs (current design and perturbed design) for every design variable perturbation in each design iteration. Furthermore, this method is sensitive to the perturbation in design variable. If the perturbation is too large relative to the mesh size, the approximation can be inaccurate; on the other hand, if the perturbation is too small, numerical truncation errors may become significant. Hence other methods were also investigated for the current research.

4.3 Continuum-based shape DSA

Continuum based material derivative technique for design sensitivity analysis was introduced by Haug *et al.* (1986). The most attractive feature of this approach is that the governing equilibrium equations of the problem are differentiated prior to discretization.

Hence this method is independent of the discretization method used. The elimination of approximation errors also makes this method more accurate.

The variational governing equation for a structural domain Ω can be written as

$$a_{\Omega}(\boldsymbol{z}, \bar{\boldsymbol{z}}) = \ell_{\Omega}(\bar{\boldsymbol{z}}) \qquad \forall\, \bar{\boldsymbol{z}} \in \boldsymbol{Z} \tag{4.7}$$

where $\boldsymbol{z}$ and $\bar{\boldsymbol{z}}$ are the actual displacements and virtual displacement fields of the structure, respectively, $\boldsymbol{Z}$ is the space of kinematically admissible virtual displacements, and $a_{\Omega}(\boldsymbol{z}, \bar{\boldsymbol{z}})$ and $\ell_{\Omega}(\bar{\boldsymbol{z}})$ are energy bilinear and load linear forms, respectively.

Neglecting the body forces, Eq. (4.7) can be written as

$$a_{\Omega}(\boldsymbol{z}, \bar{\boldsymbol{z}}) \equiv \int_{\Omega} \sigma_{ij}(\boldsymbol{z})\, \varepsilon_{ij}(\bar{\boldsymbol{z}}) d\Omega = \ell_{\Omega}(\bar{\boldsymbol{z}}) \equiv \int_{\Gamma} T_i \bar{z}_i \, d\Gamma \tag{4.8}$$

where $\sigma_{ij}(\boldsymbol{z})$ and $\varepsilon_{ij}(\bar{\boldsymbol{z}})$ are the stress and strain tensors of the displacement $\boldsymbol{z}$ and virtual displacement $\bar{\boldsymbol{z}}$, respectively; T_i is the i^{th} component of the surface traction; and $\bar{z}_i$ is the i^{th} component of $\bar{\boldsymbol{z}}$. The values of $\boldsymbol{z}$ are obtained by solving Eq. (4.7) using finite element method. After taking material derivative of both sides of Eq. (4.7), the following equation is obtained.

$$a_{\Omega}(\dot{\boldsymbol{z}}, \bar{\boldsymbol{z}}) = \ell'_{V}(\bar{\boldsymbol{z}}) - a'_{V}(\boldsymbol{z}, \bar{\boldsymbol{z}}) \qquad \forall\, \bar{\boldsymbol{z}} \in \boldsymbol{Z} \tag{4.9}$$

This equation, again, is solved for $\dot{\boldsymbol{z}}$ using finite element method. Since the same set of matrix equations needs to be solved with a different fictitious load, solution of $\dot{\boldsymbol{z}}$ is computationally efficient. The terms $\ell'_{\mathrm{V}}(\bar{\boldsymbol{z}})$ and $a'_{\mathrm{V}}(\boldsymbol{z}, \bar{\boldsymbol{z}})$ are further derived as follows:

$$\ell'_{V}(\bar{\boldsymbol{z}}) = \int_{\Gamma} \{T_i\big(z_{i,j} V_j\big) + [(T_i \bar{z}_i)_{,j} n_j + \kappa_{\Gamma}(T_i \bar{z}_i)](V_i n_i)\} d\Gamma \tag{4.10}$$

$$a'_{V}(\boldsymbol{z}, \bar{\boldsymbol{z}}) = -\int_{\Omega} [\sigma_{ij}(\boldsymbol{z})\big(\bar{z}_{i,k} V_{k,j}\big) + \sigma_{ij}(\bar{\boldsymbol{z}})\big(z_{i,k} V_{k,j}\big) - \sigma_{ij}(\boldsymbol{z}) \varepsilon_{ij}(\bar{\boldsymbol{z}}) div V] d\Omega \tag{4.11}$$

where V_j is j^{th} component of V, n_j is j^{th} component of unit normal vector n, and κ_Γ is curvature of the boundary.

Let ψ_1 be a domain functional, defined as an integral over Ω_τ

$$\psi_1 = \int_{\Omega_\tau} f_\tau(\boldsymbol{x}_\tau) d\Omega_\tau \tag{4.12}$$

where f_τ is a regular function defined on Ω_τ. If Ω is C^k regular, then the material derivative of ψ_1 at Ω is

$$\dot{\psi}_1 = \int_\Omega f'(\boldsymbol{x}) + div\big(f(\boldsymbol{x})V(\boldsymbol{x})\big) d\Omega \tag{4.13}$$

Using Eq. (4.13), sensitivity coefficients of parameters can be computed.

Although this method is theoretically sound, it works on the assumption that $\dot{z} = z' + \nabla z^T V$ is valid. The presence of strong discontinuity violates this condition, and hence application of this technique using its standard formulation is not possible. Hence this method was not implemented in this research.

4.4 Semi-analytical method

The semi-analytical method starts with FD for calculation of stiffness matrix derivatives, but computes sensitivities of rest of the parameters using analytical method. It takes advantage of the simplicity of the FD method while differentiating stiffness matrix with respect to design variables, but does not require two complete finite element solutions in design iteration unlike the FD method. It also takes advantage of the computational efficiency and accuracy that comes due to analytical computation of derivatives in the continuum method. Thus, it can be thought to be a golden mean between the two methods described earlier.

4.4.1 Sensitivity coefficients of fracture parameters

The focus of this research is on computing sensitivity coefficients of fracture parameters θ_c, and ΔN. Taking derivative of θ_c (Eq. (2.9) with respect to the design variables yields:

$$\frac{\partial \theta_c}{\partial b} = \frac{2\left[\left(1+\sqrt{1+\left(8K_{II}^2/K_I^2\right)}\right)\left(K_{II}\,\partial K_I/\partial b - K_I\,\partial K_{II}/\partial b\right)\right]}{K_I^2\left(1+\sqrt{1+\left(8K_{II}^2/K_I^2\right)}\right)+K_{II}^2\left(8+6\sqrt{1+\left(8K_{II}^2/K_I^2\right)}\right)} \tag{4.14}$$

Similarly, taking derivative of ΔN with respect to shape design variables yields:

$$\frac{\partial \Delta N}{\partial \boldsymbol{b}} = \frac{-m\cdot\Delta a}{C(\Delta K_{Ieq})^{m+1}}\frac{\partial \Delta K_{Ieq}}{\partial \boldsymbol{b}} \tag{4.15}$$

As seen from Eq. (4.14) and Eq. (4.15), sensitivity coefficients of θ_c and ΔN depend on sensitivity coefficients of K_I and K_{II}. However, the SIFs are obtained from interaction energy integral using Eq. (2.26) and Eq. (2.27). Hence, the interaction energy integral from Eq. (2.23) is differentiated with respect to design variable. Then the sensitivity coefficients of the SIFs can be easily obtained as follows:

$$\frac{\partial K_I}{\partial b_i} = \frac{E'}{2}\frac{\partial M^{(1,I)}}{\partial b_i}\text{; and } \frac{\partial K_{II}}{\partial b_i} = \frac{E'}{2}\frac{\partial M^{(1,II)}}{\partial b_i} \tag{4.16}$$

These can then be used to find sensitivity coefficients of θ_c and da/dN. A flowchart explaining the computation of sensitivity coefficients is shown in Figure 4.2.

4.4.2 Interaction energy integral sensitivity

Consider interaction energy integral as a domain functional ψ_1 defined as shown in Eq. (4.12), then the material derivative of ψ_1 at Ω is

$$\psi_1' = \int_\Omega \left[\frac{\partial f(x)}{\partial b} + f(\boldsymbol{x}) divV(\boldsymbol{x})\right] d\Omega \tag{4.17}$$

where $V(\boldsymbol{x})$ is the design velocity field that characterizes material point movements due to changes in the shape design variables and $divV(\boldsymbol{x}) = \frac{\partial V_1}{\partial x_1} + \frac{\partial V_2}{\partial x_2}$.

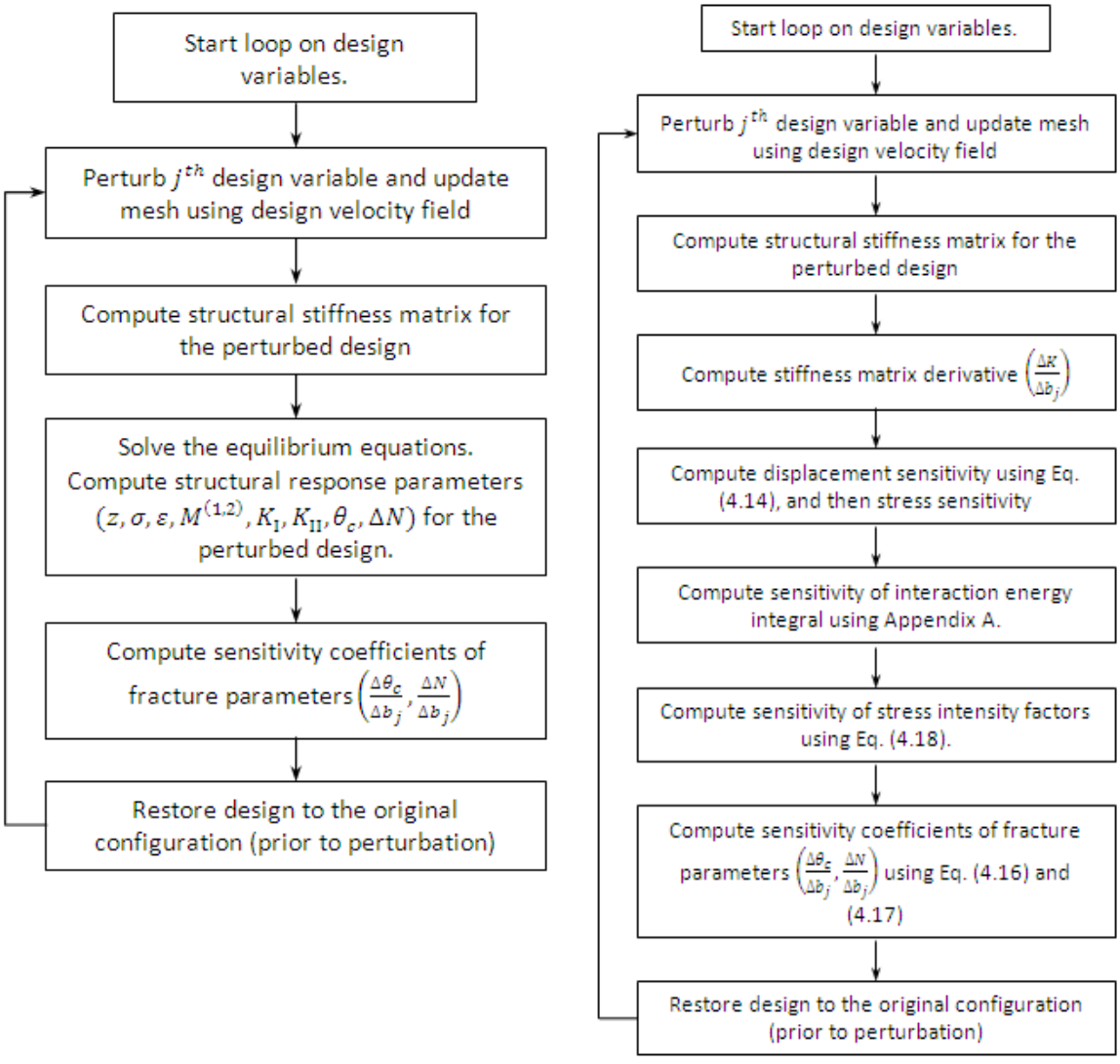

(a) Finite Difference method (b) Semi-analytical method

Figure 4.2 Procedure for computing sensitivity coefficients of fracture parameters

Applying material derivative to the interaction energy integral of Eq. (2.24) involves calculation of $\partial h_i/\partial b$ terms. In this section, only derivative of terms h_1 and h_5 are derived to explain calculation of various terms involved. Derivatives of the remaining terms in interaction integral can be found in Appendix A. Based on Eq.(2.25), derivatives of h_1 and h_5, respectively, with respect to design variable b are:

$$\frac{\partial h_1}{\partial b} = E_1 \left\{ \left[\nu_1 \frac{\partial^2 z_1^{(1)}}{\partial b \partial x_1} + \nu_2 \frac{\partial^2 z_2^{(1)}}{\partial b \partial x_2} \right] \frac{\partial z_1^{(2)}}{\partial x_1} \frac{\partial q}{\partial x_1} + \left[\nu_1 \frac{\partial z_1^{(1)}}{\partial x_1} + \nu_2 \frac{\partial z_2^{(1)}}{\partial x_2} \right] \frac{\partial^2 z_1^{(2)}}{\partial b \partial x_1} \frac{\partial q}{\partial x_1} + \left[\nu_1 \frac{\partial z_1^{(1)}}{\partial x_1} + \nu_2 \frac{\partial z_2^{(1)}}{\partial x_2} \right] \frac{\partial z_1^{(2)}}{\partial x_1} \frac{\partial^2 q}{\partial b \partial x_1} + \left[\nu_1 \frac{\partial z_1^{(1)}}{\partial x_1} + \nu_2 \frac{\partial z_2^{(1)}}{\partial x_2} \right] \frac{\partial z_1^{(2)}}{\partial x_1} \frac{\partial q}{\partial x_1} \left(\frac{\partial V_1}{\partial x_1} + \frac{\partial V_2}{\partial x_2} \right) \right\}$$

$$\frac{\partial \mathrm{h_5}}{\partial \mathrm{b}} = \frac{\partial \sigma_{12}^{(2)}}{\partial \mathrm{b}} \frac{\partial \mathrm{z_1^{(1)}}}{\partial \mathrm{x_1}} \frac{\partial \mathrm{q}}{\partial \mathrm{x_2}} + \sigma_{12}^{(2)} \frac{\partial^2 \mathrm{z_1^{(1)}}}{\partial \mathrm{b}\, \partial \mathrm{x_1}} \frac{\partial \mathrm{q}}{\partial \mathrm{x_2}} + \sigma_{12}^{(2)} \frac{\partial \mathrm{z_1^{(1)}}}{\partial \mathrm{x_1}} \frac{\partial^2 \mathrm{q}}{\partial \mathrm{b}\, \partial \mathrm{x_2}} + \sigma_{12}^{(2)} \frac{\partial z_1^{(1)}}{\partial x_1} \frac{\partial q}{\partial x_2} \left(\frac{\partial V_1}{\partial x_1} + \frac{\partial V_2}{\partial x_2} \right) \tag{4.18}$$

These terms involve first order derivatives of the actual and auxiliary state displacements $\left(\frac{\partial z_i^{(1)}}{\partial x_j} \text{ and } \frac{\partial z_i^{(2)}}{\partial x_j}\right)$, mixed second order derivatives of actual and auxiliary state displacements with respect to design variables and the spatial coordinates $\left(\frac{\partial^2 z_i^{(1)}}{\partial b \partial x_j} \text{ and } \frac{\partial^2 z_i^{(2)}}{\partial b \partial x_j}\right)$, derivatives of auxiliary state stresses with respect to design variable $\left(\frac{\partial \sigma_{ij}^{(2)}}{\partial b}\right)$, and first and mixed second order derivatives of q $\left(\frac{\partial q}{\partial x_j} \text{ and } \frac{\partial^2 q}{\partial b \partial x_j}\right)$.

Computation of the first order derivatives with respect to spatial coordinates $\frac{\partial z_i^{(1)}}{\partial x_j}$, $\frac{\partial q}{\partial x_i}$, and $\frac{\partial z_i^{(2)}}{\partial x_j}$ is straightforward. The first two can be obtained by multiplying $z_i^{(1)}$ (obtained from XFEM displacement solution) and q with shape function derivatives, respectively. Auxiliary displacements $z_i^{(2)}$ are obtained from Eq. (2.3) and (2.5) after

setting K_I and K_{II} to either 1 or 0, and their derivatives $\frac{\partial z_i^{(2)}}{\partial x_j}$ can be obtained analytically by using chain rule of differentiation as follows:

$$\frac{\partial z_i^{(2)}}{\partial x_j} = \frac{\partial z_i^{(2)}}{\partial r}\frac{\partial r}{\partial x_j} + \frac{\partial z_i^{(2)}}{\partial \theta}\frac{\partial \theta}{\partial x_j} \tag{4.19}$$

Computation of derivatives involving design variable b employs the semi-analytical method, which requires perturbing the design variable by a small amount δb and updating the finite element mesh for the perturbed design using design velocity field V, i.e.,

$$\boldsymbol{x}(b + \delta b) = \boldsymbol{x}(b) + V\delta b \tag{4.20}$$

The design velocity field is computed as discussed in section 4.1. The second order derivatives $\frac{\partial^2 z_i^{(1)}}{\partial b \partial x_j}$ are computed using semi-analytical method as follows. Consider the discretized static equilibrium equation $Kz = F$ in the finite element form, where K is the reduced stiffness matrix. Taking derivative with respect to design variable b, and rearranging yields:

$$\frac{\partial z_i^{(1)}}{\partial b} = K^{-1}\left(\frac{\partial F}{\partial b} - \frac{\partial K}{\partial b} z_i\right) \tag{4.21}$$

$\partial z_i^{(1)}/\partial b$ can be easily obtained by solving Eq. (4.21). To obtain $\partial K/\partial b$ and $\partial F/\partial b$, the design is perturbed by a small amount δb, stiffness matrix and force vector for this perturbed design are calculated, and the derivative is obtained using finite difference as follows:

$$\frac{\partial K}{\partial b} \approx \frac{\Delta K}{\delta b} = \frac{K(b+\delta b) - K(b)}{\delta b} \tag{4.22}$$

$\frac{\partial^2 z_i^{(1)}}{\partial b \partial x_i}$ is then obtained by multiplying $\frac{\partial z_i^{(1)}}{\partial b}$ with shape function derivatives. $\frac{\partial q}{\partial x_i}$, $\frac{\partial z_1^{(2)}}{\partial x_i}$, $\sigma_{ij}^{(2)}$ are computed at the perturbed design analytically, and $\frac{\partial^2 q}{\partial b \partial x_i}$, $\frac{\partial^2 z_i^{(2)}}{\partial b \partial x_i}$, and $\frac{\partial \sigma_{ij}^{(2)}}{\partial \mathrm{b}}$ are then computed using finite difference method. Note that the finite element calculations are efficient since analytical expressions of these terms are available. The design perturbation δb must be chosen carefully to minimize errors due to numerical truncation.

Also note that the level set functions (and thus, the enriched nodes and associated enrichment functions) for original and perturbed design remain unchanged. This ensures that the stiffness matrices for the original and perturbed design have same dimensions. This assumption is valid for small design perturbations, such as those used in this research.

4.4.3 Advantages of the proposed sensitivity analysis method

The proposed method calculates sensitivity coefficients of fracture parameters with respect to shape design variables. Since no re-meshing is required due to XFEM and LSM, sensitivity coefficients of fracture parameters can be calculated throughout crack propagation cycle. This is the significant advantage of this method over other sensitivity analysis techniques developed earlier. It must be emphasized that in Eq.(4.22), inverse of stiffness matrix for only the original design is required; it is not necessary to compute inverse of stiffness matrix for the perturbed design. Further, auxiliary stresses and auxiliary displacement derivatives for current and perturbed designs are computed analytically. This saves considerable computational burden and makes this method very efficient.

4.5 Shape DSA results for rectangular plate under shear load

As a first step, DSA was carried out for the 2-D plate example shown in Figure 3.8. Semi-analytical method was used to compute sensitivity coefficients of fracture parameters for the four crack growth cycles. The results obtained by semi-analytical method were compared with finite difference method. The sensitivity coefficients with respect to the design variable (plate width, w) are summarized in Table 4.1. The results from these two methods agree very well with each other.

Table 4.1 Sensitivity analysis results for edge crack under shear load

Cycle No.	(1) $K_I(\mathrm{w})\ (Ksi\sqrt{in})$	(2) $K_I(\mathrm{w}+\Delta w)(Ksi\sqrt{in})$	(3) = (2)-(1) Finite Diff.	(4) $(\partial K_I/\partial \mathrm{w})\ \Delta \mathrm{w}$	(5)=(4)*100/(3) % Agreement
1	3.329319E+01	3.328599E+01	-7.195563E-03	-7.193584E-03	99.97
2	3.799443E+01	3.798866E+01	-5.769076E-03	-5.765511E-03	99.94
3	4.360749E+01	4.359748E+01	-1.001854E-02	-1.001542E-02	99.97
4	4.933830E+01	4.932854E+01	-9.766005E-03	-9.763089E-03	99.97

	$K_{II}(\mathrm{w})\ (Ksi\sqrt{in})$	$K_{II}(\mathrm{w}+\Delta w)(Ksi\sqrt{in})$	(3) = (2)-(1)	$(\partial K_{II}/\partial \mathrm{w})\ \Delta \mathrm{w}$	(5)=(4)*100/(3)
1	4.507298E+00	4.506767E+00	-5.304489E-04	-5.304833E-04	100.01
2	-3.303423E-03	-2.883941E-03	4.194812E-04	4.217090E-04	100.53
3	9.783003E-02	9.800447E-02	1.744468E-04	1.743026E-04	99.92
4	-3.783166E-02	-3.788122E-02	-4.956017E-05	-5.202629E-05	104.98

	$\Delta N(\mathrm{w})$	$\Delta N(\mathrm{w}+\Delta w)$	(3) = (2)-(1)	$(\partial \Delta N/\partial \mathrm{w})\ \Delta \mathrm{w}$	(5)=(4)*100/(3)
1	2.030975E+05	2.032500E+05	1.524461E+02	1.523313E+02	99.92
2	1.320481E+05	1.321183E+05	7.020004E+01	7.013272E+01	99.90
3	8.152376E+04	8.158934E+04	6.558444E+01	6.553014E+01	99.92
4	5.291841E+04	5.295509E+04	3.667745E+01	3.665016E+01	99.93

	$\theta_c(\mathrm{w})$	$\theta_c(\mathrm{w}+\Delta w)$	(3) = (2)-(1)	$(\partial \theta_c/\partial \mathrm{w})\ \Delta \mathrm{w}$	(5)=(4)*100/(3)
1	-2.600307E-01	-2.600543E-01	-2.364130E-05	-2.362035E-05	99.91
2	1.738898E-04	1.518317E-04	-2.205814E-05	-2.217207E-05	100.52
3	-4.486792E-03	-4.495825E-03	-9.033351E-06	-9.024342E-06	99.90
4	1.533559E-03	1.535872E-03	2.312995E-06	2.412414E-06	104.30

The first two columns in Table 4.1 show fracture parameters for the current and perturbed design (with a perturbation of $\Delta w = 0.001\ in$), respectively. Note that perturbed design requires calculation of inverse of the stiffness matrix for determining fracture parameters. The third column shows the finite difference and the fourth column shows sensitivity coefficient obtained by the proposed method. Last column shows the accuracy of the proposed method as compared with the overall finite difference method.

It can be observed that the proposed method is very accurate. Negative sensitivity coefficients for K_I indicate that as plate width increases, K_I decreases. Further, with each crack growth increment, K_I increases and the service life decreases. The service life is highly sensitive to design variable, whereas the sensitivity of crack growth direction is quite low.

4.6 Engine connecting rod

Table 4.2 through Table 4.6 show sensitivity coefficients of fracture parameters for the initial crack with respect to design variable b_1 through b_5, respectively. Sensitivity coefficients computed by finite difference and semi-analytical methods exhibit excellent agreement. It can be observed that sensitivity of service life decreases as the crack length increases. This behavior is expected since the service life sensitivity has an inverse exponential relation with the SIFs, and SIFs increase with increase in crack length.

It was observed that for the connecting rod example, DSA with respect to one design variable using the proposed semi-analytical method and overall finite difference method required 63.2 seconds and 107 seconds, respectively. Thus, the proposed sensitivity analysis method is about 41% faster than the overall finite difference method.

Table 4.2 Sensitivity analysis results for engine connecting rod ($\Delta b_1 = 0.005\ mm$)

Cycle No.	(1) $K_I(\boldsymbol{b})$ $(MPa\sqrt{mm})$	(2) $K_I(\boldsymbol{b}+\Delta b_1)(MPa\sqrt{mm})$	(3) = (2)-(1) Finite Diff.	(4) $(\partial K_I/\partial b_1)\,\Delta b_1$	(5)=(4)*100/(3) % Agreement
1	7.823970E+01	7.823980E+01	9.587144E-05	9.583712E-05	99.96
2	8.132033E+01	8.132041E+01	7.427470E-05	7.423155E-05	99.94
3	8.688739E+01	8.688747E+01	7.950723E-05	7.946694E-05	99.95
4	8.988034E+01	8.988039E+01	5.432642E-05	5.427360E-05	99.90
5	9.407758E+01	9.407763E+01	5.546475E-05	5.541738E-05	99.91
6	9.663262E+01	9.663266E+01	4.475336E-05	4.469494E-05	99.87
7	9.972024E+01	9.972027E+01	2.961500E-05	2.956222E-05	99.82

	$K_{II}(\boldsymbol{b})$ $(MPa\sqrt{mm})$	$K_{II}(\boldsymbol{b}+\Delta b_1)(MPa\sqrt{mm})$	(3) = (2)-(1)	$(\partial K_{II}/\partial b_1)\,\Delta b_1$	(5)=(4)*100/(3)
1	-2.297324E+01	-2.297323E+01	9.837125E-06	9.854779E-06	100.18
2	1.900624E+01	1.900628E+01	3.732554E-05	3.732119E-05	99.99
3	-1.700019E+01	-1.700019E+01	5.926134E-06	5.941946E-06	100.27
4	1.490597E+01	1.490601E+01	3.631136E-05	3.631076E-05	100.00
5	-1.093157E+01	-1.093156E+01	1.681629E-05	1.683090E-05	100.09
6	1.062819E+01	1.062822E+01	2.973638E-05	2.974180E-05	100.02
7	-7.768668E+00	-7.768663E+00	5.249270E-06	5.264189E-06	100.28

	$\Delta N(\boldsymbol{b})$	$\Delta N(\boldsymbol{b}+\Delta b_1)$	(3) = (2)-(1)	$(\partial \Delta N/\partial b_1)\,\Delta b_1$	(5)=(4)*100/(3)
1	2.917784E+04	2.917773E+04	-1.117327E-01	-1.116854E-01	99.96
2	2.684004E+04	2.683995E+04	-9.091234E-02	-9.086416E-02	99.95
3	2.187770E+04	2.187763E+04	-6.650024E-02	-6.646354E-02	99.94
4	1.979040E+04	1.979035E+04	-4.526261E-02	-4.522298E-02	99.91
5	1.727856E+04	1.727853E+04	-3.393949E-02	-3.390842E-02	99.91
6	1.576995E+04	1.576992E+04	-2.710253E-02	-2.706992E-02	99.88
7	1.427453E+04	1.427451E+04	-1.454425E-02	-1.451739E-02	99.82

	$\theta_c(\boldsymbol{b})$ (Deg)	$\theta_c(\boldsymbol{b}+\Delta b_1)$ (Deg)	(3) = (2)-(1)	$(\partial \theta_c/\partial b_1)\,\Delta b_1$	(5)=(4)*100/(3)
1	4.999941E-01	4.999935E-01	-6.098540E-07	-6.099759E-07	100.02
2	-4.189508E-01	-4.189512E-01	-3.564912E-07	-3.565940E-07	100.03
3	3.612377E-01	3.612373E-01	-3.907686E-07	-3.909131E-07	100.04
4	-3.126359E-01	-3.126364E-01	-5.100175E-07	-5.101705E-07	100.03
5	2.254768E-01	2.254764E-01	-4.519510E-07	-4.521281E-07	100.04
6	-2.140708E-01	-2.140713E-01	-4.736055E-07	-4.738317E-07	100.05
7	1.536595E-01	1.536594E-01	-1.453861E-07	-1.455941E-07	100.14

Table 4.3 Sensitivity analysis results for engine connecting rod ($\Delta b_2 = 0.005$ mm)

Cycle No.	(1) $K_I(\boldsymbol{b})$ $(MPa\sqrt{mm})$	(2) $K_I(\boldsymbol{b}+\Delta b_1)(MPa\sqrt{mm})$	(3) = (2)-(1) Finite Diff.	(4) $(\partial K_I/\partial b_1)\,\Delta b_1$	(5)=(4)*100/(3) % Agreement
1	7.823970E+01	7.823982E+01	1.172926E-04	2.345986E-01	100.01
2	8.132033E+01	8.132042E+01	9.066349E-05	1.813238E-01	100.00
3	8.688739E+01	8.688747E+01	8.613315E-05	1.722986E-01	100.02
4	8.988034E+01	8.988041E+01	7.118167E-05	1.423599E-01	100.00
5	9.407758E+01	9.407764E+01	6.469995E-05	1.296082E-01	100.16
6	9.663262E+01	9.663267E+01	5.738838E-05	1.148136E-01	100.03
7	9.972024E+01	9.972025E+01	8.088620E-06	1.636065E-02	101.13

	$K_{II}(\boldsymbol{b})$ $(MPa\sqrt{mm})$	$K_{II}(\boldsymbol{b}+\Delta b_1)(MPa\sqrt{mm})$	(3) = (2)-(1)	$(\partial K_{II}/\partial b_1)\,\Delta b_1$	(5)=(4)*100/(3)
1	-2.297324E+01	-2.297323E+01	1.647527E-05	3.297707E-02	100.08
2	1.900624E+01	1.900627E+01	2.546720E-05	5.095538E-02	100.04
3	-1.700019E+01	-1.700019E+01	7.159124E-06	1.433586E-02	100.12
4	1.490597E+01	1.490602E+01	4.268133E-05	8.538933E-02	100.03
5	-1.093157E+01	-1.093155E+01	2.674615E-05	5.354249E-02	100.09
6	1.062819E+01	1.062820E+01	1.382506E-05	2.768442E-02	100.12
7	-7.768668E+00	-7.768696E+00	-2.839503E-05	-5.680449E-02	100.03

	$\Delta N(\boldsymbol{b})$	$\Delta N(\boldsymbol{b}+\Delta b_1)$	(3) = (2)-(1)	$(\partial \Delta N/\partial b_1)\,\Delta b_1$	(5)=(4)*100/(3)
1	2.917784E+04	2.917770E+04	-1.351310E-01	-2.702696E+02	100.00
2	2.684004E+04	2.683993E+04	-1.058280E-01	-2.116584E+02	100.00
3	2.187770E+04	2.187762E+04	-7.191943E-02	-1.438636E+02	100.02
4	1.979040E+04	1.979034E+04	-5.869672E-02	-1.173944E+02	100.00
5	1.727856E+04	1.727852E+04	-3.906515E-02	-7.825885E+01	100.16
6	1.576995E+04	1.576992E+04	-3.324552E-02	-6.651403E+01	100.03
7	1.427453E+04	1.427452E+04	-5.129634E-03	-1.035116E+01	100.90

	$\theta_c(\boldsymbol{b})$ (Deg)	$\theta_c(\boldsymbol{b}+\Delta b_1)$ (Deg)	(3) = (2)-(1)	$(\partial \theta_c/\partial b_1)\,\Delta b_1$	(5)=(4)*100/(3)
1	2.864755E+01	2.864750E+01	-4.683358E-05	-4.684762E-05	100.03
2	-2.400412E+01	-2.400412E+01	-4.375690E-06	-4.386806E-06	100.25
3	2.069740E+01	2.069737E+01	-2.502559E-05	-2.503808E-05	100.05
4	-1.791272E+01	-1.791275E+01	-3.304791E-05	-3.306252E-05	100.04
5	1.291887E+01	1.291883E+01	-3.814366E-05	-3.818508E-05	100.11
6	-1.226535E+01	-1.226536E+01	-8.216047E-06	-8.232591E-06	100.20
7	8.804041E+00	8.804072E+00	3.060735E-05	3.060744E-05	100.00

Table 4.4 Sensitivity analysis results for engine connecting rod ($\Delta b_3 = 0.005$ mm)

Cycle	(1)	(2)	(3) = (2)-(1)	(4)	(5)=(4)*100/(3)
No.	$K_I(\boldsymbol{b})$ $(MPa\sqrt{mm})$	$K_I(\boldsymbol{b}+\Delta b_3)(MPa\sqrt{mm})$	Finite Diff.	$(\partial K_I/\partial b_3)\,\Delta b_3$	% Agreement
1	7.823970E+01	7.824007E+01	3.645711E-04	7.292984E-01	100.02
2	8.132033E+01	8.132063E+01	2.938824E-04	5.879180E-01	100.03
3	8.688739E+01	8.688746E+01	6.977681E-05	1.399190E-01	100.26
4	8.988034E+01	8.988034E+01	3.828353E-06	7.793049E-03	101.78
5	9.407758E+01	9.407736E+01	-2.176853E-04	-4.334141E-01	99.55
6	9.663262E+01	9.663232E+01	-2.947196E-04	-5.889891E-01	99.92
7	9.972024E+01	9.971961E+01	-6.290011E-04	-1.256365E+00	99.87

	$K_{II}(\boldsymbol{b})$ $(MPa\sqrt{mm})$	$K_{II}(\boldsymbol{b}+\Delta b_3)(MPa\sqrt{mm})$	(3) = (2)-(1)	$(\partial K_{II}/\partial b_3)\,\Delta b_3$	(5)=(4)*100/(3)
1	-2.297324E+01	-2.297327E+01	-3.009677E-05	-6.027828E-02	100.14
2	1.900624E+01	1.900618E+01	-6.588977E-05	-1.317584E-01	99.98
3	-1.700019E+01	-1.700028E+01	-8.800563E-05	-1.761527E-01	100.08
4	1.490597E+01	1.490593E+01	-4.954363E-05	-9.908470E-02	100.00
5	-1.093157E+01	-1.093162E+01	-4.574744E-05	-9.134288E-02	99.83
6	1.062819E+01	1.062803E+01	-1.555014E-04	-3.109831E-01	99.99
7	-7.768668E+00	-7.768890E+00	-2.217991E-04	-4.440156E-01	100.09

	$\Delta N(\boldsymbol{b})$	$\Delta N(\boldsymbol{b}+\Delta b_3)$	(3) = (2)-(1)	$(\partial \Delta N/\partial b_3)\,\Delta b_3$	(5)=(4)*100/(3)
1	2.917784E+04	2.917739E+04	-4.487013E-01	-8.976290E+02	100.03
2	2.684004E+04	2.683973E+04	-3.050344E-01	-6.102463E+02	100.03
3	2.187770E+04	2.187762E+04	-7.384057E-02	-1.480151E+02	100.23
4	1.979040E+04	1.979040E+04	3.291153E-03	6.479747E+00	98.44
5	1.727856E+04	1.727870E+04	1.346974E-01	2.681638E+02	99.54
6	1.576995E+04	1.577012E+04	1.759799E-01	3.517020E+02	99.93
7	1.427453E+04	1.427483E+04	3.046340E-01	6.084284E+02	99.86

	$\theta_c(\boldsymbol{b})$ (Deg)	$\theta_c(\boldsymbol{b}+\Delta b_3)$ (Deg)	(3) = (2)-(1)	$(\partial \theta_c/\partial b_3)\,\Delta b_3$	(5)=(4)*100/(3)
1	2.864755E+01	2.864748E+01	-7.078160E-05	-7.076395E-05	99.98
2	-2.400412E+01	-2.400398E+01	1.376728E-04	1.376806E-04	100.01
3	2.069740E+01	2.069747E+01	7.749260E-05	7.752916E-05	100.05
4	-1.791272E+01	-1.791266E+01	5.370764E-05	5.371835E-05	100.02
5	1.291887E+01	1.291895E+01	7.908579E-05	7.887450E-05	99.73
6	-1.226535E+01	-1.226522E+01	1.346022E-04	1.346180E-04	100.01
7	8.804041E+00	8.804340E+00	2.985263E-04	2.986846E-04	100.05

Table 4.5 Sensitivity analysis results for engine connecting rod ($\Delta b_4 = 0.005$ mm)

Cycle No.	(1) $K_I(\boldsymbol{b})$ $(MPa\sqrt{mm})$	(2) $K_I(\boldsymbol{b}+\Delta b_1)(MPa\sqrt{mm})$	(3) = (2)-(1) Finite Diff.	(4) $(\partial K_I/\partial b_1)\,\Delta b_1$	(5)=(4)*100/(3) % Agreement
1	7.823970E+01	7.823971E+01	9.616628E-06	9.607671E-06	99.91
2	8.132033E+01	8.132034E+01	9.391287E-06	9.390272E-06	99.99
3	8.688739E+01	8.688740E+01	1.012141E-05	1.011293E-05	99.92
4	8.988034E+01	8.988035E+01	1.005440E-05	1.005364E-05	99.99
5	9.407758E+01	9.407759E+01	1.071246E-05	1.070482E-05	99.93
6	9.663262E+01	9.663263E+01	1.080333E-05	1.080095E-05	99.98
7	9.972024E+01	9.972025E+01	1.122919E-05	1.122171E-05	99.93

	$K_{II}(\boldsymbol{b})$ $(MPa\sqrt{mm})$	$K_{II}(\boldsymbol{b}+\Delta b_1)(MPa\sqrt{mm})$	(3) = (2)-(1)	$(\partial K_{II}/\partial b_1)\,\Delta b_1$	(5)=(4)*100/(3)
1	-2.297324E+01	-2.297324E+01	-1.084583E-07	-1.128104E-07	104.01
2	1.900624E+01	1.900625E+01	1.546427E-06	1.537308E-06	99.41
3	-1.700019E+01	-1.700019E+01	5.923496E-08	5.673535E-08	95.78
4	1.490597E+01	1.490598E+01	1.345310E-06	1.332812E-06	99.07
5	-1.093157E+01	-1.093157E+01	1.861633E-07	1.809842E-07	97.22
6	1.062819E+01	1.062819E+01	1.027594E-06	1.011839E-06	98.47
7	-7.768668E+00	-7.768668E+00	5.747615E-08	5.554737E-08	96.64

	$\Delta N(\boldsymbol{b})$	$\Delta N(\boldsymbol{b}+\Delta b_1)$	(3) = (2)-(1)	$(\partial \Delta N/\partial b_1)\,\Delta b_1$	(5)=(4)*100/(3)
1	2.917784E+04	2.917783E+04	-1.159125E-02	-1.158485E-02	99.94
2	2.684004E+04	2.684003E+04	-1.068266E-02	-1.067922E-02	99.97
3	2.187770E+04	2.187769E+04	-8.579234E-03	-8.574278E-03	99.94
4	1.979040E+04	1.979039E+04	-7.708364E-03	-7.706243E-03	99.97
5	1.727856E+04	1.727855E+04	-6.779991E-03	-6.776266E-03	99.95
6	1.576995E+04	1.576994E+04	-6.160696E-03	-6.158376E-03	99.96
7	1.427453E+04	1.427452E+04	-5.589186E-03	-5.586118E-03	99.95

	$\theta_c(\boldsymbol{b})$ (Deg)	$\theta_c(\boldsymbol{b}+\Delta b_1)$ (Deg)	(3) = (2)-(1)	$(\partial \theta_c/\partial b_1)\,\Delta b_1$	(5)=(4)*100/(3)
1	2.864755E+01	2.864755E+01	-2.504917E-06	-2.491137E-06	99.45
2	-2.400412E+01	-2.400411E+01	6.634345E-07	6.725211E-07	101.37
3	2.069740E+01	2.069740E+01	-2.137150E-06	-2.121351E-06	99.26
4	-1.791272E+01	-1.791272E+01	3.447917E-07	3.580340E-07	103.84
5	1.291887E+01	1.291887E+01	-1.604073E-06	-1.586187E-06	98.88
6	-1.226535E+01	-1.226535E+01	1.871014E-07	1.925842E-07	102.93
7	8.804041E+00	8.804040E+00	-1.044261E-06	-1.024957E-06	98.15

Table 4.6 Sensitivity analysis results for engine connecting rod ($\Delta b_5 = 0.005$ mm)

Cycle No.	(1) $K_I(\boldsymbol{b})(MPa\sqrt{mm})$	(2) $K_I(\boldsymbol{b}+\Delta b_1)(MPa\sqrt{mm})$	(3) = (2)-(1) Finite Diff.	(4) $(\partial K_I/\partial b_1)\,\Delta b_1$	(5)=(4)*100/(3) % Agreement
1	7.823970E+01	7.823961E+01	-9.348287E-05	-9.349502E-05	100.01
2	8.132033E+01	8.132024E+01	-9.162985E-05	-9.162479E-05	99.99
3	8.688739E+01	8.688729E+01	-9.893953E-05	-9.894995E-05	100.01
4	8.988034E+01	8.988024E+01	-9.837242E-05	-9.836624E-05	99.99
5	9.407758E+01	9.407747E+01	-1.049050E-04	-1.049129E-04	100.01
6	9.663262E+01	9.663251E+01	-1.058594E-04	-1.058558E-04	100.00
7	9.972024E+01	9.972013E+01	-1.109210E-04	-1.109279E-04	100.01

	$K_{II}(\boldsymbol{b})\ (MPa\sqrt{mm})$	$K_{II}(\boldsymbol{b}+\Delta b_1)(MPa\sqrt{mm})$	(3) = (2)-(1)	$(\partial K_{II}/\partial b_1)\,\Delta b_1$	(5)=(4)*100/(3)
1	-2.297324E+01	-2.297324E+01	1.328437E-06	1.301272E-06	97.96
2	1.900624E+01	1.900623E+01	-1.490746E-05	-1.492608E-05	100.12
3	-1.700019E+01	-1.700019E+01	-5.778510E-07	-6.069653E-07	105.04
4	1.490597E+01	1.490596E+01	-1.236541E-05	-1.239122E-05	100.21
5	-1.093157E+01	-1.093157E+01	-1.307619E-06	-1.340132E-06	102.49
6	1.062819E+01	1.062818E+01	-9.778944E-06	-9.811849E-06	100.34
7	-7.768668E+00	-7.768669E+00	-1.167303E-06	-1.203458E-06	103.10

	$\Delta N(\boldsymbol{b})$	$\Delta N(\boldsymbol{b}+\Delta b_1)$	(3) = (2)-(1)	$(\partial \Delta N/\partial b_1)\,\Delta b_1$	(5)=(4)*100/(3)
1	2.917784E+04	2.917795E+04	1.128026E-01	1.128073E-01	100.00
2	2.684004E+04	2.684014E+04	1.041836E-01	1.041826E-01	100.00
3	2.187770E+04	2.187778E+04	8.388260E-02	8.388641E-02	100.00
4	1.979040E+04	1.979048E+04	7.531983E-02	7.531822E-02	100.00
5	1.727856E+04	1.727863E+04	6.644046E-02	6.644291E-02	100.00
6	1.576995E+04	1.577001E+04	6.034942E-02	6.034930E-02	100.00
7	1.427453E+04	1.427458E+04	5.519214E-02	5.519402E-02	100.00

	$\theta_c(\boldsymbol{b})$ (Deg)	$\theta_c(\boldsymbol{b}+\Delta b_1)$ (Deg)	(3) = (2)-(1)	$(\partial \theta_c/\partial b_1)\,\Delta b_1$	(5)=(4)*100/(3)
1	4.999941E-01	4.999945E-01	4.193424E-07	4.198355E-07	100.12
2	-4.189508E-01	-4.189510E-01	-1.162059E-07	-1.158522E-07	99.70
3	3.612377E-01	3.612381E-01	3.626434E-07	3.632098E-07	100.16
4	-3.126359E-01	-3.126360E-01	-7.376892E-08	-7.326757E-08	99.32
5	2.254768E-01	2.254771E-01	2.622454E-07	2.628947E-07	100.25
6	-2.140708E-01	-2.140708E-01	-3.557757E-08	-3.494203E-08	98.21
7	1.536595E-01	1.536597E-01	1.887179E-07	1.894236E-07	100.37

Chapter 5

STRUCTURAL SHAPE OPTIMIZATION

5.1 Introduction to structural shape optimization

Numerical optimization techniques (also known as mathematical programming techniques) have been used to tackle structural optimization problems in the last few decades (Haftka & Gürdal, 1991). In structural shape optimization, shape parameters are selected as design variables for the optimization problem. A majority of optimization algorithms require that an initial set of design variables with their upper and lower bounds be specified. The design is then updated iteratively from this point. The iterative process is commonly expressed as follows:

$$\boldsymbol{b}^n = \boldsymbol{b}^{n-1} + \alpha \boldsymbol{d}^n \tag{5.1}$$

where n is the iteration number; $\boldsymbol{d}$ is the vector of the search direction in the design space defined by the design variables vector $\boldsymbol{b}$; and α is the step size along direction $\boldsymbol{d}$. The method of determining $\boldsymbol{d}$ and α may vary depending upon the optimization algorithm. Usually, the algorithm determines $\boldsymbol{d}$ such that a small move in this direction will reduce the objective function without violating any constraints. Gradients calculated by the DSA module are used to determine the search direction $\boldsymbol{d}$. A numerical interpolation scheme is applied to determine the step-size α. Once $\boldsymbol{b}^n$ is obtained, a new search direction and step

size are calculated using Eq. (5.2), and the process is repeated until a specified convergence criterion is satisfied. The convergence criterion depends on the design problem.

5.2 Proposed design optimization process

As mentioned in section 1.7, two types of design problems are considered in this research. In the first design problem, the goal is to maximize service life of components subject to constraints on volume (which is analogous to weight) and structural performance measures. The design problem is defined as:

$$\begin{aligned} &\text{Maximize: } N(\boldsymbol{b}) \\ &\text{Subject to: } \mathbb{V}(\boldsymbol{b}) < \mathbb{V}^{max},\ \psi_{\mathrm{i}}(\boldsymbol{b}) \leq\ \psi_i^u \\ &b_j^\ell\ \leq\ b_j\ \ \leq\ b_j^u \end{aligned} \tag{5.2}$$

where N is the service life in number of load cycles; b_j are the shape design variables with lower and upper limits b_j^l and b_j^u, respectively; $\mathbb{V}$ is the volume with the upper limit of $\mathbb{V}^{max}$; and ψ_i are the constraints on structural performance measures, such as stresses. The second design problem, which focuses on minimizing material subject to constraints on service life and structural performance measures, is defined as:

$$\begin{aligned} &\text{Minimize: } \mathbb{V}(\boldsymbol{b}) \\ &\text{Subject to: } N(\boldsymbol{b}) > N^{min},\ \psi_{\mathrm{i}}(\boldsymbol{b}) \leq\ \psi_i^u \\ &b_j^\ell\ \leq\ b_j\ \ \leq\ b_j^u \end{aligned} \tag{5.3}$$

where N^{min} is the minimum required service life.

The shape optimization process is depicted in Figure 5.1. Note that there is a crack growth analysis loop within each design iteration. In other words, for each design iteration, a complete crack growth analysis is conducted until the failure criterion is met ($K_{eq} < K_c$) and the corresponding service life is evaluated. Here K_{eq} is the equivalent mode I SIF and K_c is the fracture toughness of the material.

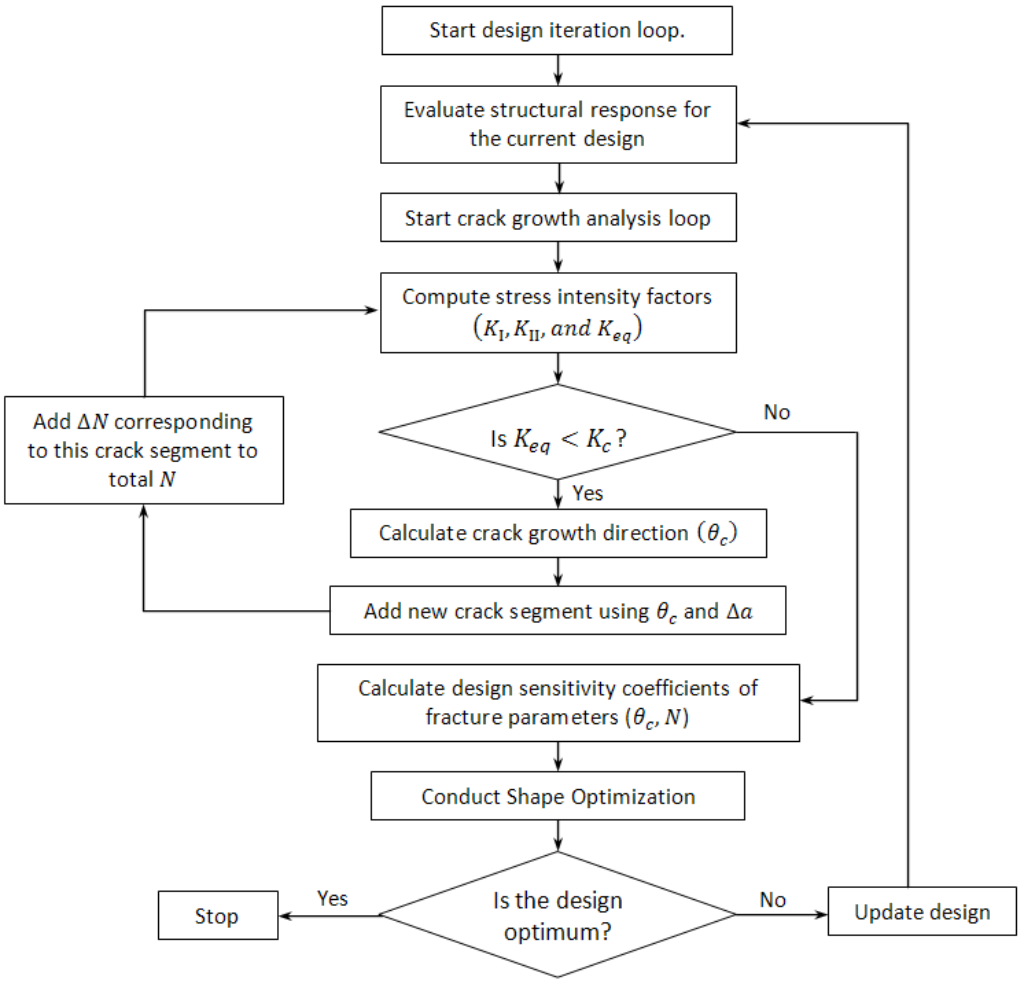

Figure 5.1 Shape optimization process

The process starts with an initial design and a given crack size and location. It is assumed that design velocity field is already computed. Structural response

(displacements and stresses) is evaluated for the initial design. Using this information, interaction energy integral and SIFs are computed. If the SIFs do not exceed the failure criteria ($K_{eq} < K_c$), then the crack growth direction is calculated and a crack segment is added to the initial crack. Service life corresponding to this crack segment is computed and added to the total service life for this design configuration. The crack growth analysis is conducted until the failure criterion is reached. Once the failure criterion is reached, sensitivity coefficients of objective function (either service life or volume), and constraints (structural performance measures) are computed using semi-analytical method. Two methods for shape optimization are demonstrated using the connecting rod example.

It is entirely possible that with changes during shape during optimization, the crack-tip element (any enriched element, for that matter) for the same crack growth cycle may differ from one design iteration to the next. This will result in an inconsistent set of elements for computation of fracture parameters during design optimization process, which is undesirable. While interaction energy integral is theoretically path independent, very marginal path dependence is observed during numerical implementation. To avoid this inconsistency, a set of elements sufficiently away from crack tip is selected for computation of interaction integral for each crack growth cycle. The same set of elements is then used for corresponding crack growth cycles during subsequent design iterations.

5.2.1 Interactive what-if analysis

First, an interactive what-if analysis method is used to optimize connecting rod shape for maximum service life. In what-if analysis, a first-order estimate of change in objective function due to change in design variables is determined (Chang, 2009).

Different design changes can be efficiently tried as change in objective function can be estimated based on the sensitivity coefficients—no crack propagation analysis is required. The design is updated and crack propagation analysis is conducted to validate new design. This procedure is performed iteratively until the design satisfies convergence criterion. Although this process requires manual intervention at every iteration, it is very useful as it offers insight into problem behavior. Further, if the problem is not very complex, this method may yield results very quickly. This method is demonstrated for shape optimization of the connecting rod for maximum service life.

5.2.2 Batch mode optimization using DOT

In this method, a commercial optimization algorithm, Design Optimization Tools (DOT), developed by Vanderplaats Research and Development is used. DOT is a general-purpose gradient-based optimization software library that can be used for solving a wide variety of design optimization problems. DOT is very flexible in terms of importing and exporting data and can be easily interfaced with C/C++ or MATLAB programs. Using an advanced option in DOT, in addition to objective and constraint function values, user can also supply gradients to DOT (VR&D, 2001). Using this information, DOT determines design changes and outputs a vector of changes in design variables.

Taking advantage of this capability, a ‘C’ program is written to interface DOT with the MATLAB program for crack propagation analysis and DSA. Batch files are written to automate data backup and to execute programs that update CAD and finite element mesh update according to design changes determined by DOT. Once an initial problem is defined as shown in Eq. (5.2) or (5.3), and parameters for optimization

algorithm are specified, the optimization process runs without any user intervention until convergence criterion is satisfied. Thus, this is a completely automated process and hence very suitable for solving complex design optimization problems that involve several design variables. This method is demonstrated for solving both design optimization problems described earlier.

5.3 Design for maximum life using what-if analysis

In this study, all five design variables for the connecting rod are considered. Constraints are imposed on minimum principal stress evaluated at certain nodes. The design problem is defined as follows:

$$\begin{aligned} &\text{Maximize: } N(\boldsymbol{b}) \\ &\text{Subject to: } \mathbb{V}(\boldsymbol{b}) < 2400\ mm^3,\ |\psi_i(\boldsymbol{b})| \leq 70\ MPa\ ,\ \ i = 1\ to\ 28 \\ &\qquad b_j^{\ell} \leq b_j \leq b_j^{u}\ ,\ \ j = 1 \text{ to } 5 \end{aligned} \tag{5.4}$$

First, crack-propagation analysis and design sensitivity analysis is performed for the initial design. The new design variables vector $\boldsymbol{b}^*$ is determined as follows:

$$\boldsymbol{b}^* = \boldsymbol{b} + \delta\boldsymbol{b} = \boldsymbol{b} + \alpha\boldsymbol{d}_j \tag{5.5}$$

where $\boldsymbol{d}_j$, the search direction for new design, is determined by normalizing vector of design sensitivity coefficients of the objective function.

$$\boldsymbol{d}_j = \left(\frac{\partial N}{\partial b_j}\right) \Big/ \left(\overline{\frac{\partial N}{\partial b}}\right), \text{ where } \overline{\frac{\partial N}{\partial b}} = \sqrt{\sum_{j=1}^{5} \left(\frac{\partial N}{\partial b_j}\right)^2} \tag{5.6}$$

Change in objective function for the new design can be obtained from the first-order estimate based on sensitivity coefficients as follows:

$$N^* = N + \sum_{j=1}^{5} \left(\frac{\partial N}{\partial b_j} \delta b_j \right), \text{ where } \delta b_j = \alpha \boldsymbol{d}_j \quad (5.7)$$

The step-size α is determined so that N^* varies about 10-15% from N. The new design is verified by conducting crack propagation analysis. If the predicted value for objective function agrees with calculated value, next design change is determined. Otherwise, the step-size is reduced and the design is verified. This procedure is continued for a number of design iterations until convergence criterion is reached. The optimization results for this study are summarized in Table 5.1 and shown in Figure 5.2. Figure 5.3 shows geometric shape for the original and optimized design. Figure 5.4 shows the crack propagation path for original and optimized design. The stress intensity factors and crack tip coordinates for the original and optimized design are summarized in Table 5.2.

Convergence was observed at the end of 10 design iterations. The study required about 16 clock hours to complete using a 3.3 GHz Intel Xeon processor. It was observed that the first four design variables reached their lower bound whereas the fifth design variable reached its upper limit. There is an increase of 64% in service life and a decrease of 12% in weight for the optimized connecting rod. From Table 5.2, it can be observed that the increase in service life largely comes from the additional crack increments and reduction in stresses. For example, for the final design, the equivalent SIF for the initial crack reduces by about 14%. Effect of decrease in SIF is amplified due to the exponent in the Paris equation (Eq. (2.6)). For this problem, $m = 3.5$. It was also observed that for this example, stress generally decreases with reduction in area. This can be seen from Table 5.3, which shows average component stresses for the elements used for interaction integral calculation for three designs—initial design, midway design, and design at lower bound. This explains increase in service life with reduction in area.

Table 5.1 What-if analysis results for the connecting rod example

Iter No.	b_1 (mm)	b_2 (mm)	b_3 (mm)	b_4 (mm)	b_5 (mm)	Volume (mm^3)	Service Life (Cycles)
1	25.000	55.000	18.000	100.000	18.500	2713.57	145,009
2	24.303	54.197	17.623	99.898	19.498	2664.58	148,419
3	22.586	51.981	15.584	99.412	19.498	2414.03	161,315
4	21.991	50.860	12.881	99.132	19.498	2132.24	196,258
5	20.041	44.299	13.926	98.098	19.498	2170.04	228,820
6	19.212	40.005	14.529	97.340	19.498	2218.35	253,008
7	18.183	40.005	14.811	90.008	19.498	2267.68	258,224
8	15.003	40.005	14.840	90.008	19.498	2245.94	250,198
9	15.003	40.005	15.740	90.008	19.498	2387.13	239,875
10	15.003	40.005	15.990	90.008	19.498	2397.33	238,253

Table 5.2 What-if analysis: Crack propagation analysis results for the connecting rod

	Original Design					Optimized Design				
Cycles	K_I	K_{II}	K_{eq} ($MPa\sqrt{mm}$)	θ_c (Deg)	Crack Tip Coordinates	K_I	K_{II}	K_{eq} $MPa\sqrt{mm}$	θ_c (Deg)	Crack Tip Coordinates
0					(48.00,1.50)					(48.00,1.50)
1	78.24	-22.97	81.54	28.65	(47.26,1.21)	67.23	-23.78	71.31	32.66	(47.28,1.16)
2	81.32	19.01	83.51	-24.00	(46.46,1.24)	70.04	21.11	73.15	-29.20	(46.48,1.21)
3	86.89	-17.00	88.53	20.70	(45.70,0.99)	76.93	-19.15	79.28	25.25	(45.74,0.91)
4	89.88	14.91	91.11	-17.91	(44.90,0.99)	80.38	17.92	82.36	-23.10	(44.94,0.93)
5	94.08	-10.93	94.71	12.92	(44.12,0.80)	86.10	-13.71	87.19	17.27	(44.17,0.72)
6	96.63	10.63	97.22	-12.27	(43.32,0.79)	89.69	13.73	90.73	-16.67	(43.37,0.73)
7	99.72	-7.77	100.2	8.80	(42.53,0.65)	94.31	-10.36	94.88	12.25	(42.58,0.57)
8						98.08	10.90	98.68	-12.38	(41.78,0.59)
9						102.15	-8.59	102.51	9.49	(40.99,0.47)

Table 5.3 Average stresses for elements used for interaction integral calculation

Elem	σ_{xx} (MPa)			σ_{yy} (MPa)			τ_{xy} (MPa)		
No.	Design 1	Design 2	Design 3	Design 1	Design 2	Design 3	Design 1	Design 2	Design 3
1	-1.51	-1.57	-1.01	3.71	3.84	2.00	-1.08	-0.78	-1.23
2	-1.73	-0.74	-1.62	0.05	1.57	3.71	-0.41	-1.45	-0.45
3	-1.91	-1.55	-0.85	5.59	0.18	1.75	0.17	-0.52	-1.46
4	-3.12	-1.73	-1.46	3.68	5.11	0.25	2.04	0.48	-0.56
5	0.60	-3.64	-3.49	4.67	0.45	0.36	-0.08	0.13	0.12
6	-1.37	-2.92	-3.56	6.14	4.38	6.48	-1.76	2.18	-0.49
7	-0.77	-3.81	-1.08	2.18	6.84	2.85	-1.67	-0.13	-1.56
8	-1.08	0.08	-1.41	3.15	4.13	3.64	-1.56	0.02	-1.07
9	-0.95	-1.10	-1.18	2.19	5.30	2.64	-1.30	-1.51	-1.07
10	-1.26	-0.88	-1.43	2.91	2.55	3.11	-1.13	-1.67	-0.69
11	-1.00	-1.23	-0.85	0.38	3.51	0.59	-0.77	-1.38	-0.96
12	-0.71	-1.03	-0.70	0.83	2.47	1.15	-1.13	-1.23	-1.32
13	-1.85	-1.33	-4.15	4.80	3.11	-0.04	-0.85	-0.94	-0.33
14	-1.98	-0.88	-2.37	5.42	0.50	0.06	-0.37	-0.90	-0.29
15	-2.93	-0.65	-1.19	2.16	1.02	4.92	1.64	-1.26	0.74
16	-3.22	-2.63	-1.43	1.04	-0.04	5.23	0.89	-0.30	0.40
17	-0.45	-1.17	-1.83	0.99	5.72	4.44	-1.46	0.64	-0.09
18	-0.51	-1.83	-1.82	1.63	4.77	4.62	-1.71	-0.44	0.32
19	-4.13	-1.86	-3.02	0.21	5.14	2.99	-0.29	0.05	1.86
20	-3.10	-2.58	-2.68	0.56	2.52	1.15	0.50	1.87	1.12
21	-4.48	-2.84	-3.01	-0.04	1.10	1.58	-0.41	1.00	1.29
22	-2.27	-0.54	-4.04	0.12	2.11	-0.08	-0.42	-1.84	-0.14
23	0.35	-3.94	-0.32	5.38	0.09	4.66	0.79	-0.22	0.79
24	0.08	-3.98	-1.05	4.57	0.01	4.47	0.53	-0.42	0.85
25	-0.68	0.06	-3.68	5.21	5.51	6.81	0.91	0.89	0.27
26	-0.96	-0.03	-3.53	6.01	4.64	6.40	0.80	0.69	1.28
27	-1.72	-0.89	-3.86	5.50	5.21	5.70	0.62	0.88	1.29
28	-4.03	-3.82	-3.41	6.26	6.82	4.52	1.18	0.75	1.85
29	-3.59	-3.49	-0.12	5.18	6.00	4.73	1.85	1.68	-0.95
30	-3.63	-0.30	0.18	7.19	4.81	4.33	1.14	-1.17	-0.35
31	-0.21	0.13	0.47	5.60	4.38	4.79	-1.56	-0.59	0.47
32	0.55	0.64	0.00	5.01	4.77	4.12	-0.90	0.23	0.23
33	-3.71	-3.18	-2.83	7.42	7.37	6.74	0.05	-0.56	-0.92
34	-3.56	-2.98	-1.83	7.05	6.64	5.73	-0.76	-1.12	-1.41
35	-2.47	-2.03	-1.78	6.37	6.67	6.76	-1.57	-1.50	-1.37
36	-2.67	-0.81	-0.87	7.44	6.29	5.31	-1.29	-1.65	-1.36

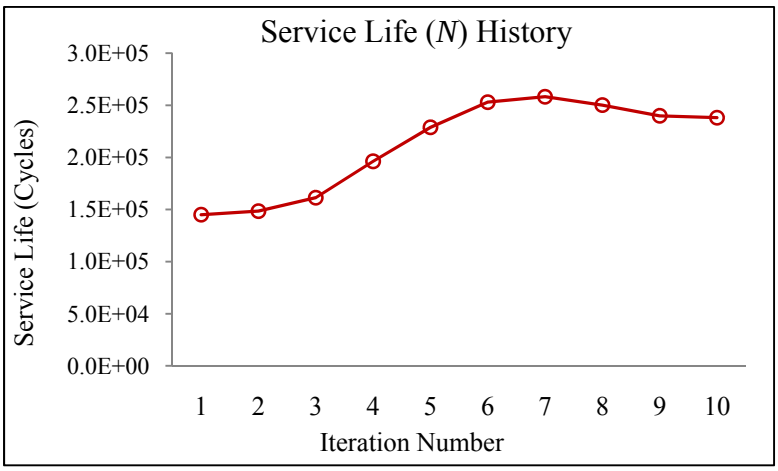

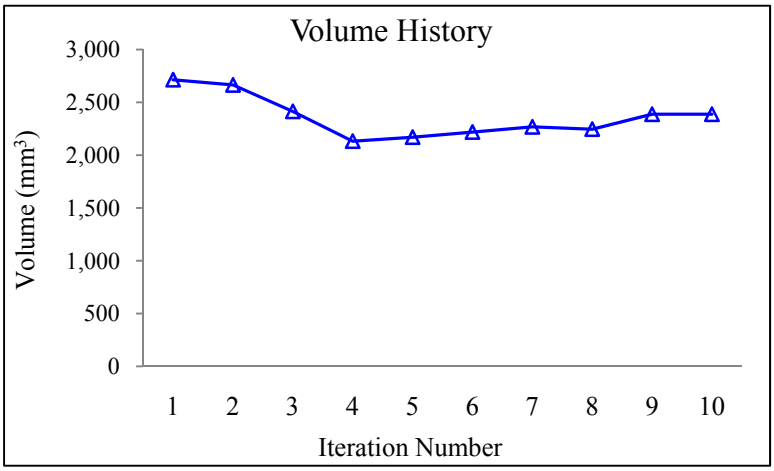

Figure 5.2 What-if analysis results: Design for maximum life of the connecting rod

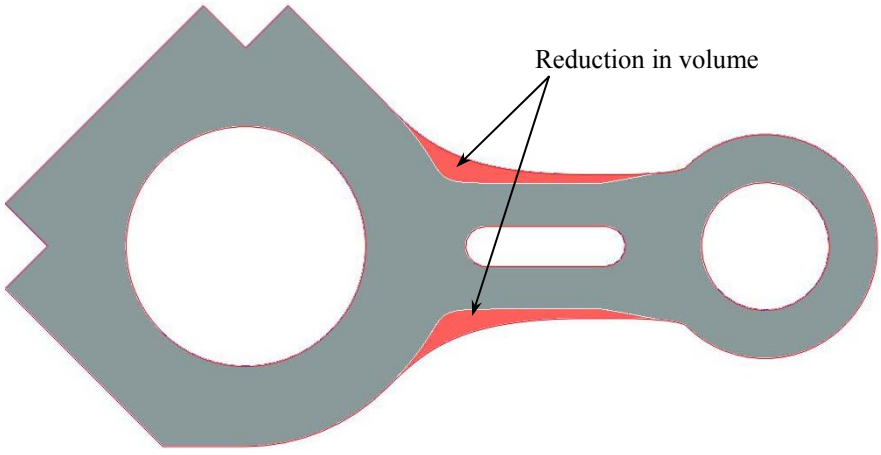

Figure 5.3 What-if analysis results: Original and optimized design

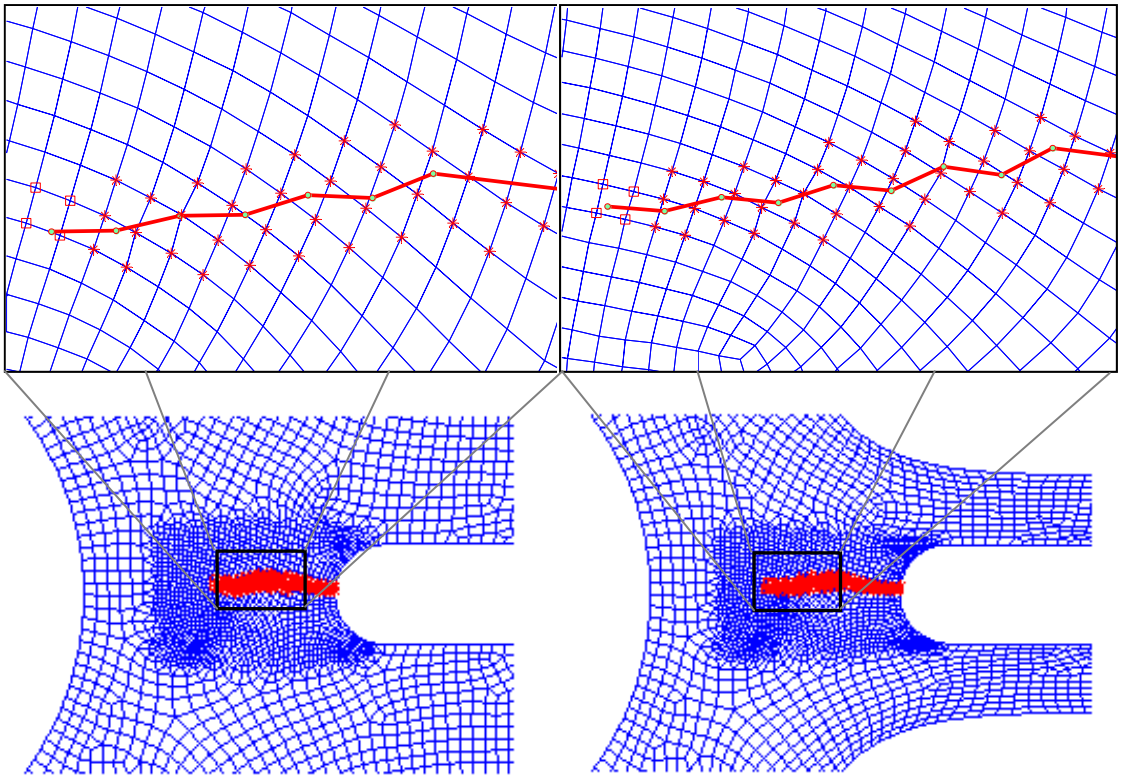

(a) Original design (b) Optimized design

Figure 5.4 What-if analysis: Crack propagation path for original and optimized design

5.4 Design for maximum life using batch-mode optimization

In this study, only the first three design variables are considered and stress constraints are imposed at 8 nodes. A constraint of $2400\,mm^3$, which corresponds to about 10% reduction in initial design, is imposed on volume. The design problem is defined as:

$$\begin{aligned} &\text{Maximize: } N(\boldsymbol{b}) \\ &\text{Subject to: } \mathbb{V}(\boldsymbol{b}) < 2400\,mm^3, |\psi_i(\boldsymbol{b})| \leq 70\,MPa, \quad i = 1\ to\ 8 \\ &\qquad b_j^{\ell} \leq b_j \leq b_j^{u}, \quad j = 1 \text{ to } 3 \end{aligned} \tag{5.8}$$

Sequential Quadratic Programming (Haftka & Gürdal, 1991) algorithm in DOT is used for optimization. The optimization results are presented in Figure 5.5 and Table 5.4. The algorithm converged in 7 SQP iterations, which required 18 crack propagation analyses and 6 sensitivity analyses. The optimization process required about 24 clock hours to complete. It was observed that b_1 and b_2, converge to their lower limit, whereas b_3 decreases initially, but later increases to satisfy violated stress constraints. Although values differ slightly, this trend is consistent with the results from what-if analysis. There is an increase of 56% in service life and a decrease of 16% in weight for the optimized connecting rod. The shape for optimal design is shown in Figure 5.6. The crack propagation path for original and optimized design is shown in Figure 5.7 and the SIFs, crack propagation angle, and crack tip coordinates for original and optimized design are summarized in Table 5.5. The optimized design allows eight crack growth increments (against 7 for the original design) while satisfying all structural performance constraints, and hence corresponding increase in life is observed.

Table 5.4 Design for maximum service life: Batch-mode optimization results

Iter No.	b_1 (mm)	b_2 (mm)	b_3 (mm)	Volume (mm^3)	Service Life (Cycles)
1	25.000	55.000	18.000	2713.57	145,010
2	23.063	45.314	16.455	2467.84	179,911
3	15.021	40.010	14.724	2236.93	233,848
4	15.049	40.006	14.923	2258.40	227,014
5	15.052	40.006	14.923	2258.41	229,666
6	15.384	40.001	15.112	2278.61	226,332
7	15.794	40.000	15.071	2274.04	226,016

Table 5.5 Design for maximum service life: Crack propagation analysis results

Cycles	Original Design					Optimized Design				
	K_I	K_{II}	K_{eq}	θ_c (Deg)	Crack Tip Coordinates	K_I	K_{II}	K_{eq}	θ_c (Deg)	Crack Tip Coordinates
	($MPa\sqrt{mm}$)					($MPa\sqrt{mm}$)				
					(48.00,1.5)					(48.00,1.5)
1	78.24	-22.97	81.54	28.65	(47.26,1.21)	66.37	-23.76	65.03	32.92	(47.28,1.15)
2	81.32	19.01	83.51	-24.00	(46.46,1.24)	69.81	20.04	66.91	-28.17	(46.48,1.18)
3	86.89	-17.00	88.53	20.70	(45.70,0.99)	77.11	-17.25	74.12	23.17	(45.73,0.90)
4	89.88	14.91	91.11	-17.91	(44.90,0.99)	80.95	15.99	78.40	-20.87	(44.93,0.90)
5	94.08	-10.93	94.71	12.92	(44.12,0.80)	86.74	-11.01	84.36	14.03	(44.16,0.71)
6	96.63	10.63	97.22	-12.27	(43.32,0.79)	90.68	10.54	89.34	-12.93	(43.36,0.69)
7	99.72	-7.77	100.2	8.80	(42.53,0.65)	95.76	-6.20	95.43	7.35	(42.56,0.58)
8						100.12	6.39	101.20	-7.25	(41.76,0.56)

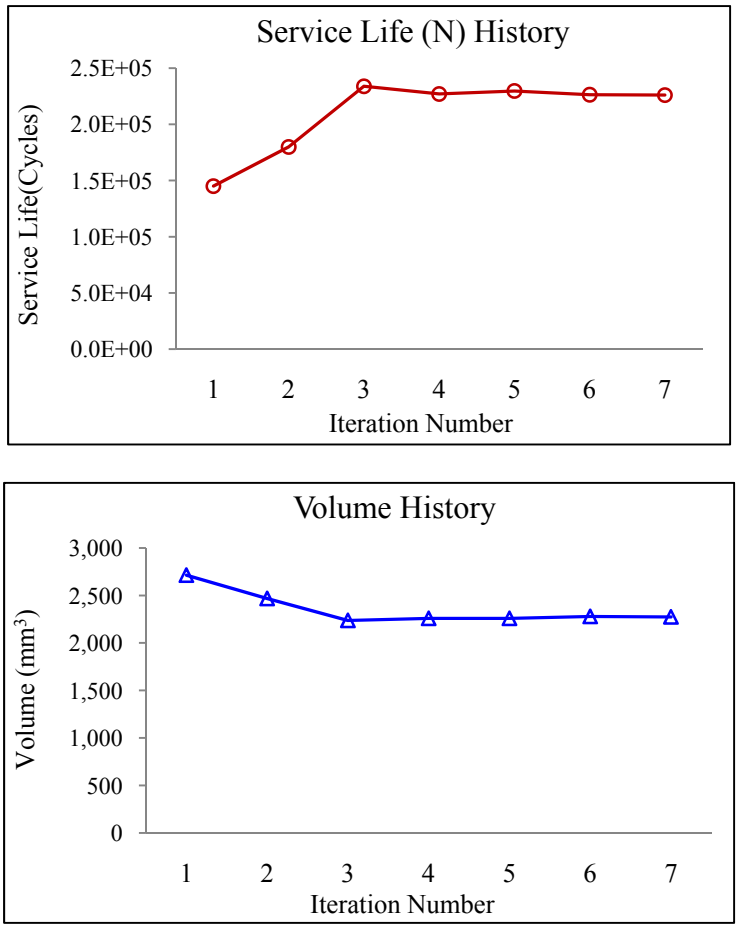

Figure 5.5 Design for maximum service life: Batch-mode optimization results

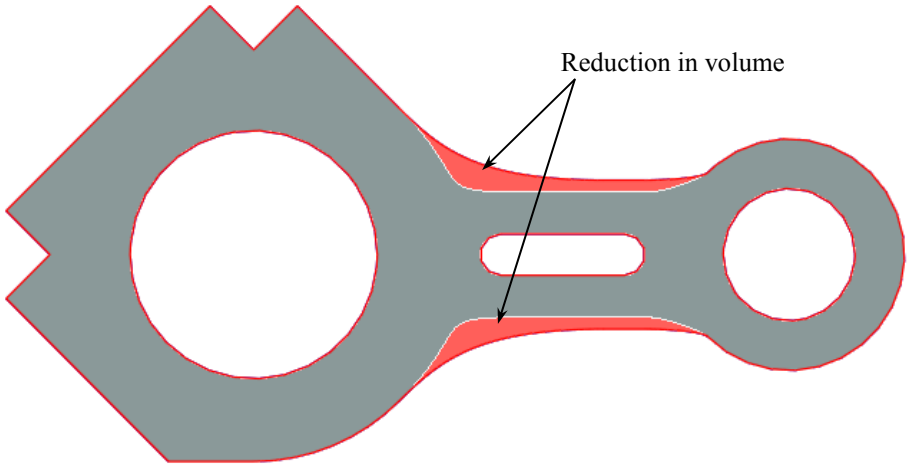

Figure 5.6 Optimization for maximum service life: Original and optimized design.

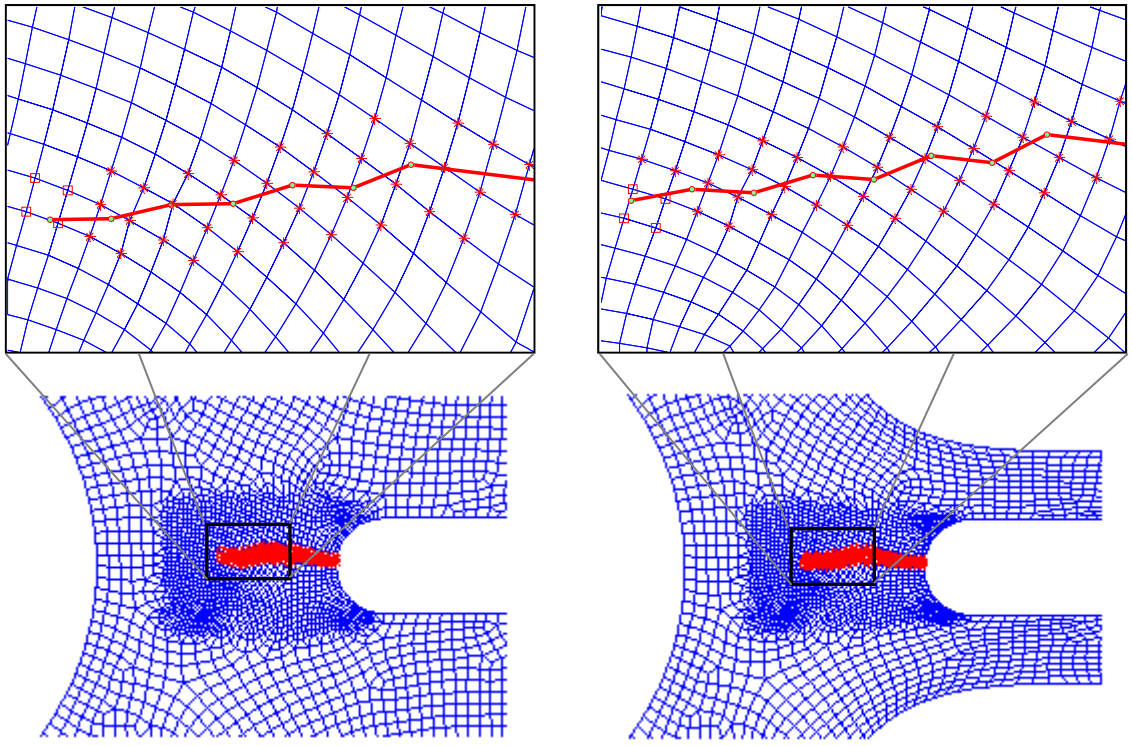

(a) Original design

(b) Optimized design

Figure 5.7 Design for maximum service life: Crack propagation path

5.5 Design for minimum weight using batch-mode optimization

In this study, only the first three design variables are considered. A lower limit of 200,000 cycles, which corresponds to 30% increase in service life, is imposed as a constraint. Stress constraints are imposed at 8 nodes located in the known high stress region. Sequential Quadratic Programming (SQP) algorithm in DOT is used for optimization. The optimization results are shown in Table 5.6 and Figure 5.8. The optimized shape of the connecting rod is shown in Figure 5.9 and the crack propagation path can be observed from Figure 5.10. The crack propagation results for original and optimized design are summarized in Table 5.7.

$$\begin{aligned} &\text{Minimize: } \mathbb{V}(\boldsymbol{b}) \\ &\text{Subject to: } N(\boldsymbol{b}) > 2 \times 10^5 \text{ cycles}, |\psi_i(\boldsymbol{b})| \leq 70\ MPa\,,\ i = 1\ to\ 8 \\ &\qquad b_j^{\ell} \leq b_j \leq b_j^{u}\,,\quad j = 1 \text{ to } 3 \end{aligned} \tag{5.9}$$

Table 5.6 Design for minimum weight: Batch-mode optimization results

Iter No.	b_1 (mm)	b_2 (mm)	b_3 (mm)	Volume (mm^3)	Service Life (Cycles)
1	25.00	55.00	18.00	2713.57	145,009
2	18.65	45.47	13.82	2178.46	214,803
3	17.50	43.75	14.13	2198.06	229,126
4	16.13	41.69	14.54	2227.76	229,364
5	15.43	40.65	14.89	2259.06	227,494
6	15.07	40.08	15.15	2283.26	225,641
7	15.00	40.00	15.13	2281.06	226,110

Table 5.7 Design for minimum weight: Crack propagation analysis results

Cycles	Original Design					Optimized Design				
	K_I	K_{II}	K_{eq}	θ_c (Deg)	Crack Tip Coordinates	K_I	K_{II}	K_{eq}	θ_c (Deg)	Crack Tip Coordinates
	(MPa$\sqrt{m}$)					(MPa$\sqrt{m}$)				
0					(48.00,1.50)					(48.00,1.50)
1	78.24	-22.97	81.54	28.65	(47.26,1.21)	66.44	-23.78	70.56	32.92	(47.28,1.15)
2	81.32	19.01	83.51	-24.00	(46.46,1.24)	69.79	20.15	72.64	-28.30	(46.48,1.19)
3	86.89	-17.00	88.53	20.70	(45.70,0.99)	77.06	-17.42	79.00	23.36	(45.73,0.90)
4	89.88	14.91	91.11	-17.91	(44.90,0.99)	80.89	16.11	82.48	-21.01	(44.93,0.90)
5	94.08	-10.93	94.71	12.92	(44.12,0.80)	86.68	-11.16	87.39	14.23	(44.16,0.71)
6	96.63	10.63	97.22	-12.27	(43.32,0.79)	90.59	10.60	91.21	-13.00	(43.36,0.69)
7	99.72	-7.77	100.2	8.80	(42.53,0.65)	95.68	-6.13	95.87	7.27	(42.57,0.58)
8						100.02	6.19	100.22	-7.03	(41.77,0.56)

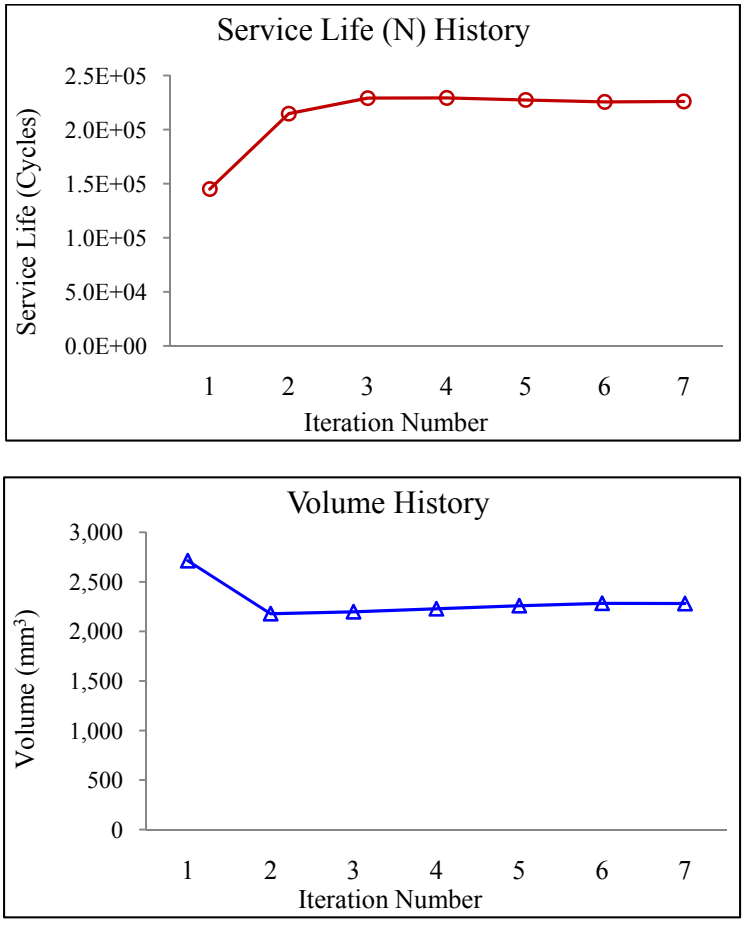

Figure 5.8 Design for minimum weight: Batch-mode optimization results

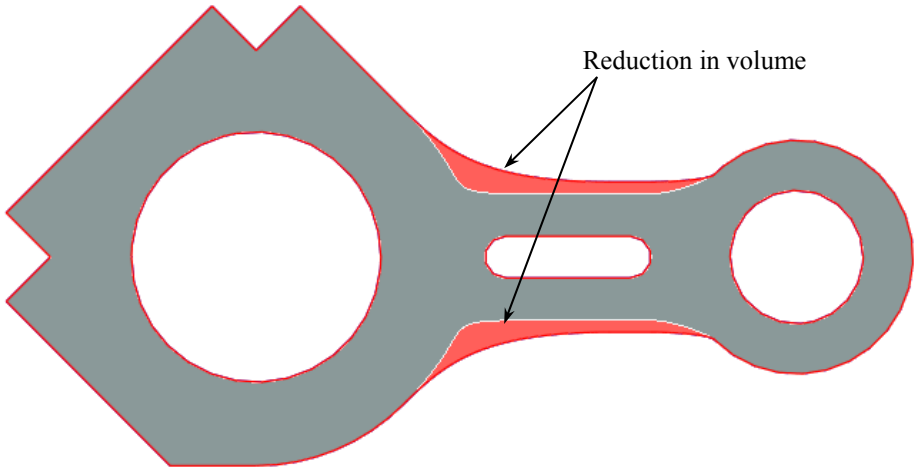

Figure 5.9 Design for minimum weight: Original and optimized design

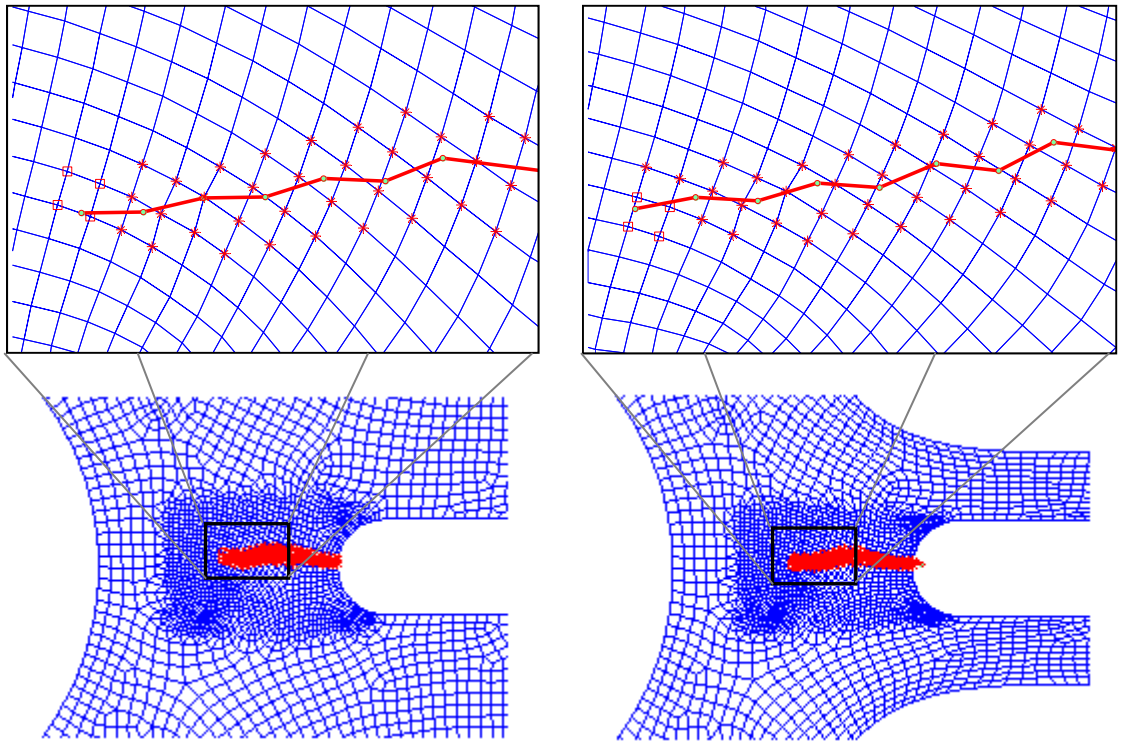

(a) Original design

(b) Optimized design

Figure 5.10 Design for minimum weight: Crack propagation path for original and optimized design

The algorithm converged in 7 SQP iterations, which required 18 crack propagation analyses and 6 sensitivity analyses. The optimization required about 24 clock hours to complete. b_1 and b_2 converge to their lower limit, whereas b_3 decreases initially, but later increases to satisfy violated stress constraints. Although values differ slightly, results for this case are almost identical to the previous one. There is a decrease of 16% in weight and an increase of 56% in service life for the optimized connecting rod.

Optimization results obtained from both interactive and batch-mode approaches indicate similar trends. The results reveal that the design corresponding to maximum service life also corresponds to the minimum weight design in this case. Note that this may not hold true for other examples. It was observed that even with more design variables (which translate into more design sensitivity analyses), the what-if analysis was faster than the batch-mode optimization, and accurately reflected problem behavior. This is because the what-if analysis requires only first-order estimate in determining step size along the search direction; whereas, SQP is a more sophisticated technique and conducts line search by solving a quadratic equation that requires evaluation of design at three different points in the design space. Thus, both optimization methods have their own place and choice should be made depending upon the design problem at hand.

Chapter 6

CONCLUSIONS AND FUTURE WORK

6.1 Conclusions

While crack propagation analysis and shape optimization have both enjoyed great attention by the research community, incorporation of crack propagation analysis into shape optimization framework has not received much attention. This research presents a design process that supports shape optimization of structural components under 2-D mixed-mode fracture for maximum service life. The main contributions of this research are:

- Incorporation of crack propagation analysis into shape optimization framework to solve two commonly used design problems: (i) Design for maximum service life and (ii) Design for minimum weight subject to a specified service life.
- Development of a reliable, accurate, and efficient semi-analytical method for computation of sensitivity coefficients of fracture parameters with respect to shape design variables for a growing crack.
- Incorporation of XFEM-LSM for crack propagation facilitates crack propagation modeling without the need for highly refined mesh or the need for re-meshing, and thus, makes this method very efficient.

In regular FEA the crack needs to align with crack faces and highly refined mesh is required to accurately capture the steep stress gradients near crack tip region. Despite several advancements in automatic mesh generation algorithms, mesh generation for complex 3-D components is still challenging. Therefore, the need for re-meshing at every step in the crack growth process adversely affects the feasibility of FEM for modeling such problems. Also, during shape optimization, crack propagation analysis needs to be performed several times. Integration of XFEM-LSM provides a more elegant and efficient way to solve crack propagation problems by effectively overcoming these limitations. Hence, incorporation of XFEM-LSM into shape optimization framework is an important and unique contribution of this research.

Considering that during design optimization process, there are several design iterations and during each iteration, DSA is performed with respect to each design variable, even a small improvement in efficiency of the DSA method is important. The novel semi-analytical DSA technique developed in this research overcomes the challenge of computing derivatives of discontinuous or unsmooth enrichment functions in XFEM and is capable of computing sensitivity coefficients of fracture parameters for a growing crack with respect to shape design variables. Both, finite difference and semi-analytical methods were implemented in this research and it was shown that the semi-analytical DSA method is up to 40% faster than the finite difference method.

The proposed design process has its roots in the damage tolerant design approach commonly used in fracture mechanics. It assumes that a crack exists in the structure and then determines its optimum geometric configuration for maximum residual service life. For designing new structural components, first crack initiation analysis should be

performed to find out most likely location and size of the crack. This design process can then be incorporated early into the design phase of these components to optimize their geometric shape for maximum service life. For components with existing parts, material can be added or removed (if feasible) to prolong their residual service life. Also, in general, this method is useful for determining effect of shape changes on the residual service life.

The design optimization process can successfully handle arbitrary 2-D geometries and can solve general design problems that are most commonly encountered, such as design for maximum life and design for minimum weight. Two different optimization approaches are also presented. Batch-mode optimization approach requires minimal user-intervention and is suitable for more complex design problems. On the other hand, what-if analysis is an extremely useful technique for gaining insight into the problem behavior and should be the preferred approach for relatively simple optimization problems.

The optimization process was completely automated using C/C++ and MATLAB codes and Windows batch files. The program can accept finite element mesh from external codes, such as ANSYS, and therefore is capable of handling any general 2-D geometry. The programs developed can be used for any 2-D example. Thus, another important contribution of this research is the development of software architecture for this optimization process.

The design process delineated here provides basic framework for solving more complex problems. The scope for further enhancements is identified next.

6.2 Future work

This research takes a definitive step towards developing a reliable technique for design of structural components for durability, but several improvements can be made to increase its scope. One notable limitation of this method is its ability to deal with only LEFM problems. An ability to incorporate effects of crack-tip plasticity (elastic-plastic fracture mechanics) would significantly increase scope of this work.

Although XFEM–LSM technique has been successfully demonstrated for 3-D applications, commercial codes for 3-D (or even 2-D) crack propagation using XFEM have started surfacing only recently. Notably, the latest release of ABAQUS (version 6.9) facilitates XFEM implementation through user defined libraries. Use of such commercial codes will provide a more standardized and easy way to apply this method to a wide range of problems. In future, this design process can be extended for 3-D applications. Also modification of current XFEM-LSM algorithm for parallel computing would significantly increase its capability to handle much more complex problems, such as those involving multiple cracks.

Continuum based material derivative technique differentiates governing equilibrium equations prior to discretization. Hence, development of a continuum based design sensitivity analysis technique would further increase accuracy, efficiency, and reliability of this process.

BIBLIOGRAPHY

Aliabadi, M. H. (1997). A new generation of boundary element methods in fracture mechanics. *International Journal of Fracture , 86*, 91-125.

Anderson, T. L. (1985). *Fracture Mechanics: Fundamentals and Applications* (2 ed.). Boca Raton, Florida, USA: CRC Press Inc.

ANSYS Commands Reference 11.1. (2008). ANSYS, Inc., Canonsburg, PA, USA.

Babuska, I., & Melenk, J. M. (1997). The partition of unity method. *International Journal for Numerical Methods in Engineering , 40*, 727-758.

Banichuk, N. V., Ivanova, S. Y., Makeev, E. V., & Sinitsin, A. V. (2005). Optimal Shape Design of Axisymmetric Shells for Crack Initiation and Propagation Under Cyclic Loading. *Mechanics Based Design of Structures and Machines , 33* (2), 253-269.

Bannerman, D. B., & Young, R. T. (1946). Some Improvements Resulting from Studies of Welded Ship Failures. *Welding Journal , 25*.

Barosum, R. S. (1974). Application of quadratic isoparametric finite elements in linear fracture mechanics. *International Journal of Fracture , 10* (4), 603-605.

Barosum, R. S. (1977). Triangular quarter-point elements as elastic and perfectly-plastic crack tip elements. *International Journal for Numerical Methods in Engineering , 11*, 85-98.

Belytschko, T., & Black, T. (1999). Elastic crack growth in finite elements with minimal remeshing. *International Journal for Numerical Methods in Engineering , 45* (5), 601-620.

Belytschko, T., & Chen, H. (2004). Singular Enrichment Finite Element Method for Elastodynamic Crack Propagation. *International Journal of Computational Methods , 1* (1), 1-15.

Belytschko, T., Moes, N., Usui, S., & Parimi, C. (2001). Arbitrary discontinuities in finite elements. *International Journal for Numerical Methods in Engineering , 50* (4), 993-1013.

Benzley, S. E. (1974). Representation of singularities with isoparametric finite elements. *International Journal for Numerical Methods in Engineering , 8*, 537-545.

Bordas, S. A. (2003). *Extended Finite Element and Level Set Methods with Applications to Growth of Cracks and Biofilms.* Ph.D. Thesis, Northwestern University, Evanston, IL, USA.

Buchholz, F. G., Chergui, A., & Dhondt, G. (1999). A comparison of SIF and SERR results with reference solutions regarding 3D and mode coupling effects for different specimens. *Proc. of the First International Conference on Fracture and Damage Mechanics* , 201-212.

Buchholz, F. G., Grebner, H., Dreyer, K. H., & Krome, H. (1988). 2D- and 3D-applications of the improved and generalized modified crack closure integral method. *Computational Mechanics , 1*, 1-14.

Chang, K. H. (2009). Shape sensitivity analysis and design studies for CAD flume sections. *Structural and Multidisciplinary Optimization , 37* (1), 91-106.

Chang, K. H., Yu, X., & Choi, K. K. (1997). Shape design sensitivity analysis and optimization for structural durability. *International Journal for Numerical Methods in Engineering , 40*, 1719-1743.

Chen, G., Rahman, S., & Park, Y. H. (2001). Shape sensitivity analysis in mixed-mode fracture mechanics. *Computational Mechanics , 27* (4), 282-291.

Chessa, J. (2002). *The Extended Finite Element Method for Free Surface and Two Phase Flow Problems.* Ph. D. thesis, Northwestern University, Evanston, IL, USA.

Choi, K. K., & Chang, K. H. (1994). A Study on Velocity Field Computation for Shape Design Optimization. *Journal of Finite Elements in Analysis and Design , 15*, 317-341.

Chow, W. T., & Atluri, S. N. (1995). Finite element calculation of stress intensity factors for interface cracks using the virtual crack closure integral. *Computational Mechanics , 16*, 1-9.

Courtin, S., Gardin, C., Bezine, G., & Ben Hadj Hamouda, H. (2005). Advantages of the J-integral approach for calculating stress intensity factors when using the commercial finite element software ABAQUS. *Engineering Fracture Mechanics , 72*, 2174–2185.

Daux, C., Moes, N., Dolbow, J., Sukumar, N., & Belytschko, T. (2000). Arbitrary cracks and holes with the extended finite element method. *International Journal for Numerical Methods in Engineering , 48* (12), 1741-1760.

deLorenzi, H. G. (1985). Energy release rate calculations by the finite element method. *Engineering Fracture Mechanics , 21*, 129-143.

deLorenzi, H. G. (1982). On the energy release rate and the J-integral for 3-D crack configurations. *International Journal of Fracture , 19*, 183-193.

Dhondt, G. (2001). 3-D mixed-mode K-calculations with the interaction integral method and the quarter point element stress method. *Comunications in Numerical Methods in Engineering , 17*, 303-307.

Dolbow, J. (1999). *An Extended Finite Element Method with Discontinuous Enrichment for Applied Mechanics.* Ph.D. thesis, Northwestern University, Evanston, IL, USA.

Dolbow, J., Moes, N., & Belytschko, T. (2000). Modeling fracture in Mindlin-Reissner plates with the eXtended finite element method. *International Journal of Solids & Structures , 37*, 7161-7183.

Erdogen, F., & Sih, G. C. (1963). On the crack extension in plates under plane loading and transverse shear. *Journal of Basic Engineering , 85*, 519-527.

Fleming, M. (1997). *The Element-Free Galerkin Method for Fatigue and Quasi-static Fracture.* Ph.D. thesis, Northwestern University, Evanston, IL, USA.

Gravouil, A., Moes, N., & Belytschko, T. (2002). Non-planar 3D crack growth by the extended finite element and the level sets--Part II: level set update. *International Journal for Numerical Methods in Engineering , 53* (11), 2569-2586.

Grootenboer, H. J. (1979). *Finite element analysis of two-dimensional reinforced concrete, taking account of nonlinear physical behaviour and the development of discrete cracks.* Ph.D. Thesis, Delft University of Technology, Delft, Netherlands.

Haftka, R. T., & Gürdal, Z. (1991). *Elements of Structural Optimization* (3 ed.). Norwell, MA, USA: Kluwer Academic Publishers.

Han, S. Y., & Lim, J. K. (2002). Shape optimization for prolonging fatigue life. *JSME International Journal Series , 45* (2), 298-304.

Harter, J. A. (2008). *AFGROW User's Guide and Technical Manual: AFGROW for Windows XP/VISTA, Version 4.0012.15.* WPAFB, OH: Air Force Research Lab.

Haug, J. E., Choi, K. K., & Komkov, V. (1986). *Design Sensitivity Analysis of Structural Systems, Mathematics in Science and Engineering* (Vol. 177). Orlando, Florida, USA: Academic Press Inc.

Henshell, R. D., & Shaw, K. G. (1975). Crack tip elements are unnecessary. *International Journal of Numerical Methods in Engineering , 9* (3), 495-509.

Huang, R., Sukumar, N., & Prevost, J. H. (2003). Modeling quasi-static crack growth with the extended finite element method. Part II: Numerical Applications. *International Journal of Solids and Structures , 40*, 7539-7552.

Hwang, H. Y., Choi, K. K., & Chang, K. H. (1997). Shape Design Sensitivity and Optimization Using p-Version Design Modeling and Finite Element Analysis. *Mechanics Based Design of Structures and Machines , 25* (1), 103-137.

Jones, R., Chaperon, P., & Heller, M. (2002). Structural optimisation with fracture strength constraints. *Engineering Fracture Mechanics , 69*, 1403-1423.

Joo, S. H., & Chang, K. H. (2001). Design for Safety of recreational water slides. *Mechanics Based Design of Structures and Machines , 29* (2), 261-294.

Matlab 2007 User's Guide. (2007). The Mathworks Inc., Natick, MA, USA.

Melenk, J. M. (1995). *On generalized finite element methods.* Ph.D. thesis, University of Maryland, College Park, MD, USA.

Melenk, J. M., & Babuska, I. (1996). *The partition of unity finite element method: Basic theory and applications.* Seminar fur Angewandte Mathematik, Eidgenossiche Technische Hochschule, Zurich, Switzerland.

Miegroet, L. V., Moes, N., Fleury, C., & Duysinx, P. (2005). Generalized Shape Optimization based on the Level Set Method. *Proc. 6th World Congress of Structural and Multidisciplinary Optimization*, (pp. 1-10). Rio De Janeiro, Brazil.

Moes, N., & Belytschko, T. (2002). Extended finite element method for cohesive crack growth. *Engineering Fracture Mechanics , 69*, 813-834.

Moes, N., Gravouil, A., & Belytschko, T. (2002). Non-planar 3D crack growth by the extended finite element and level sets. Part I: mechanical model. *International Journal for Numerical Methods in Engineering , 53* (11), 2549-2568.

Mohammadi, S. (2008). *Extended Finite Element Method For Fracture Analysis of Structures.* Hoboken, NJ, USA: John Wiley and Sons Inc.

Moran, B., & Shih, C. F. (1987). A general treatment of crack tip contour integrals. *International Journal of Fracture , 35*, 295-310.

Moran, B., & Shih, C. F. (1987). Crack tip and associated domain integrals from momentum and energy balance. *Engineering Fracture Mechanics , 27* (6), 615-642.

MSC.Software, C. (2005). MSC.Fatigue User's Guide. Santa Ana, CA, USA.

NBS. (1983). *The Economic Effects of Fracture in the United States.* Gaitherdburg, MD: National Bureau of Standards, U.S. Department of Commerce.

Ngo, D., & Scordelis, A. C. (1967). Finite element analysis of reinforced concrete beams. *Journal of American Concrete Institute , 64*, 152-163.

Nguyen, V. P. (2005). *An object-oriented approach to the eXtended Finite Element Method with Application to Fracture Mechanics.* Ph.D. Thesis, Hochiminh City University of Technology, Vietnam.

Nilson, A. H. (1968). Non-linear analysis of concrete by the finite element method. *Journal of American Concrete Institute* (65), 757-766.

Nishikov, G. P., & Atluri, S. N. (1987). Calculation of fracture mechanics parameters for an arbitrary three-dimensional crack by the equivalent domain integral method. *International Journal for Numerical Methods in Engineering , 24*, 1801-1821.

Noel, D. (2007-2008). *Crack Simulation with extended Finite Element Methods.* Internship Report, University of Glasgow, UK, Department of Civil Engineering.

NTSB. (1989). *Aircraft Accident Report - Aloha Airlines, flight243, Boeing 737-200, - N73711 near Maui, Hawaii- 28 April 1988.* National Transportation Safety Board.

NTSB. (1990). *United Airlines Flight 232 McDonnell Douglas DC-10-10 Sioux Gateway Airport, Sioux City, Iowa.* National Transport Safety Bureau.

Nuismer, R. (1975). An energy release rate criterion for mixed mode fracture. *International Journal of Fracture , 11*, 245-250.

Osher, S., & Sethian, J. (1988). Fronts propagating with curvature dependent speed: Algorithms based on Hamilton-Jacobi formulations. *Journal of Computational Physics , 79* (1), 12-49.

Paris, P. C., Gomez, M. P., & Anderson, W. P. (1961). A rational analytic theory of fatigue. *The Trend in Engineering , 13*, 9-14.

Rabczuk, T., & Wall, W. A. (2006-2007). *A course on Extended Finite Element and Meshfree Methods.* Technical University of Munich. Munich, Germany.

Rice, J. R. (1968). A path independent integral and the approximate analysis of strain concentration by notches and cracks. *Journal of Applied Mechanics , 35*, 379-386.

Rots, J. G. (1988). *Computational Modeling of Concrete Fracture.* Ph.D. Dissertation, Delft University, Netherlands.

Rots, J., Nauta, P., Kursters, G., & Blaauwendraad, J. (1985). Smeared crack approach and fracture localization in concrete. *Heron* (30), 1-48.

Saouma, V. E., & Ingraffea, A. R. (1981). Fracture mechanics analysis of discrete cracking. *IABSE Colloq. Adv. Mech.* , 413-436.

Saurin, V. V. (2000). Shape design sensitivity analysis for fracture conditions. *Computers and Structures , 76*, 399-405.

Shih, C. F., & Asaro, R. J. (1988). Elastic-plastic analysis of cracks on bimaterial interfaces : part I-small scale yielding. *Journal of Applied Mechanics , 55*, 299-316.

Shih, C. F., Moran, B., & Nakamura, T. (1986). Energy release rate along a three-dimensional crack front in a thermally stressed body. *International Journal of Fracture , 30*, 79-102.

Sih, G. C. (1973). Energy-density concept in fracture mechanics. *Engineering Fracture Mechanics , 5*, 1037-1040.

Stern, M., Becker, E. B., & Dunham, R. S. (1976). A contour integral computation of mixed-mode stress intensity factors. *International Journal of Fracture , 12* (3), 359-368.

Stolarska, M., Chopp, D. L., Moes, N., & Belytschko, T. (2001). Modeling crack growth by level sets and the extended finite element method. *International Journal for Numerical Methods in Engineering , 51* (8), 943-960.

Sukumar, N., & Prevost, J. H. (2003). Modeling quasi-static crack growth with the extended finite element method. Part I: Computer implementation. *International Journal of Solids and Structures , 40*, 7513-7537.

SwRI. (2005). NASGRO 5.2 User's Guide. San Antonio, TX, USA.

Taroco, E. (2000). Shape sensitivity analysis in linear elastic fracture mechanics. *Computer Methods in Applied Mechanics and Engineering , 188*, 697-712.

Timbrel, C., Chandwani, R., & Cook, G. (2004). State Of The Art In Crack Propagation. *Journee Scientifique* , 1-35.

Vanderplaats, G. (1999). *Numerical Optimization Techniques for Engineering Design* (3 ed.). Colorado Springs, Colorado, USA: Vanderplaats R&D, Inc.

VR&D. (2001). *Vanderplaats Research and Development, Design Optimization Tools User's Manual," Version 5.x.* Vanderplaats Research and Development, Inc., Colorado Spring, CO, USA.

Wells, A. A. (1955). *The condition of fast fracture in aluminum alloys with particular reference to comet failures.* British Welding Research Association Report.

Yau, J. F., Wang, S. S., & Corten, H. T. (1980). A mixed-mode crack analysis of isotropic solids using conservation laws of elasticity. *Journal of Applied Mechanics , 47*, 335-341.

Zahavi, E., & Torbilo, V. (1996). *Fatigue Design: Life expectancy of Machine Parts.* Boca Raton, Florida, USA: CRC Press Inc.

Appendix A

SENSITIVITY OF INTERACTION INTEGRAL

It was mentioned earlier that calculation of sensitivity coefficients of stress intensity factors involves differentiation of the interaction integral with respect to design variables. This section builds upon the material presented in section 2.5.3, and shows a detailed derivation for computation of sensitivity coefficients of interaction integral using semi-analytical method. The interaction energy integral is given by

$$M^{(1,2)} = \int_A \left[\sigma_{ij}^{(1)} \frac{\partial z_i^{(2)}}{\partial x_1} + \sigma_{ij}^{(2)} \frac{\partial z_i^{(1)}}{\partial x_1} - W^{(1,2)} \delta_{1j}\right] \frac{\partial q}{\partial x_j} dA \tag{A.1}$$

Expanding individual terms,

$$\sigma_{ij}^{(1)} \frac{\partial z_i^{(2)}}{\partial x_1} \frac{\partial q}{\partial x_j} = \sigma_{11}^{(1)} \frac{\partial z_1^{(2)}}{\partial x_1} \frac{\partial q}{\partial x_1} + \sigma_{12}^{(1)} \frac{\partial z_1^{(2)}}{\partial x_1} \frac{\partial q}{\partial x_2} + \sigma_{21}^{(1)} \frac{\partial z_2^{(2)}}{\partial x_1} \frac{\partial q}{\partial x_1} + \sigma_{22}^{(1)} \frac{\partial z_2^{(2)}}{\partial x_1} \frac{\partial q}{\partial x_2} \tag{A.2}$$

$$\sigma_{ij}^{(2)} \frac{\partial z_i^{(2)}}{\partial x_1} \frac{\partial q}{\partial x_j} = \sigma_{11}^{(2)} \frac{\partial z_1^{(1)}}{\partial x_1} \frac{\partial q}{\partial x_1} + \sigma_{12}^{(2)} \frac{\partial z_1^{(1)}}{\partial x_1} \frac{\partial q}{\partial x_2} + \sigma_{21}^{(2)} \frac{\partial z_2^{(1)}}{\partial x_1} \frac{\partial q}{\partial x_1} + \sigma_{22}^{(2)} \frac{\partial z_2^{(1)}}{\partial x_1} \frac{\partial q}{\partial x_2} \tag{A.3}$$

$$W^{(1,2)} \delta_{1j} \frac{\partial q}{\partial x_j} = \left[\sigma_{11}^{(2)} \frac{\partial z_1^{(1)}}{\partial x_1} + \sigma_{12}^{(2)} \left(\frac{\partial z_1^{(1)}}{\partial x_2} + \frac{\partial z_2^{(1)}}{\partial x_1}\right) + \sigma_{22}^{(2)} \frac{\partial z_2^{(1)}}{\partial x_2}\right] \frac{\partial q}{\partial x_1} \tag{A.4}$$

Combining Eq. A.1 to Eq. A.4,

$$\begin{aligned} M^{(1,2)} = \int_A & \left[\sigma_{11}^{(1)} \frac{\partial z_1^{(2)}}{\partial x_1} \frac{\partial q}{\partial x_1} + \sigma_{12}^{(1)} \frac{\partial z_1^{(2)}}{\partial x_1} \frac{\partial q}{\partial x_2} + \sigma_{21}^{(1)} \frac{\partial z_2^{(2)}}{\partial x_1} \frac{\partial q}{\partial x_1} + \sigma_{22}^{(1)} \frac{\partial z_2^{(2)}}{\partial x_1} \frac{\partial q}{\partial x_2}\right] dA + \\ & \int_A \left[\sigma_{12}^{(2)} \frac{\partial z_1^{(1)}}{\partial x_1} \frac{\partial q}{\partial x_2} + \sigma_{22}^{(2)} \frac{\partial z_2^{(1)}}{\partial x_1} \frac{\partial q}{\partial x_2} - \sigma_{12}^{(2)} \frac{\partial z_1^{(1)}}{\partial x_2} \frac{\partial q}{\partial x_1} - \sigma_{22}^{(2)} \frac{\partial z_2^{(1)}}{\partial x_2} \frac{\partial q}{\partial x_1}\right] dA \end{aligned} \tag{A.5}$$

Rewriting Eq. A.5 as follows,

$$M^{(1,2)} = \int_A hdA$$
$$\text{where } h = h_1 + h_2 + h_3 + h_4 + h_5 + h_6 - h_7 - h_8 \tag{A.6}$$

and $h_i, i = 1\ to\ 8$ depend upon the stress state.

$$h_1 = E_1 \left[\nu_1 \frac{\partial z_1^{(1)}}{\partial x_1} + \nu_2 \frac{\partial z_2^{(1)}}{\partial x_2}\right] \frac{\partial z_1^{(2)}}{\partial x_1} \frac{\partial q}{\partial x_1} \tag{A.7a}$$

$$h_2 = E_2 \left[\frac{\partial z_1^{(1)}}{\partial x_2} + \frac{\partial z_2^{(1)}}{\partial x_1}\right] \frac{\partial z_1^{(2)}}{\partial x_1} \frac{\partial q}{\partial x_2} \tag{A.7b}$$

$$h_3 = E_2 \left[\frac{\partial z_1^{(1)}}{\partial x_2} + \frac{\partial z_2^{(1)}}{\partial x_1}\right] \frac{\partial z_2^{(2)}}{\partial x_1} \frac{\partial q}{\partial x_1} \tag{A.7c}$$

$$h_4 = E_1 \left[\nu_2 \frac{\partial z_1^{(1)}}{\partial x_1} + \nu_1 \frac{\partial z_2^{(1)}}{\partial x_2}\right] \frac{\partial z_2^{(2)}}{\partial x_1} \frac{\partial q}{\partial x_2} \tag{A.7d}$$

$$h_5 = \sigma_{12}^{(2)} \frac{\partial z_1^{(1)}}{\partial x_1} \frac{\partial q}{\partial x_2} \tag{A.7e}$$

$$h_6 = \sigma_{22}^{(2)} \frac{\partial z_2^{(1)}}{\partial x_1} \frac{\partial q}{\partial x_2} \tag{A.7f}$$

$$h_7 = \sigma_{12}^{(2)} \frac{\partial z_1^{(1)}}{\partial x_2} \frac{\partial q}{\partial x_1} \tag{A.7g}$$

$$h_8 = \sigma_{22}^{(2)} \frac{\partial z_2^{(1)}}{\partial x_2} \frac{\partial q}{\partial x_1} \tag{A.7h}$$

Factors E_1, E_2, ν_1, and ν_2 depend on stress state and are given as follows:

Plane Strain	Plane Stress	
$E_1 = \frac{E}{(1+\nu)(1-2\nu)}$	$E_1 = \frac{E}{1-\nu^2}$	(A.8a)
$E_2 = \frac{E}{2(1+\nu)}$	$E_2 = \frac{E}{2(1+\nu)}$	(A.8b)
$\nu_1 = (1-\nu)$	$\nu_1 = 1$	(A.8c)
$\nu_2 = \nu$	$\nu_2 = \nu$	(A.8d)

Differentiating h_i with respect to design variable yields (for plane strain state):

$$\frac{\partial h_1}{\partial b} = E_1 \left\{ \left[\nu_1 \frac{\partial^2 z_1^{(1)}}{\partial b \partial x_1} + \nu_2 \frac{\partial^2 z_2^{(1)}}{\partial b \partial x_2} \right] \frac{\partial z_1^{(2)}}{\partial x_1} \frac{\partial q}{\partial x_1} + \left[\nu_1 \frac{\partial z_1^{(1)}}{\partial x_1} + \nu_2 \frac{\partial z_2^{(1)}}{\partial x_2} \right] \frac{\partial^2 z_1^{(2)}}{\partial b \partial x_1} \frac{\partial q}{\partial x_1} + \left[\nu_1 \frac{\partial z_1^{(1)}}{\partial x_1} + \nu_2 \frac{\partial z_2^{(1)}}{\partial x_2} \right] \frac{\partial z_1^{(2)}}{\partial x_1} \frac{\partial^2 q}{\partial b \partial x_1} \right\} \tag{A.9a}$$

$$\frac{\partial h_2}{\partial b} = E_2 \left\{ \left[\frac{\partial^2 z_1^{(1)}}{\partial b \partial x_2} + \frac{\partial^2 z_2^{(1)}}{\partial b \partial x_1} \right] \frac{\partial z_1^{(2)}}{\partial x_1} \frac{\partial q}{\partial x_2} + \left[\frac{\partial z_1^{(1)}}{\partial x_2} + \frac{\partial z_2^{(1)}}{\partial x_1} \right] \frac{\partial^2 z_1^{(2)}}{\partial b \partial x_1} \frac{\partial q}{\partial x_2} + \left[\frac{\partial z_1^{(1)}}{\partial x_2} + \frac{\partial z_2^{(1)}}{\partial x_1} \right] \frac{\partial z_1^{(2)}}{\partial x_1} \frac{\partial^2 q}{\partial b \partial x_2} \right\} \tag{A.9b}$$

$$\frac{\partial h_3}{\partial b} = E_2 \left\{ \left[\frac{\partial^2 z_1^{(1)}}{\partial b \partial x_2} + \frac{\partial^2 z_2^{(1)}}{\partial b \partial x_1} \right] \frac{\partial z_2^{(2)}}{\partial x_1} \frac{\partial q}{\partial x_1} + \left[\frac{\partial z_1^{(1)}}{\partial x_2} + \frac{\partial z_2^{(1)}}{\partial x_1} \right] \frac{\partial^2 z_2^{(2)}}{\partial b \partial x_1} \frac{\partial q}{\partial x_1} + \left[\frac{\partial z_1^{(1)}}{\partial x_2} + \frac{\partial z_2^{(1)}}{\partial x_1} \right] \frac{\partial z_2^{(2)}}{\partial x_1} \frac{\partial^2 q}{\partial b \partial x_1} \right\} \tag{A.9c}$$

$$\frac{\partial h_4}{\partial b} = E_1 \left\{ \left[\nu_2 \frac{\partial^2 z_1^{(1)}}{\partial b \partial x_1} + \nu_1 \frac{\partial^2 z_2^{(1)}}{\partial b \partial x_2} \right] \frac{\partial z_2^{(2)}}{\partial x_1} \frac{\partial q}{\partial x_2} + \left[\nu_2 \frac{\partial z_1^{(1)}}{\partial x_1} + \nu_1 \frac{\partial z_2^{(1)}}{\partial x_2} \right] \frac{\partial^2 z_2^{(2)}}{\partial b \partial x_1} \frac{\partial q}{\partial x_2} + \left[\nu_2 \frac{\partial z_1^{(1)}}{\partial x_1} + \nu_1 \frac{\partial z_2^{(1)}}{\partial x_2} \right] \frac{\partial z_2^{(2)}}{\partial x_1} \frac{\partial^2 q}{\partial b \partial x_2} \right\} \tag{A.9d}$$

$$\frac{\partial h_5}{\partial b} = \left\{ \frac{\partial \sigma_{12}^{(2)}}{\partial b} \frac{\partial z_1^{(1)}}{\partial x_1} \frac{\partial q}{\partial x_2} + \sigma_{12}^{(2)} \frac{\partial^2 z_1^{(1)}}{\partial b \partial x_1} \frac{\partial q}{\partial x_2} + \sigma_{12}^{(2)} \frac{\partial z_1^{(1)}}{\partial x_1} \frac{\partial^2 q}{\partial b \partial x_2} \right\} \tag{A.9e}$$

$$\frac{\partial h_6}{\partial b} = \left\{ \frac{\partial \sigma_{22}^{(2)}}{\partial b} \frac{\partial z_2^{(1)}}{\partial x_1} \frac{\partial q}{\partial x_2} + \sigma_{22}^{(2)} \frac{\partial^2 z_2^{(1)}}{\partial b \partial x_1} \frac{\partial q}{\partial x_2} + \sigma_{22}^{(2)} \frac{\partial z_2^{(1)}}{\partial x_1} \frac{\partial^2 q}{\partial b \partial x_2} \right\} \tag{A.9f}$$

$$\frac{\partial h_7}{\partial b} = \left\{ \frac{\partial \sigma_{12}^{(2)}}{\partial b} \frac{\partial z_1^{(1)}}{\partial x_2} \frac{\partial q}{\partial x_1} + \sigma_{12}^{(2)} \frac{\partial^2 z_1^{(1)}}{\partial b \partial x_2} \frac{\partial q}{\partial x_1} + \sigma_{12}^{(2)} \frac{\partial z_1^{(1)}}{\partial x_2} \frac{\partial^2 q}{\partial b \partial x_1} \right\} \tag{A.9g}$$

$$\frac{\partial h_8}{\partial b} = \left\{ \frac{\partial \sigma_{22}^{(2)}}{\partial b} \frac{\partial z_2^{(1)}}{\partial x_2} \frac{\partial q}{\partial x_1} + \sigma_{22}^{(2)} \frac{\partial^2 z_2^{(1)}}{\partial b \partial x_2} \frac{\partial q}{\partial x_1} + \sigma_{22}^{(2)} \frac{\partial z_2^{(1)}}{\partial x_2} \frac{\partial^2 q}{\partial b \partial x_1} \right\} \tag{A.9h}$$